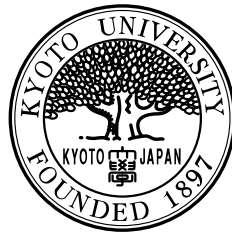


Evidence for in-medium modification of the ϕ meson at normal nuclear density

Ryotaro Muto



A dissertation submitted in partial fulfillment
of the requirements for the degree of
Doctor of Science

DEPARTMENT OF PHYSICS
FACULTY OF SCIENCE
KYOTO UNIVERSITY

January, 2007

Abstract

Invariant mass spectra of $\phi \rightarrow e^+e^-$ decays have been measured in 12-GeV $p + A$ reactions at the KEK Proton-Synchrotron to detect possible in-medium modification of the spectral function of the ϕ meson. Copper and carbon targets are used to provide nuclei with different nuclear sizes. A significant excess on the low-mass side of the ϕ meson peak is observed in the low $\beta\gamma$ region of the ϕ mesons ($\beta\gamma_\phi < 1.25$) with the copper target. In the high $\beta\gamma$ region ($\beta\gamma_\phi > 1.25$) with the copper target and in all the $\beta\gamma$ region with the carbon target, however, the spectral shapes of ϕ mesons are well described by the Breit-Wigner shape with known effects from detectors and physics processes. This observation is consistent with a picture of the mass modification in a nucleus, because the modification is expected to be more detectable for ϕ mesons produced in a larger nucleus with a lower velocity, due to an increase of their decay probability inside the nucleus. We have performed model calculations including in-medium mass modification of the ϕ meson to reproduce the observed spectra. We assume the linear dependences of the decrease of the pole mass and the broadening of the total decay width (Γ_ϕ^{tot}) of the ϕ meson on the nuclear density. For the partial width of $\phi \rightarrow e^+e^-$ decay (Γ_ϕ^{ee}), we assume following two cases: (i) the branching ratio $\Gamma_\phi^{ee} / \Gamma_\phi^{\text{tot}}$ remains unchanged in the medium, and (ii) Γ_ϕ^{ee} doesn't change in the medium. The data favor the case (i) with the pole-mass decrease of 3.4% and the width broadening by a factor of 3.6 for the ϕ meson at normal nuclear density. This result is the first experimental data which show the modification of the ϕ meson mass spectra in nuclear matter.

Contents

1	Introduction	4
2	Experimental Procedure	9
2.1	Overview of the apparatus	9
2.2	Accelerator facility and beam line	10
2.3	Targets and beam profile	13
2.4	The spectrometer magnet	16
2.5	Tracking	23
2.5.1	Cylindrical drift chamber (CDC)	23
2.5.2	Barrel-shaped drift chambers (BDC)	31
2.6	Start timing counter	32
2.7	Electron identification counters	36
2.7.1	Front gas-čerenkov counter	36
2.7.2	Rear gas-čerenkov counter	37
2.7.3	Rear lead-glass EM calorimeter	40
2.7.4	Side lead-glass EM calorimeter	42
2.7.5	Forward lead-glass EM calorimeter	45
2.8	Trigger	46
2.8.1	Electron first level trigger	47
2.9	Data acquisition system	47
3	Analysis	51
3.1	Electron trigger data set	51
3.2	Calibration	51
3.2.1	Drift time measurement and determination of drift length	51
3.2.2	Global position alignment of tracking devices	53
3.2.3	Gain calibration of lead glass calorimeter	57
3.3	Event reconstruction	57
3.3.1	Track reconstruction	57
3.3.2	Mass scale and resolution	60
3.3.3	Vertex reconstruction	65
3.3.4	Electron identification	67
3.3.5	Contamination by electron misidentification	76

4	Results and Discussions	78
4.1	Observed mass spectra of e^+e^- pairs	78
4.2	Expected mass shape for in-vacuum decay of ϕ mesons	78
4.2.1	Resonance shape of $\phi \rightarrow e^+e^-$ decay	78
4.2.2	Physics processes which distort mass shape	80
4.2.3	Effect of the coulomb potential of target nuclei	84
4.2.4	Monte Carlo simulation of the detector response	86
4.3	The fit of the mass spectra with the expected resonance shape	87
4.4	Evaluation of the number of the excess	93
4.4.1	Systematic errors	93
4.5	Theoretical interpretation	96
4.5.1	Model calculation with mass modification	96
4.5.2	Best fit parameters for pole shift and width broadening of ϕ meson	100
4.6	Comparison with ρ and ω mesons	104
5	Conclusion	109
6	Acknowledgements	111

Chapter 1

Introduction

The properties of hadrons, which are composite particles of quarks and gluons, have been measured and determined in many experimental studies in the past. These properties, such as mass and decay width, are the vacuum expectation values. Therefore, in principle, these properties can be different when the vacuum itself changes, i.e., when hadrons are in hot or dense matter. It is difficult, however, to calculate the properties within a framework of quantum chromodynamics (QCD), since the coupling constant in the strong force sharply rises at low energy. In 1960's, Nambu and Jona-Lasinio proposed the spontaneous breaking of the chiral symmetry as the fundamental mechanism to create the mass of hadrons [1]. Quarks gain their current mass (a few MeV/c^2 for u and d quarks, $\simeq 100 \text{ MeV}/c^2$ for s quark) through the Higgs mechanism. Further they gain their effective mass due to the chiral symmetry breaking in the quantum chromodynamics. It is noteworthy that 99% of nucleon mass is to be generated in the latter mechanism. Figure 1.1 shows the schematic behavior of the $\langle \bar{q}q \rangle$, quark-antiquark pair condensate, calculated with the Nambu and Jona-Lasinio (NJL) model [2]. The $\langle \bar{q}q \rangle$ is the order parameter of the chiral symmetry. According to the theoretical calculation, the $\langle \bar{q}q \rangle$ decreases linearly to the density and the chiral symmetry will be restored partially even at normal nuclear density, whereas the $\langle \bar{q}q \rangle$ shows the sudden drop around the critical temperature, $T \sim 150\text{--}200 \text{ MeV}$.

Although this theoretical concept is very attractive and is widely accepted, its experimental evidence has not been established so far. A possible and interesting approach is to measure the properties of hadrons in hot/dense nuclear matter in which the chiral symmetry could be restored and the properties of hadrons are expected to change.

The possibility of the decrease in the mass of light vector mesons in nuclear medium was first pointed out by Brown and Rho [6]. Thereafter, many theoretical studies were conducted. Hatsuda and Lee calculated the density dependence of the ϕ meson mass based on the QCD sum rule [7, 8] as shown in Fig. 1.2. According to their calculation, $m_\phi(\rho)/m_\phi(0)$ can be approximated as $m_\phi(\rho)/m_\phi(0) = 1 - k \cdot y \cdot (\rho/\rho_0)$, where $m_\phi(\rho)$ is the mean value of the mass spectrum of ϕ meson at density ρ , y denoting $\frac{2\langle \bar{s}s \rangle_N}{\langle \bar{u}u \rangle_N + \langle \bar{d}d \rangle_N}$ is a strangeness content in the nucleon, and ρ_0 is normal nuclear density, 0.17 fm^{-3} .

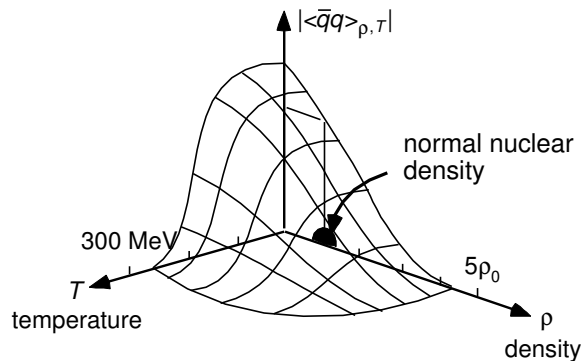


Figure 1.1: A quark condensate $|\langle\bar{q}q\rangle|$ as a function of temperature T and density ρ taken from Ref. [3]

In their prediction the actual value of the proportional coefficient k is 0.15 ± 0.05 , the error of which is caused from the uncertainty in the π -N Σ term. Also y itself has uncertainty from 0.12 to 0.22. Thus the product of k and y is in the range of 0.01 to 0.04, corresponding to the mass decrease for the ϕ meson at normal nuclear density to be 10–40 MeV/ c^2 .¹ As for the decay width of ϕ meson, several theoretical calculations exist and they predict the broadening of the width by factor five or six [9, 10] to ten [11], at normal nuclear density. Klingl, Waas and Weise calculated the in-medium spectra of ϕ meson, as shown in Figure 1.3. They predicted that the width of ϕ meson increases by a factor of ten with a small pole mass shift. When the width of ϕ meson broadens by such a large factor, the lifetime of ϕ meson $c\tau_\phi$ in a nucleus is reduced from 46 to 5 fm, and the probability of in-medium decay increases.

There exist several experimental reports observing a signature of the in-medium modification of ρ and ω mesons, including our reports [12, 14, 15, 4, 5]. The CERES/NA45 experiment, which was carried out at CERN-SPS to investigate the nuclear matter at high temperature, measured low-mass dielectron spectra in Pb-Au collisions at 158 A GeV [12]. They observed the enhancement of e^+e^- pair yield in the mass range of 0.3 – 0.7 GeV/ c^2 over the expected yield from the known hadronic sources in p-p collisions. Recently the NA60 collaboration also reported in-medium modification of the ρ meson at high temperature in 158 A GeV In-In collisions by measuring the dimuon spectra using high-granularity silicon pixel telescopes [15]. They observed a broadening of ρ meson in dimuon spectra but without a significant mass shift. The theoretical interpretation for above heavy-ion collision experiments is rather difficult since the estimation for the time evolution of the temperature and density of the system is inevitable. As the studies concerning the dense matter, only the CBELSA/TAPS collaboration reported $14^{+1}_{-8}\%$ of mass decrease of the ω meson at normal nuclear density in the invariant mass distribution of the $\pi^0\gamma$ decay channel. The result is consistent with the theoretical

¹It should be noted that the mass in their prediction is not a pole mass but a mean value of the mass spectrum of the ϕ meson. The two is almost same for narrow resonances such as ϕ and ω .

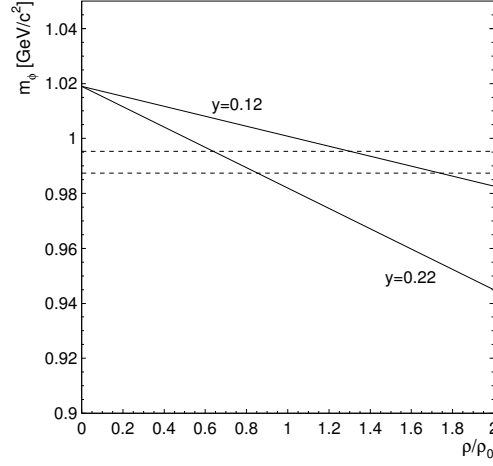


Figure 1.2: The mean value of the mass spectrum of ϕ meson as functions of density which is normalized by normal nuclear density ρ_0 , predicted with use of the QCD sum rule [7]. Two solid lines correspond to the two typical values of y , the strangeness content in the nucleon. The dashed lines indicate the $K^0\bar{K}^0$ and K^+K^- decay thresholds at $\rho = 0$, which are the main decay modes of the ϕ meson.

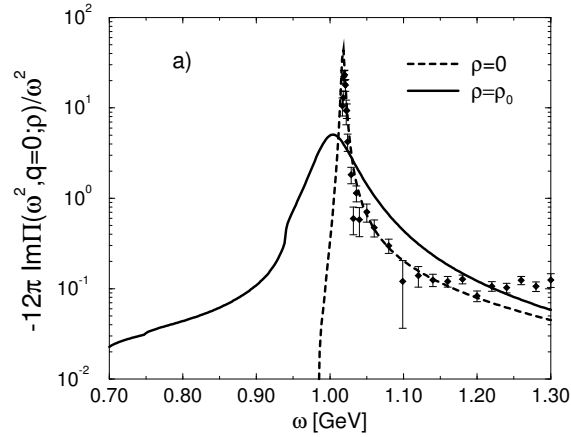


Figure 1.3: Calculation for spectrum of the strange quark current-current correlation function corresponding to the spectral shape of ϕ meson [11]. Dashed curve is for the shape in vacuum, and solid curve is for the shape at normal nuclear density, ρ_0 .

prediction [7], although their result have a large error. The disadvantage of this experiment is that the data are not free from the effect caused by π^0 rescattering. Further informations from experiments are necessary to definitely conclude the vector meson modification in nuclear medium.

It is worth mentioning the GSI S236 experiment, which is not the study for the vector meson modification, but strongly related to the chiral symmetry restoration in the dense matter. They reported an enhancement of the pion-nucleus potential in deeply-bound pionic nuclei as a possible signature of the chiral symmetry restoration [16]. They argued that the pion decay constant $(f_\pi)^2$, which is also the order parameter of chiral symmetry breaking, decreases 36% at normal nuclear density. This result is consistent with the theoretical prediction proposed by Brown and Rho [6].

On the ϕ meson modification, however, the experimental information is more limited. The mass resolution of CERES/NA45 experiment was not enough to discuss the mass modification of the ϕ meson. NA60 collaboration observed a clear peak of ϕ meson with the mass resolution of about 30 MeV/ c^2 in their dimuon spectra, but they claim no modification of the ϕ meson. It is not surprising because the ϕ mesons detected in their spectrometer had large velocity, $\beta\gamma = 10\text{--}30$, thus the fraction of the in-medium decays of ϕ mesons could be small. The HADES experiment is now running and they reported dielectron spectra in 2 GeV·A C+C collisions [17]. In this energy domain, central heavy ion collisions are expected to form a reaction volume with temperatures of about $T=60\text{--}90$ MeV and densities up to $3\rho_0$. Thus far, their statistics is not sufficient to discuss the mass modification of vector mesons. The PHENIX experiment at RHIC reported the $\phi \rightarrow e^+e^-$ spectrum in Au+Au collisions at $\sqrt{s_{NN}} = 200$ GeV [18]. They observed the ϕ meson signal in the e^+e^- invariant mass distribution from the data taken in 2002, but with a marginal signal strength; too poor to see the modification of the ϕ meson shape. In 2004, they acquired about 40 times larger statistics, thus a significant improvement in the electron pair analysis is expected in near future. The LEPS collaboration reported a possible increase of the ϕ -N interaction in medium by measuring the A -dependence of the ϕ photo-production yields in the K^+K^- decay mode [19], although the modification of the mass spectrum of the ϕ meson was not observed. At the moment, no clear evidence for the modification of the ϕ meson mass has been observed in the above experiments.

The present experiment, KEK-PS E325, was conducted at the KEK 12-GeV Proton-Synchrotron, in order to detect a signature of the in-medium mass modifications of vector mesons in the reactions of 12 GeV $p + A \rightarrow \rho, \omega, \phi + X$. In our earlier publications [4, 5], we reported the mass modification of ρ and ω mesons in nuclear medium. In the present thesis, we focus on the results of the $\phi \rightarrow e^+e^-$ decay channel. The result described in this thesis is the first positive signal of the ϕ meson modification revealed in the e^+e^- mass spectrum [20].

In the case of $\rho/\omega \rightarrow e^+e^-$ decays, it is very difficult to distinguish matter effects on either one of the two mesons, due to the overlapping of two peaks with different widths [4, 5]. The natural width of the ϕ meson is narrow (4.26 MeV/ c^2) without other resonances in the vicinity; therefore, we can examine the possible mass modification

more clearly. When the properties are modified by the medium, the observed spectrum contains two components: in-vacuum decays with a normal mass distribution and in-medium decays with a modified mass distribution. The latter component can cause an excess around the ϕ meson peak in invariant mass spectra. For a lower velocity and larger target nuclei, the amount of such an excess is expected to increase due to the increase of the decay probability inside the nucleus. When we select ϕ mesons with $\beta\gamma_\phi < 1.25$ for a copper target, we expect 6% of them to decay inside a nucleus, even without any in-medium broadening.

The E325 spectrometer comprises two arms with electron ID counters and kaon ID counters that share a dipole magnet and tracking devices. The typical acceptance for the ϕ meson in the laboratory frame was $0.5 < y_\phi < 2.0$ and $0 < p_{T\phi} < 1$ covering the $\beta\gamma$ region from 0.5 to 3.5. The data taking was carried out from 1997 to 2002. In this thesis, we report analysis results with e^+e^- -triggered data collected in 2001 and 2002. A primary proton beam with a typical intensity of 1×10^9 protons per spill was delivered to targets. In order to observe the nucleus-size dependence, we accumulated data by using two types of targets, carbon (C) and copper (Cu). The combination of such a high-intensity beam with targets of as thin as 0.5% radiation length enabled us to measure the e^+e^- decay mode with enough statistics and to suppress the background from γ conversions in the target materials.

In Chapter 2, the experimental procedure is described. The details of the analysis procedure are presented in Chapter 3. In Chapter 4 we present the data of the e^+e^- -invariant mass spectra, and discuss on the nuclear size dependence and the velocity dependence of the observed e^+e^- -spectra in the ϕ meson mass region. The conclusion is given in Chapter 5.

Chapter 2

Experimental Procedure

2.1 Overview of the apparatus

The spectrometer was built at the primary beam-line EP1-B in the 12 GeV Proton Synchrotron (PS) in KEK. The beam line EP1-B was constructed in 1995 for experiments requiring a high-intensity primary beam [21]. This beam line was designed to transport 12 GeV protons with the maximum intensity of 4×10^9 per 2 seconds spill, with a small beam halo.

In the present experiment, the primary protons with a typical intensity of 6 to 9×10^8 protons per spill were delivered to nuclear targets located at the center of the spectrometer magnet to produce the vector mesons inside a nucleus. We employed two kinds of targets, carbon and copper, to investigate the nuclear size dependence in the invariant mass spectra of the vector mesons. We used very thin targets of about 0.5 % radiation length in each. The detail of the target configuration is described in Sec. 2.3. The combination of thin targets with a high intensity beam enabled us to reduce backgrounds by keeping the γ conversion rate in the target material comparable to the π^0 Dalitz decay rate which is 1.2%.

The spectrometer was designed to measure the $\rho/\omega/\phi \rightarrow e^+e^-$ decays and $\phi \rightarrow K^+K^-$ decay with the same apparatus. The schematic view of our spectrometer is shown in Fig. 2.1 and Fig. 2.2¹. The spectrometer had two electron arms and two kaon arms, which shared the dipole magnet and the tracking devices. The electron arm covered from $\pm 12^\circ$ to $\pm 90^\circ$ horizontally and $\pm 22^\circ$ vertically. The kaon arms covered from $\pm 12^\circ$ to $\pm 54^\circ$ horizontally and $\pm 6^\circ$ vertically. The typical acceptance for the ϕ mesons in the e^+e^- decay channel was $0 < p_{T\phi} < 1$ GeV/ c and $0.5 < y_\phi < 2.0$ while the beam rapidity y_{beam} is 3.3. This coverage corresponds to $0.5 < \beta\gamma_\phi < 3.5$ for ϕ mesons. The acceptance was optimized for slowly moving vector mesons which have a larger decay probability inside a nucleus in which they are produced. A detailed description of the E325 spectrometer can be found in [22].

¹In this thesis, we adopt the right-handed coordinate system of which the origin is at the center of the spectrometer magnet, the x-axis is parallel to the beam direction, and the z-axis is vertical pointing upward.

Tracking was performed with two kinds of drift chambers, a cylindrical drift chamber (CDC) and barrel-shaped drift chambers (BDCs). In the year 2000, the vertex drift chamber (VTC) was installed at the center of the CDC to improve the vertex reconstruction resolution. We did not use the VTC information in the present analysis because the mass acceptance are significantly different between the targets when VTC hits were required.

The vertical magnetic field was provided by the dipole magnet, with the field strength of 0.71 T at the center of the magnet and the field integral of 0.81 T·m from the center to 1680 mm in radius where the BDCs were located.

To identify the electron and positron from the decay of the vector mesons, the electron arms had two or three stages of the electron identification counters. The first stage was done by Front Gas Čerenkov counters (FGC) which covered from $\pm 12^\circ$ to $\pm 90^\circ$ horizontally and $\pm 23^\circ$ vertically. The second stage consisted of three types of electron-identification counters. The rear gas-Čerenkov counters (RGC) covered $\pm 12^\circ$ to $\pm 54^\circ$ horizontally and $\pm 6^\circ$ vertically. These regions correspond to the kaon-arm acceptance. The rear lead-glass calorimeters (RLG) covered the same horizontal acceptances as RGCs, and vertical acceptances were outside the kaon-arm acceptance, from $\pm 9^\circ$ to $\pm 23^\circ$. The horizontal regions from $\pm 57^\circ$ to $\pm 90^\circ$ were covered by the side lead-glass calorimeters (SLG), which had vertical acceptance of $\pm 23^\circ$. In the kaon-arm acceptance, the forward lead-glass calorimeters (FLG) were placed as the third stage of the electron identification. The FLGs covered $\pm 7^\circ$ vertically and 12° to 54° in the left arm, -12° to -40° in the right arm, horizontally.

Kaon identification was done by the time of flight measurement with the three types of scintillator arrays, cooperating with the pion veto by segmented aerogel Čerenkov counters (AC). The AC was a threshold-type Čerenkov detector with aerogel as a radiator whose refractive index was 1.034, to separate kaons from pions in the momentum region of 0.53 to 1.88 GeV/ c [23, 24]. The time of flight measurement was done by the start timing counters (STC) placed around the inner ridge of CDC at 380 mm from the targets and the forward time of flight counters (FTOF) placed at 3951 mm from the targets. Hodoscope counters (HD) were also used to provide the information of the charge, the crude momentum of the tracks, and $\beta(=v/c)$ for the kaon trigger. STCs were also used to provide the event time-zero since we could not count beam protons one by one due to the high intensity.

In the following sections details of the experimental components which are relevant for the present analyses are described.

2.2 Accelerator facility and beam line

The proton synchrotron facility at KEK consists of four stages of accelerators, the 750 kV Cockroft-Walton, the 40 MeV LINAC, the 500 MeV Booster Synchrotron and the 12 GeV Proton Synchrotron (PS).

The typical beam intensity was 3×10^{12} protons per spill in PS. During our exper-

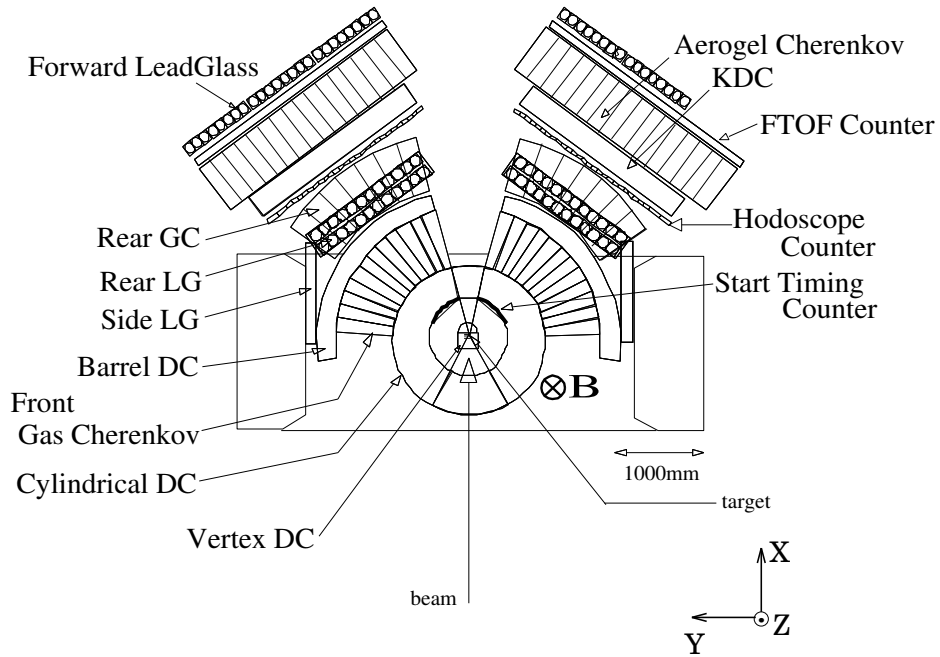


Figure 2.1: Schematic view of the E325 spectrometer, the top view.

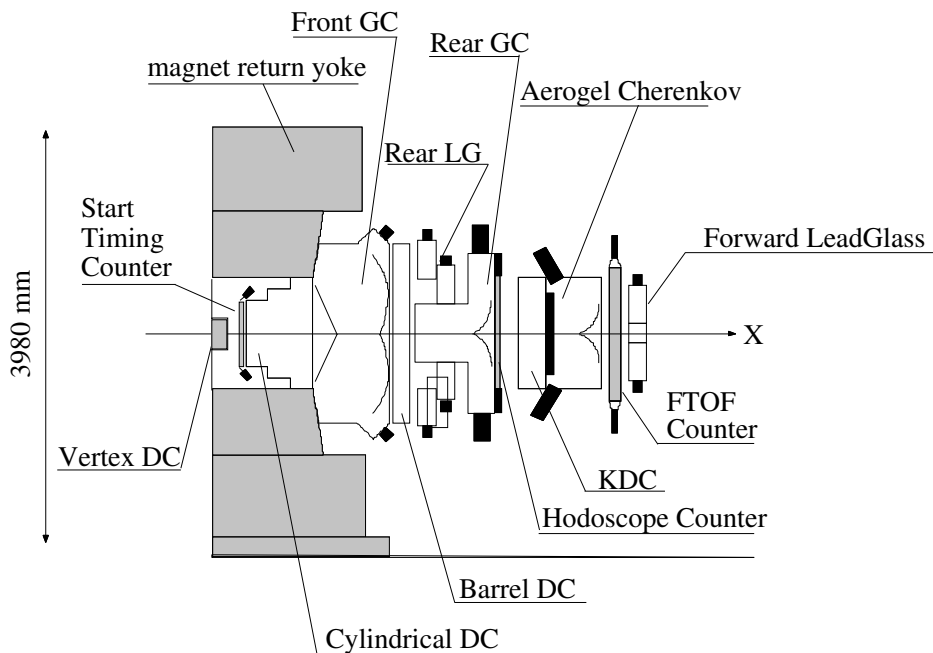


Figure 2.2: Schematic view of the E325 spectrometer, the cross section along the center of the kaon arm, 33° from the beam line, is shown.

iment these protons were delivered to two primary beam lines simultaneously, about 1% to the EP1 beam line and 99% to EP2. The beam in EP1 can be switched either to EP1-A or to EP1-B. The beam line EP1-A is used to produce secondary particles for experiments using low energy pions or kaons in the slow extraction mode and for the neutrino oscillation experiment (K2K) in the fast extraction mode. The present experiment is performed at EP1-B which is a special beam line for primary proton usage. The schematic view of the beam line EP1-B is shown in Fig. 2.3.

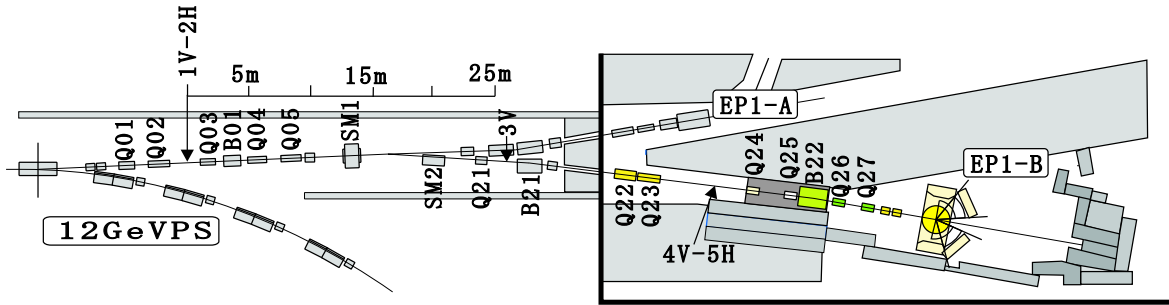


Figure 2.3: Schematic view of the EP1-B beam line.

When EP1-B is in operation, protons extracted to the EP1 beam line were focused with a set of quadrupole magnets, **Q01** and **Q02** to the first vertical collimator **1V** where the intensity was typically reduced to one-fifteenth. Here the initial image of the beam was defined by **1V** together with the horizontal collimator **2H**. At this point the beam profile from PS spreads vertically so that the beam intensity was controlled by changing the aperture of the collimator **1V**. Typical aperture of the collimators **1V** and **2H** were set as 8.0 mm and 2.2 mm respectively. Then the beam was bent by six degrees with the steering magnets **SM1** and **SM2**, and was vertically focused with a set of quadrupole magnets (**Q03**, **Q04**, **Q05**, **Q21**) to the point where the vertical collimator **3V** was placed. The vertical collimator **3V** was used to remove beam halo. Then the beam was transferred by the 'DQQ' (**B21**, **Q22**, **Q23**) complex to the first focusing point where the collimators **4V** and **5H** were located and again the rejection of beam halo was performed. After passing through the other beam-focusing complex 'QQDQQ' (**Q24**, **Q25**, **B22**, **Q26**, **Q27**), the beam was delivered to the final focusing point at the center of the spectrometer. At the target we obtained the size of the beam spot of 1~2 mm in FWHM. At the end of the EP1-B beam line, the intensity of beam protons was monitored with 10% accuracy using an ionization chamber [25]. The repetition period was four seconds, and the flat top of the spill was about 1.8 seconds.

In prior to the experimental data accumulation, the aperture of the collimators were tuned to reduce the beam halo. It was turned out that the adjustment of the collimators was effective to reduce the random trigger rate, so that the adjustment was done to minimize the interaction trigger rate of the spectrometer with keeping the transmission of beam particles constant. The scanning of the magnetic field strengths of **B21** and **B22** was also effective to reduce the beam halo, by controlling the beam trajectory

and minimize the interference of the beam halo with the beam pipe. We chose the setting where the least trigger rate was realized. These tunings were performed in every accelerator tuning cycle of about two weeks long, because the extraction status of a beam from the PS was different in every cycle, but quite stable within a cycle. The collimator settings in the present data-taking period are listed in Table 2.1. The collimator **4V** in the year 2001 and **3V** and **4V** in the year 2002 were full opened, because these were not effective to reduce the halo.

year	1V	2H	3V	4V	5H
2001	8.0mm	4.0mm	50mm	<i>full</i>	15.0mm
2002		2.7mm	<i>full</i>	<i>full</i>	

Table 2.1: The collimator width setting.

2.3 Targets and beam profile

We used two kinds of targets, carbon and copper, aligned in line along the beam axis. We used two copper targets and one carbon target in the year 2001, four copper targets and one carbon target in the 2002. The configuration of the targets used in the present experiment is summarized in Table 2.2. The size of each targets were determined not to disturb the acceptance of any other target. The target holder was mounted in VTC located at the center of the magnet. The schematic view of the target holder is shown in Fig. 2.5. The targets were held at the bottom sandwiched by the two polyethylene stays with thicknesses of 1 mm.

material	mass number	x position [mm]	width [mm]	height [mm]	thickness [mg/cm ²]	interaction length [%]	radiation length [%]
2001							
carbon	12.011	0	25	25	92	0.11	0.21
copper	63.546	± 48	25	25	2×73	2×0.054	2×0.57
2002							
carbon	12.011	0	10	25	184	0.21	0.43
copper	63.546	$-43, -23, +24, +48$	10	25	4×73	4×0.054	4×0.57

Table 2.2: The target dimensions, interaction lengths and radiation lengths in year 2001 and 2002. We used one carbon target and two (four) copper targets in 2001 (2002).

To reduce the interaction of beam protons with air, the entire beam line was kept as vacuum from the extraction point after **1V-2H** collimators to a front of VTC. The region of vacuum was terminated with a 200- μ m-thick Mylar sheet at the front of VTC.

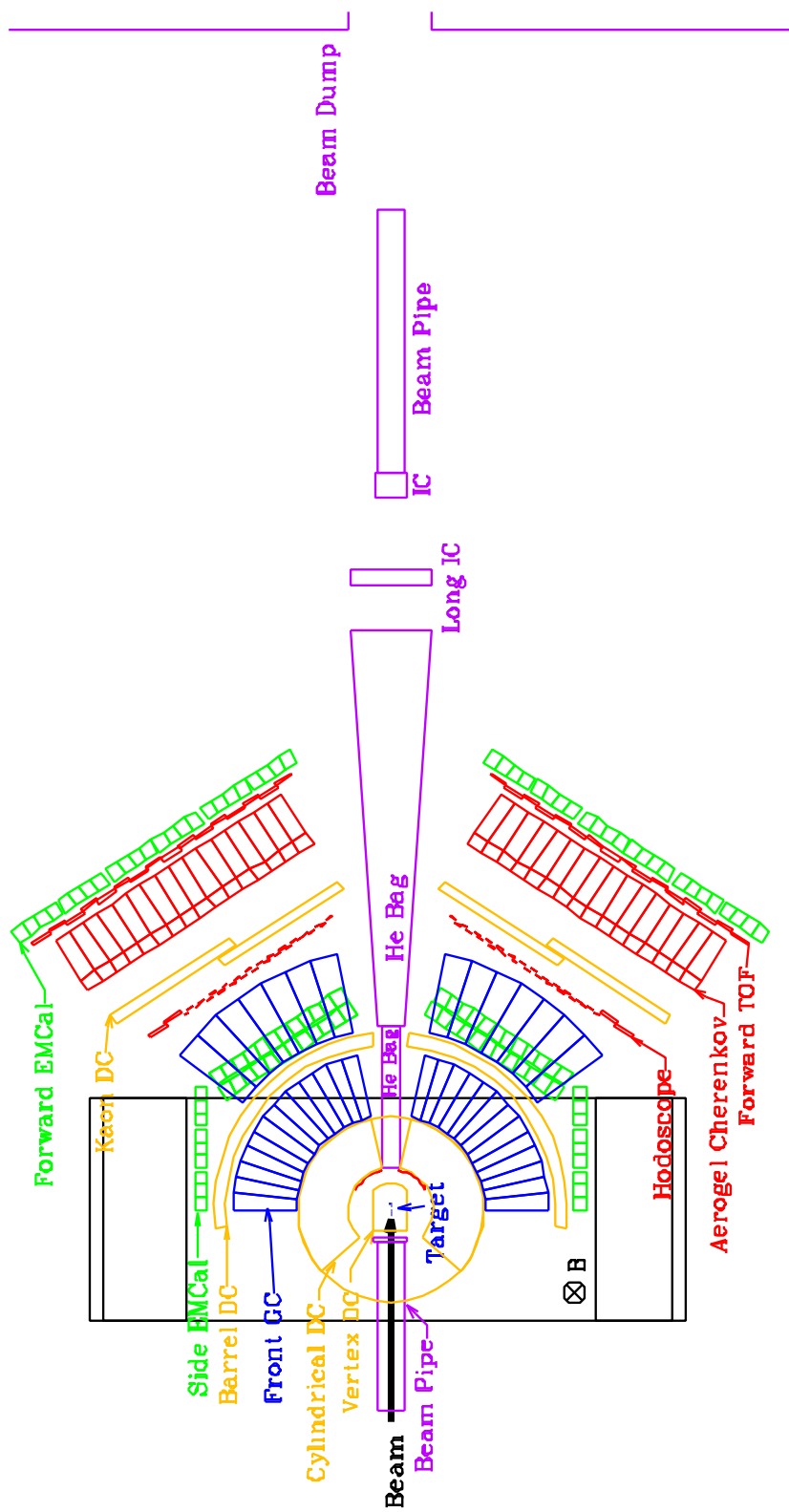


Figure 2.4: Schematic view of target and beam pipe.

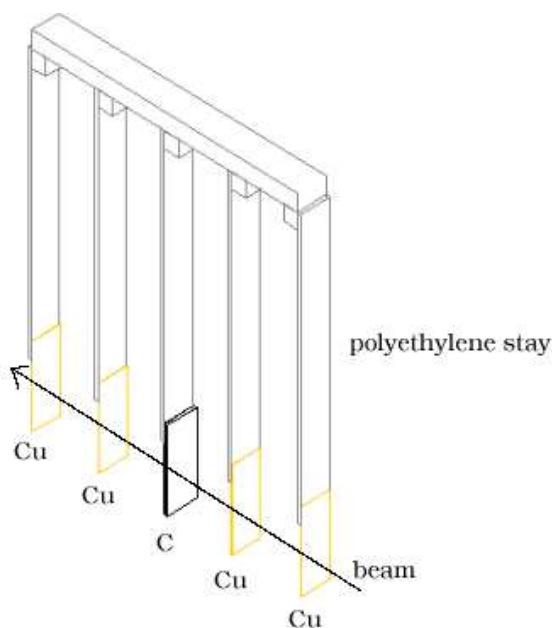


Figure 2.5: Schematic view of targets and their supports in the year 2002.

Behind the exit of VTC, the beam line was followed by a helium-filled beam pipe, as shown as “He Bag” in Figure 2.4. A helium gas was flowed at a rate of 1000 cc per minute. The ion chamber was located at the end of the He Bag to measure the beam intensity. Between the ion chamber and the beam dump, a vacuum beam pipe was located.

Beam Profile

Figure 2.6 shows the beam profile at the target position which was measured as follows. The center target, carbon, whose thickness was 1 mm in the year 2002, worked as the 1mm-wide probe when the target holder was rotated by 90° around the z axis. The horizontal beam position can be moved with the bending magnet **B22**, located most downstream the EP1-B beamline (see Figure 2.3). The beam profile in the horizontal direction can be measured by counting the interaction rate by changing the beam position. The rates as a function of the beam position are plotted in Figure 2.6. Here, the relation (2.1) is used to obtain the horizontal beam position at the center of the pole piece from the voltage (V) of the **B22** power supply;

$$(2.1) \quad y = 0.109 \times (V - V_0)$$

The offset was optimally obtained with the measured beam profile. The one standard deviation of the beam spot sizes in the horizontal direction were estimated to be 1.59 mm for 2001 and 0.83 mm for 2002 by subtracting the effective thickness of the carbon target.

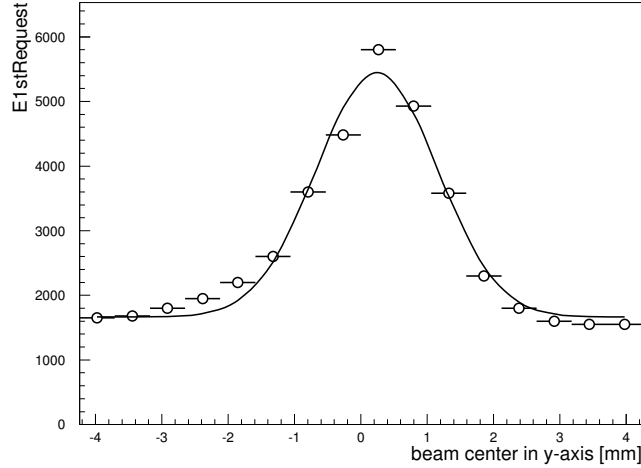


Figure 2.6: Interaction rate as a function of the beam position. The beam position was obtained from the voltage of **B22** using Eq.(2.1). The solid line represents the fit result with the quadrate target profile convoluted with Gaussian.

2.4 The spectrometer magnet

The spectrometer magnet was a dipole type with the overall weight of 300 ton. The dimension was 5655 mm in width, 3980 mm in height and 2120 mm in depth. To ensure the maximum vertical acceptance for electrons (± 23 degrees), the pole piece was made of two layers of cylinder with the diameters of 1760 mm and 2120 mm as shown in Figure 2.7. The gap between the poles was 907 mm. Other dimensions can be seen in Figure 2.7. The coil had 168 turns in each pole piece, and the normal operation current was 1560 A.

The magnetic field at the center of the pole piece was adjusted at 0.71 T to supply the integrated magnetic-field $\int B \cdot dl$ of 0.81 T·m from the targets to the radius of 1680 mm where the barrel drift chambers (BDC) were located.

Field Mapping and Calculation

It is important to know the precise magnetic field-strength everywhere in the acceptance since the amplitude of the $\int B \cdot dl$ is proportional to the rigidity of tracks. The magnetic field map were obtained by the calculation and compared to the hall-probe measurements. The magnet itself was symmetrically build from left to right and upstream to downstream, and top to down. The actual field, however, was distorted due to other magnetic materials which were the iron plate on the floor to support the magnet weight and the magnetic shield placed just front of the photomultiplier tubes of the aerogel Čerenkov counter. We calculated the magnetic field map using

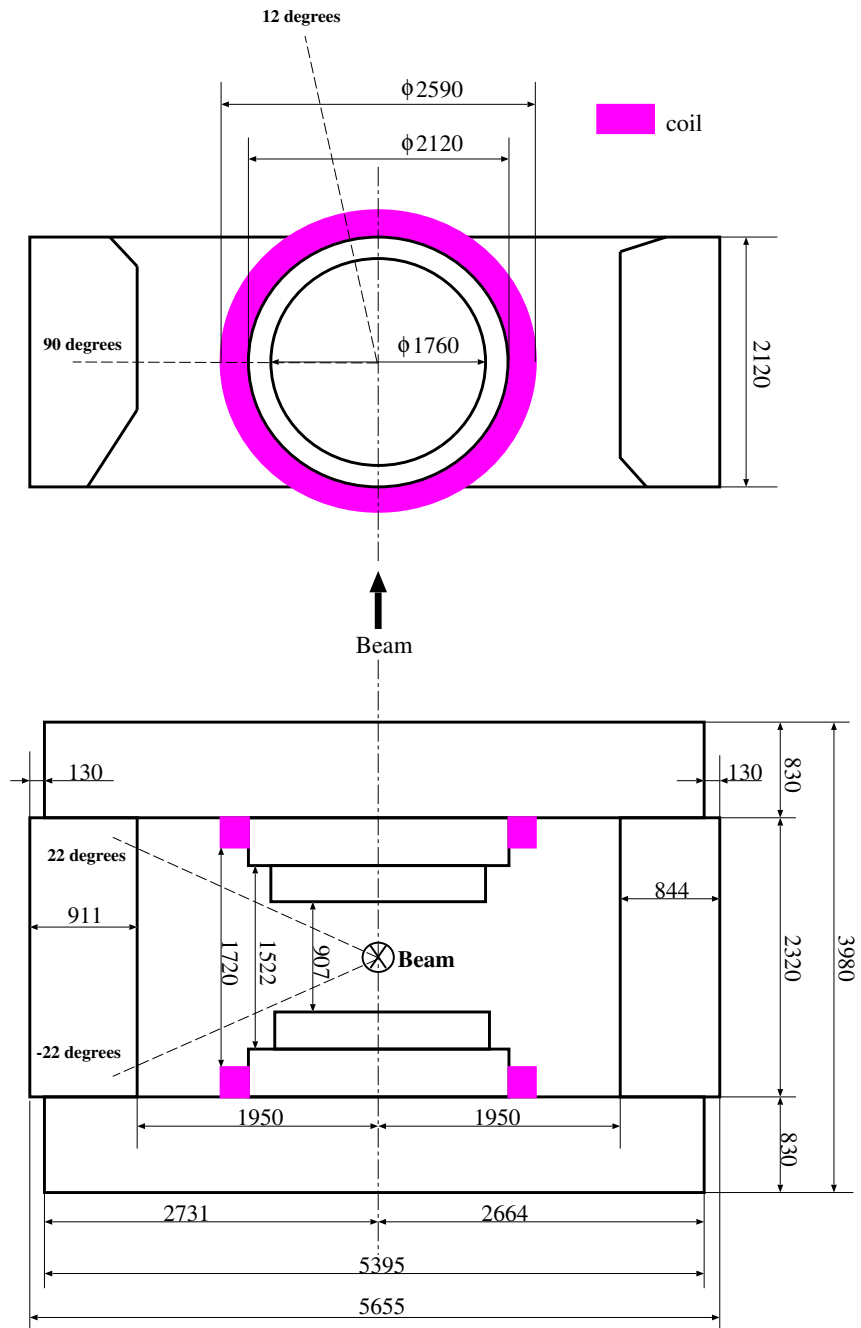


Figure 2.7: Schematic view of the spectrometer magnet. The dashed lines indicates the acceptance for electrons.

TOSCA [26], which performs a finite-element-method analysis. All the magnetic materials were taken into account in the calculation. Since the preliminary calculations and the measurements proved the left-right symmetry of the field, we performed a full calculation assuming the left-right symmetry to reduce the calculation time. The strength of the magnetic field on the x-y plane (the horizontal plane 400 mm below the beam line, which means 50 mm above the pole piece) is shown in Figure 2.8.

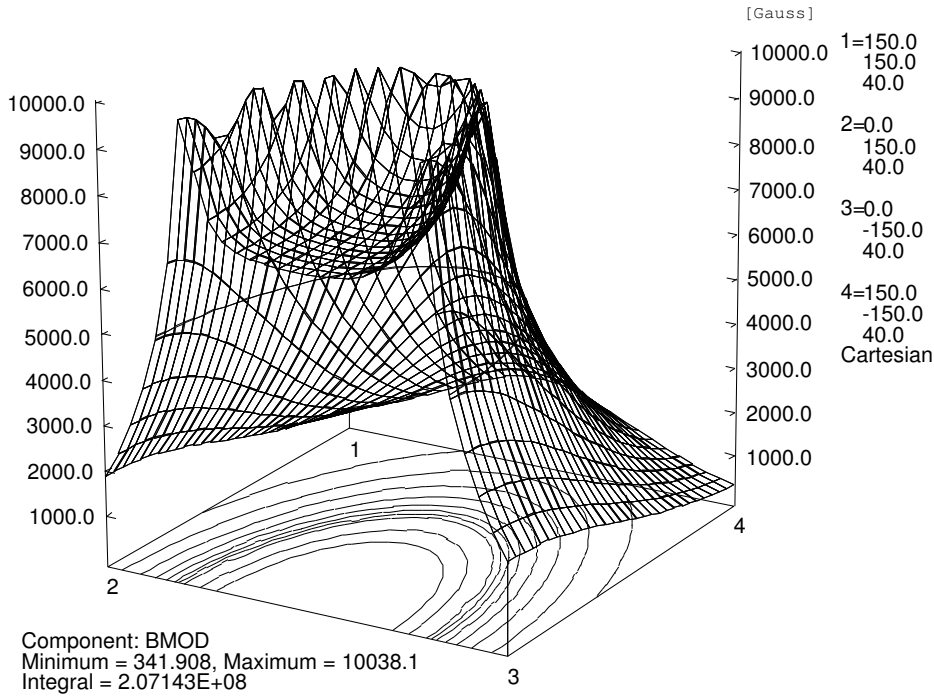


Figure 2.8: The calculated magnetic field map on the plane $z = -400$ mm.

We measured the magnetic field (B_x , B_y , B_z) with a set of hall probes which were placed orthogonal to each other in a cylinder. The cylinder can move back and forth in a tube placed along the x axis. The hall voltages of the probes were calibrated with a NMR probe before the measurement. The measured region was limited within the reach of the measurement device. We covered the region shown in Figure 2.9 by three different settings indicated by A, B and C. The measurements were performed on the 3-dimensional lattice points of 50 mm pitch. The relative position alignment among the three measured regions was done by minimizing the differences in the overlapped region. The hall probes are precisely orthogonal to each other but they could have a global rotations to the measurement coordinates which changes while traversing along the tube of the measurement device. We corrected such rotations with the measured field map around $z = 0$ mm plane, by making use of the fact that the horizontal magnetic field components B_x and B_y should be zero on the plane $z = 0$ mm where the magnetic field had good top-down symmetry. The three components of the magnetic field on the horizontal plane 363 mm below the beam line is shown in Fig. 2.10.

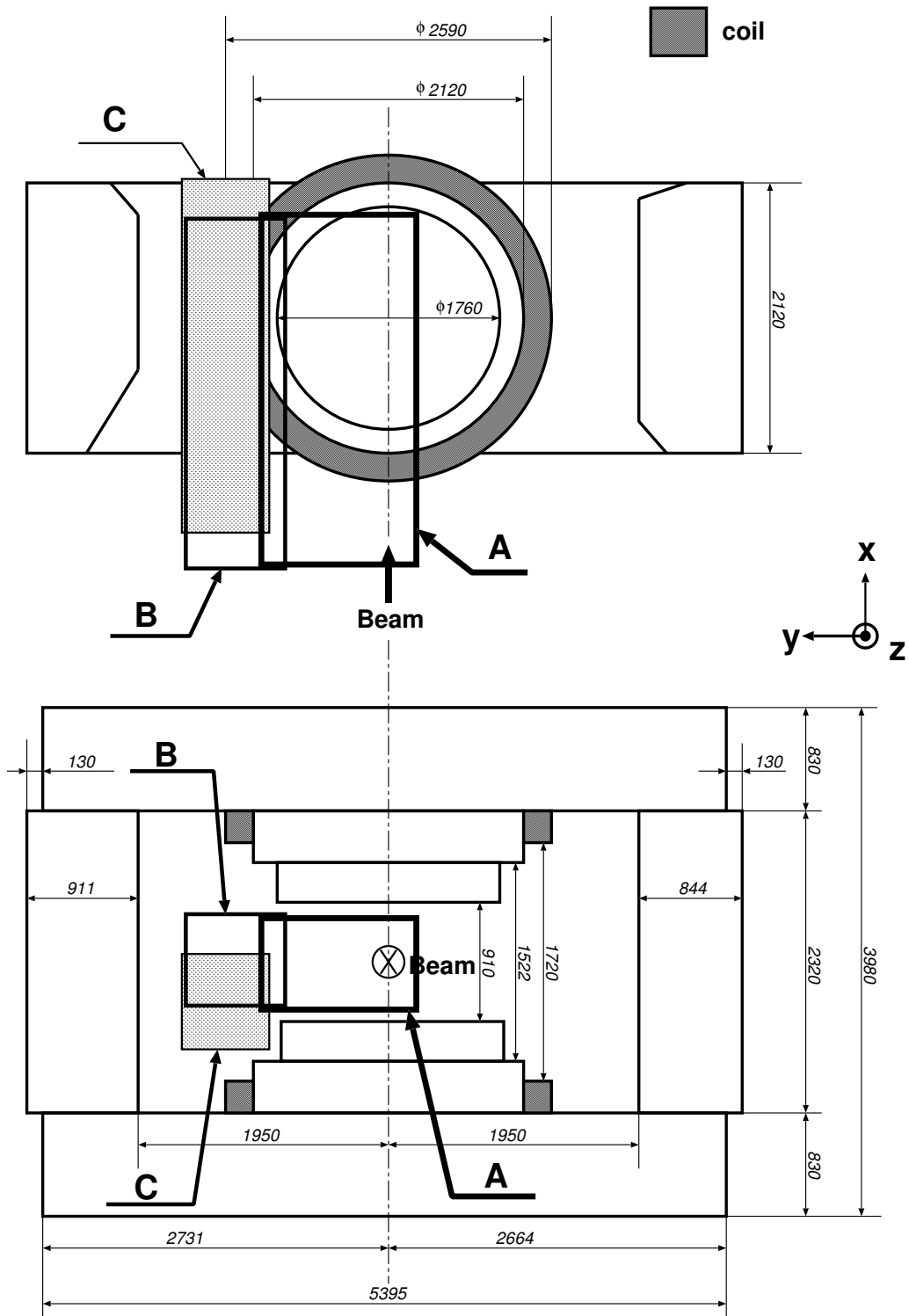


Figure 2.9: The three regions of the magnetic field measurements.

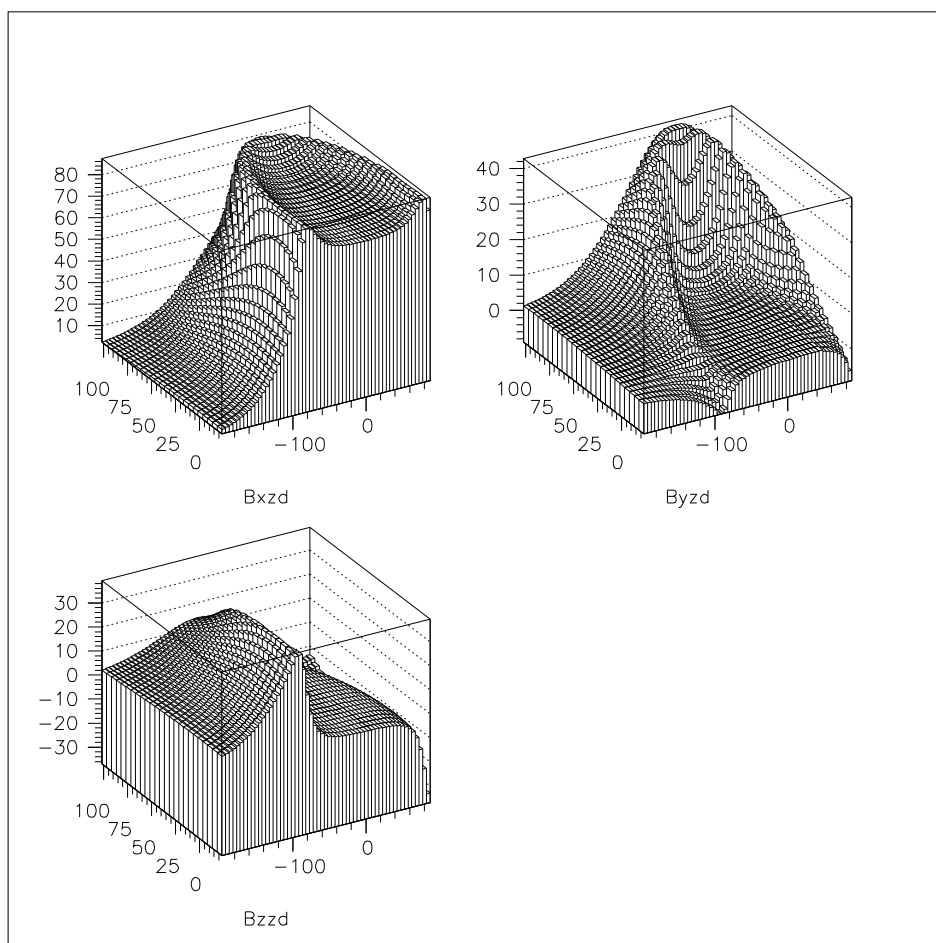


Figure 2.10: The measured magnetic field map on the plane $z = -363$ mm.

We evaluated the systematic uncertainty of the momentum determination caused from the inaccuracy of the magnetic field map. We generated the drift chamber hits for charged particle trajectories with the measurement map, and we fitted them using the Runge-Kutta method with the calculated map. We found that the discrepancy between the original momenta and the fitted results was within $0.2\% \pm 0.3\%$ in the momentum region from 0.5 to 2.0 GeV/c. The deviation of 0.2 % was corrected by scaling the calculated map. Figure 2.11 shows the difference of the track momenta between the measured and calculated map after the 0.2 % correction. Since the measured region was limited, the calculated magnetic field was used in the track finding and fitting.

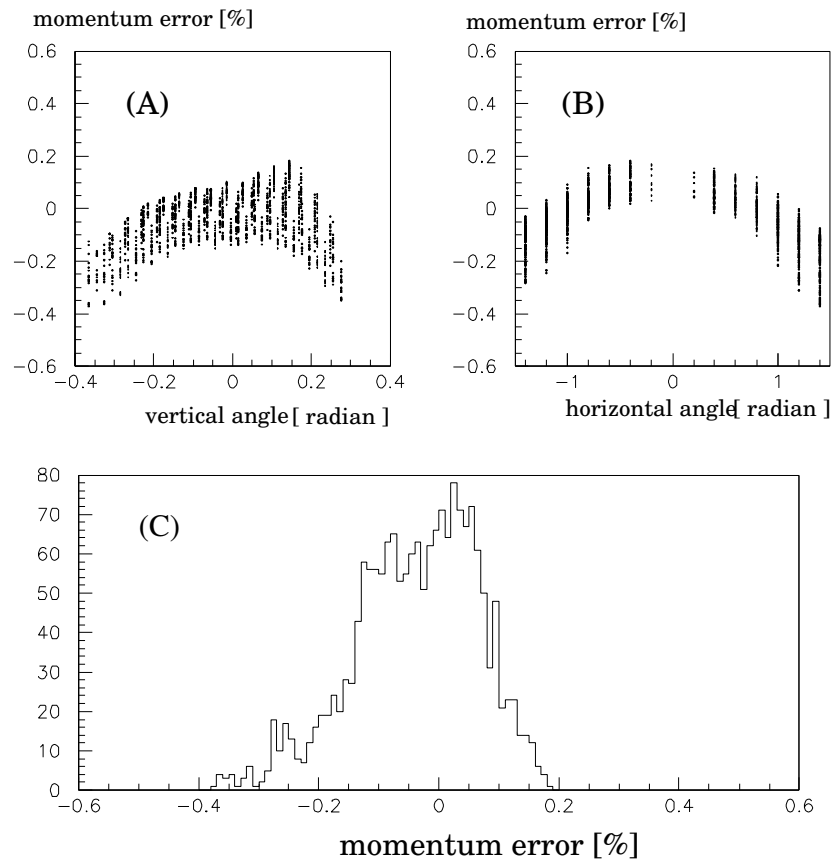


Figure 2.11: Possible uncertainty of the momentum determination due to the magnetic field map. Test tracks were generated with the measured map and reconstructed with the calculated map. The differences of the reconstructed momenta from the generated momenta were plotted as a function of the vertical angle in (A), and the horizontal angle in (B). The histogram (C) gives the projection of all the differences. 0.2% discrepancy was already corrected.

Run-by-run Correction

The magnetic field strength was monitored with NMR probe located at the center of the pole piece during the data taking period, at begin and end of each run, and the averaged value for each run was used for a run-by-run correction of the scale of the field map strength in the analysis. An actual drift was as small as 0.07%, as shown in Figure 2.12.

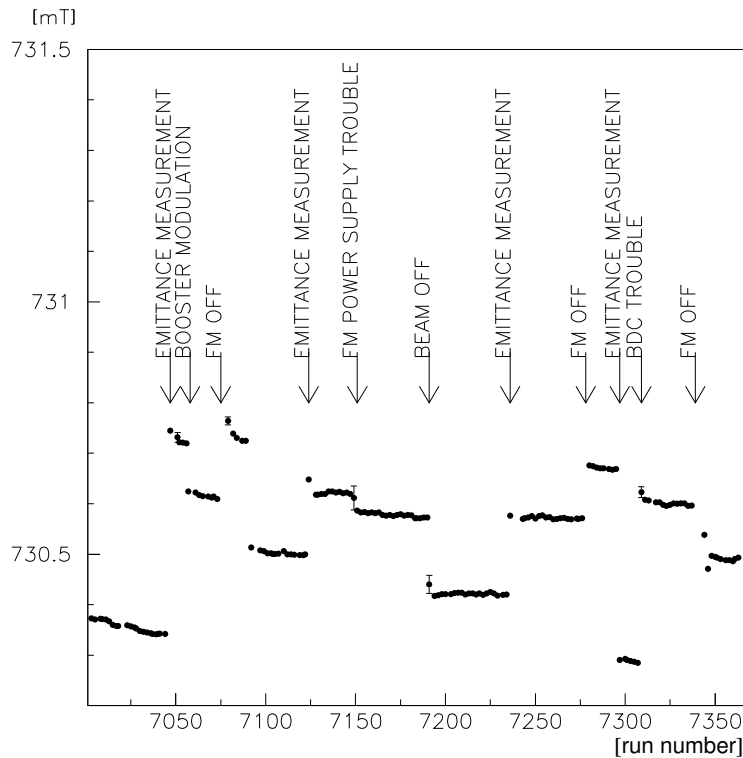


Figure 2.12: Averaged value of magnetic field strength for each run measured with a NMR probe. The comments are given when the magnet power supply was turned off. The error bar corresponds to the difference between the obtained values at the beginning and end of each run.

Magnet Trouble and Field Re-calculation

Before the cycle of the year 2001, we had a trouble in an isolation in the coils of the dipole magnet. We had originally 14 coils for the magnet, seven coils for each pole piece. Because of the trouble, we had to give up the two coils for the upper pole piece. To keep the top-down symmetry and the field integral as before, we switched off the corresponding two coils in the lower pole piece and operated the magnet with

14/10 times larger current, 2184 A than the nominal current of 1560 A. During the cycle of the 2001, we lost another coil in the upper pole piece due to a trouble in an isolation again. We gave up the three coils for the upper pole piece and turned on the all seven coils in the lower pole piece. To keep the field integral as before, we operated the magnet with 14/11 times larger current of 1985.5 A than the nominal of 1560 A. Since the available 11 coils are four in the upper side and seven in the lower side, the magnetic field became asymmetric from top to down. Under this condition, the magnetic field map was calculated again with TOSCA. The systematic uncertainty was estimated through the measurement of the magnetic field with a NMR probe for several sample heights at the center of the magnet. The measured values are listed in Table 2.3. The asymmetry of the measured magnetic field was reproduced well by the calculation. The difference of the absolute values between the calculation and the measurement were $0.49 \pm 0.03\%$, as shown in Figure 2.13. We scaled the absolute value of the calculated magnetic field to the measured value by a factor 0.00488. A systematic error from this difference, 0.03%, is negligible in the present experiment.

z[mm]	measured[mT]	calculated[mT]
446.5	698.367	701.910
225.5	699.225	702.792
1.5	706.540	710.069
-222.5	721.317	724.732
-446.5	730.180	733.540

Table 2.3: The measured and calculated magnetic fields for five z positions with the top-down asymmetric field. The operation current for the magnet was set to 1985.5 A.

2.5 Tracking

Tracking was performed with two kinds of drift chambers, a cylindrical drift chamber (CDC) and barrel-shaped drift chambers (BDCs).

2.5.1 Cylindrical drift chamber (CDC)

The schematic view of Cylindrical Drift Chamber (CDC) is shown in Figure 2.14. The outer diameter of CDC is 1760 mm, the inner diameter is 800 mm and the height is 840 mm. We located CDC on the pole piece of the spectrometer magnet. The acceptance of CDC was from $\pm 12^\circ$ to $\pm 132^\circ$ horizontally and $\pm 22^\circ$ vertically.

The CDC consists of ten radial layers of the drift cells, and they were grouped into three super-layers. The inner super-layer was in the radial region from 445.0 to 475.0 mm having three layers of drift cells (X, X', U), the middle super-layer was from 602.5 to 642.5 mm having four layers (V, V', X, X'), and the outer was from 800.0 to

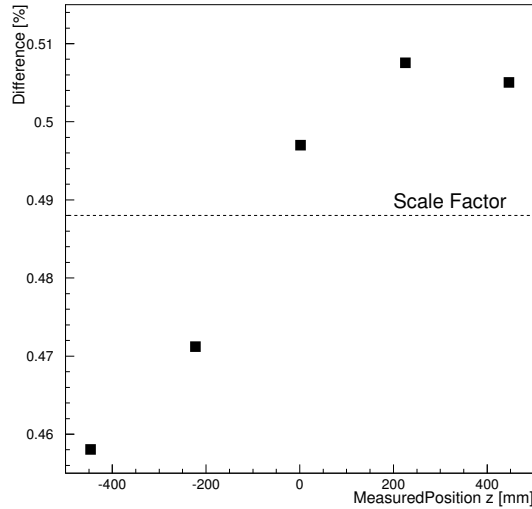


Figure 2.13: Differences between the measured magnetic field strength and the calculation with TOSCA. The vertical axis denote the ratio of the differences to the measured values. The horizontal axis is the z position of the measured points. The calculation was scaled by a factor of 0.488%, as shown by the dashed line.

830.0 mm having three layers (U, X, X'). In the X and X' layers the direction of wires was vertical and in the U and V layers the wires were tilted by about ± 0.1 radian. Argon-ethane mixed gas of 50% and 50% was used at 1 atm. The gas flow rate was about 100 cc/min.

The structures of the drift cells are shown in Fig. 2.15. The sense wires were gold-plated tungsten of $30 \mu\text{m}\phi$ and the potential wires were Be-Cu of $100 \mu\text{m}\phi$. The position of the wire was determined by the bush inserted at the end of the feed through pipes. We used the bush with a $80 \mu\text{m}\phi$ hole for the sense wires, so that the precision of the wire positioning was about $25 \mu\text{m}$. All the drift cells of CDC had the same horizontal angular coverage of 1.5 degrees with respect to the targets. Details of the wire arrangements were shown in Table 2.4.

We calculated the electrical field shape in the chamber cell and the relation between the drift length and the drift time (x-t relation) with the drift chamber simulation code GARFIELD [27]. The simulated drift line in the outer super-layer is shown in Figure 2.16 and the x-t relation is shown in Figure 2.17. The obtained x-t relation was used initially to determine hit positions in the drift length calibration.

The structure of CDC was designed to restrict its active region only to the spectrometer acceptance. The top and bottom end plates were semi-curved with 3 stages as shown in Figure 2.14. This structure was effective to gain the mechanical strength of the chamber frame and consequently to minimize the support structure within the spectrometer acceptance. On the end plates ceramic boards were inserted, which pro-

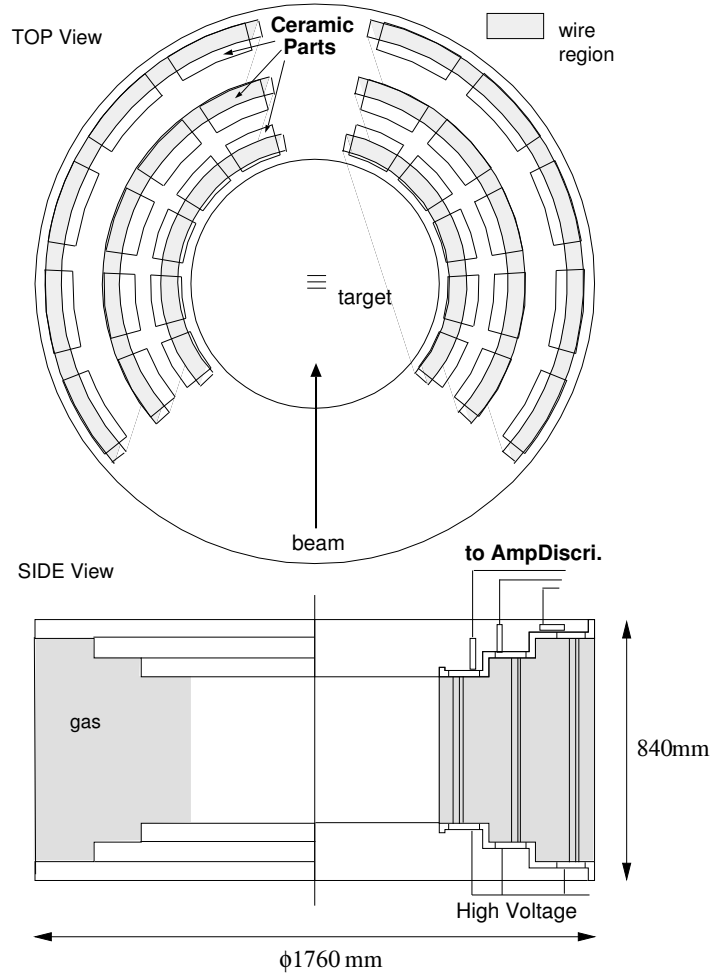


Figure 2.14: Schematic view of CDC.

Super Layer	Inner			Middle				Outer		
Layer	1	2	3	4	5	6	7	8	9	10
Wire Direction	X	X'	U	V	V'	X	X'	U	X	X'
Radial Location of Sense Wires [mm]	445	455	475	602.5	612.5	632.5	642.5	800	820	830
Wire Length [mm]	441	441	-	-	-	565	565	-	713	713
Cell Width [degree]	1.5	1.5	1.5	1.5	1.5	1.5	1.5	1.5	1.5	1.5
Cell Width [mm]	11.65	11.91	12.43	15.77	16.04	16.55	16.82	20.94	21.47	21.73
Tilt Angle [rad]	0	0	-0.1127	0.1116	0.1135	0	0	-0.1174	0	0
Number of Sense Wires	81	81	77	76/77 [†]	77/76 [†]	81	81	77	82	82

[†]left arm/right arm.

Table 2.4: The wire configuration of CDC.

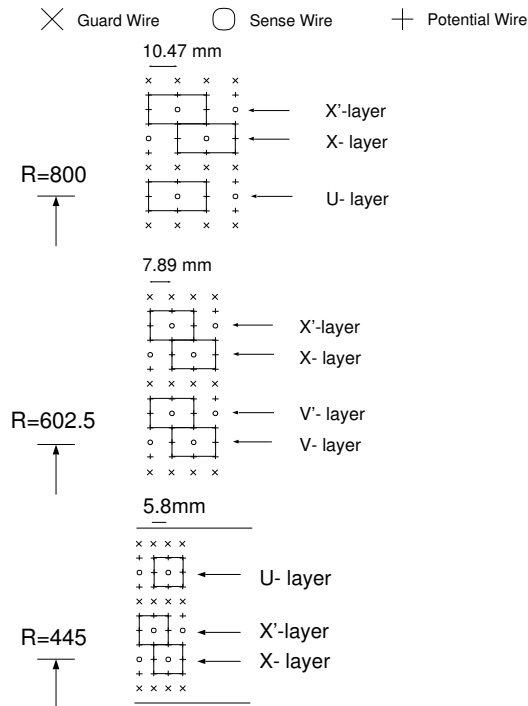


Figure 2.15: The cell structures of CDC.

vided the support to the feedthroughs and electrical connections.

The read-out electronics of CDC consisted of Amplifier-Shaper-Discriminator (ASD) ICs on a print circuit board mounted on CDC (ASD board), a LVDS-ECL converter and a time to digital converter (TDC). The ASD IC is developed for the Thin Gap Chambers in the forward muon trigger system of the LHC ATLAS experiment [29]. The block diagram of the ASD chip is shown in Figure 2.21. The measured (specification) gain of the pre-amplifier of the ASD is 360 (800) mV/pC, and the gain of the main amp is 4 (7). The output signal of the ASD board was sent to LVDS-ECL converter board via 10 m-long twisted-pair cables. From the LVDS-ECL converter, the signal was transferred to the counting house with 35 m-long twisted-pair cables.

When a minimum ionizing particle passed through one drift cell of CDC, it generated about a hundred ionizing electrons. The electric field around the wire amplified these electrons by 1.6×10^4 . Through the ASD, the pulse height of the signals before the discriminator was typically 240 mV for minimum ionizing particles. The threshold voltage of the discriminator was set from 5 to 18 mV for various CDC super-layers. ²

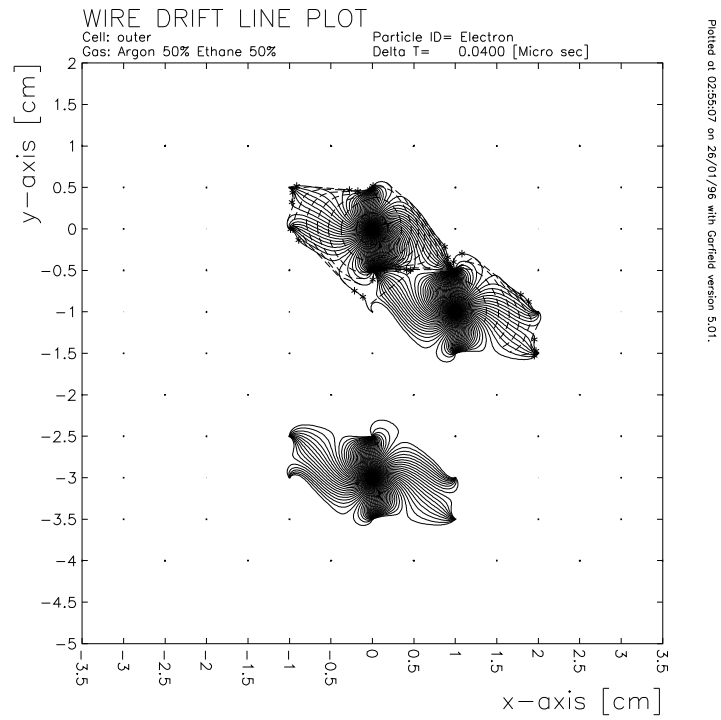


Figure 2.16: The simulated drift line in the outer super-layer (3 layers) in the magnetic field of 0.61T, which is the magnetic field strength at this location when the spectrometer magnet is fully excited.

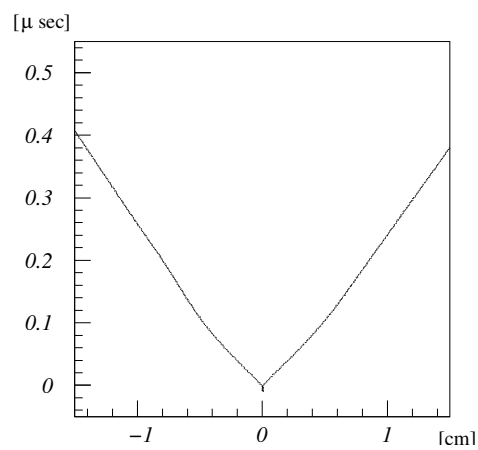


Figure 2.17: The calculated relation between the drift time and the drift length of the X-layer in the outer super-layer under the magnetic field of 0.61T

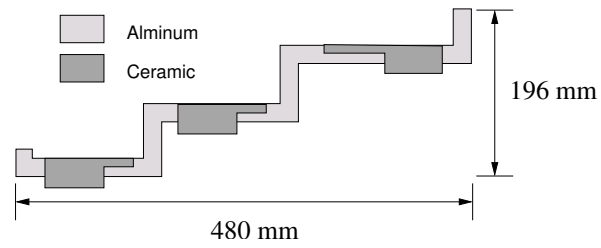


Figure 2.18: The cross section of the aluminum end plate and the ceramic plate.

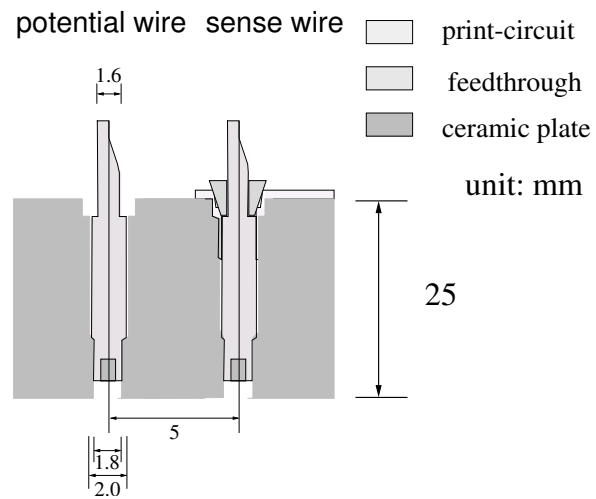


Figure 2.19: Schematic view of the feedthrough structure for the ceramic plate of CDC.

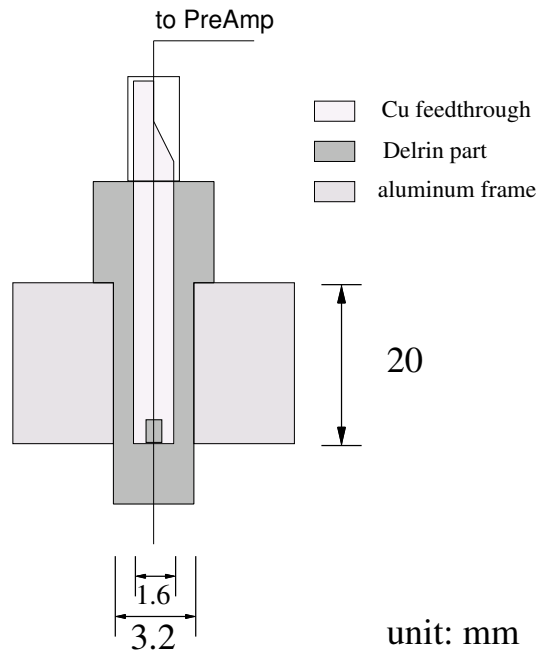


Figure 2.20: Schematic view (not to the scale) of the feedthrough structure for the one on the aluminum plate of CDC.

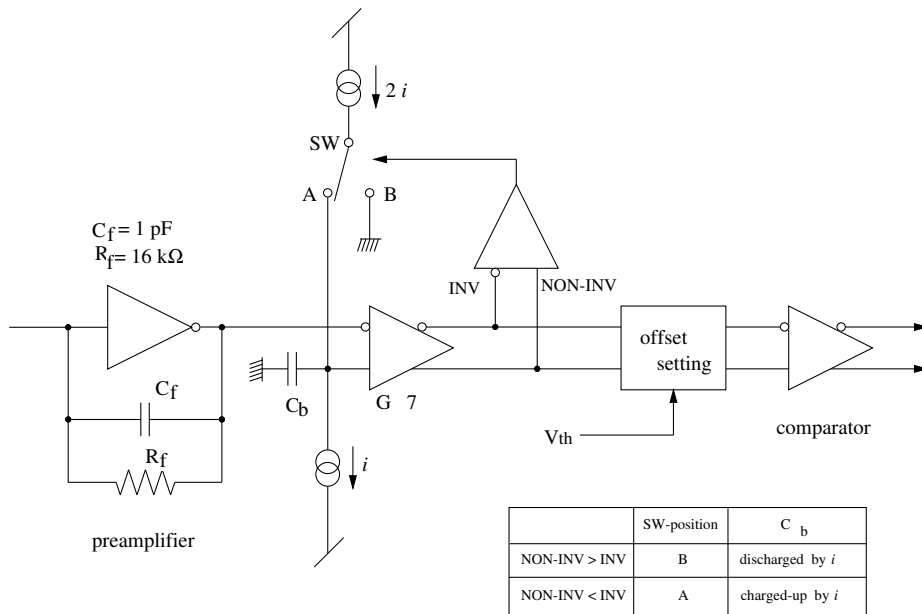


Figure 2.21: Block diagram of the ASD chip.

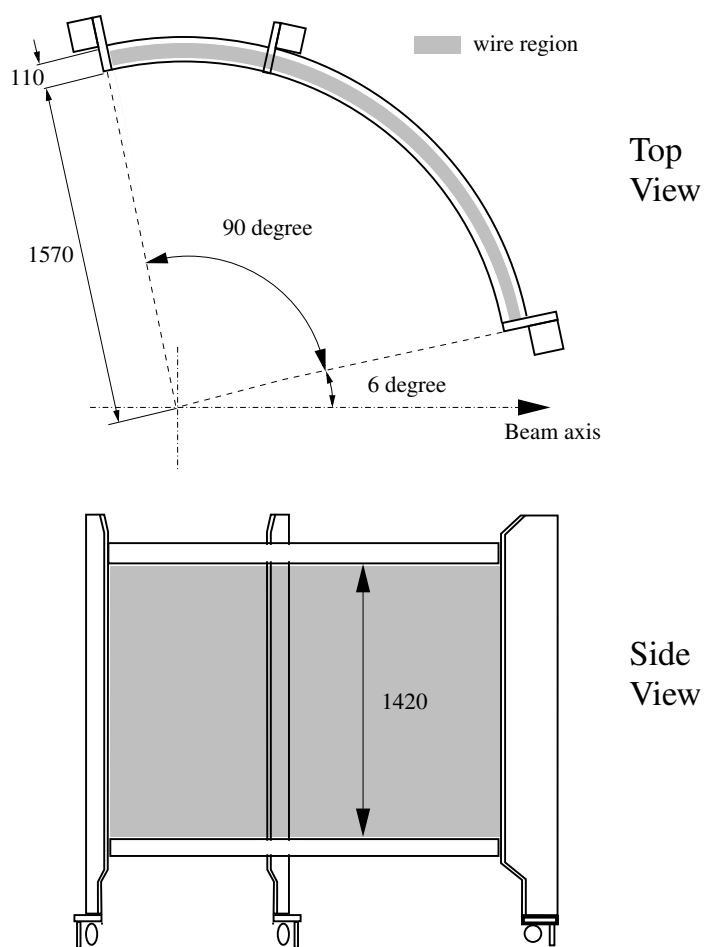


Figure 2.22: Schematic view of BDC.

2.5.2 Barrel-shaped drift chambers (BDC)

The structure of Barrel-shaped Drift Chambers (BDC) consisted of 90-degree arc-shaped end plates at the top and the bottom which were supported by three aluminum bars as shown in Figure 2.22. The inner radius was 1570 mm, the outer radius was 1680 mm and the height was 1420 mm. The acceptance of BDC is the same as CDC for the vertical coverage but with a smaller horizontal coverage from $\pm 7.5^\circ$ to $\pm 94.5^\circ$. The BDC's have 4 layers of drift cells with an XX'UV configuration, located at $r=1600$ to 1650 mm. In the X and X' layers the direction of wires was vertical and in the U and V layers the wires were tilted by about ± 0.1 radian. Argon-ethane mixed gas of 50% and 50% was used at 1 atm as same as CDC.

The structure of the drift cells is shown in Figure 2.23. All the drift cells of BDC had the same horizontal angular coverage of 0.75 degrees with respect to the target position. The size of the drift cells of BDC was the same as that of the outer super layer of CDC. The high voltage of -0.7 kV was applied to the potential wires, of +0.1 kV to the guard wires and of +1.5 kV to the sense wires. Details of the wire arrangements are shown in Table 2.5.

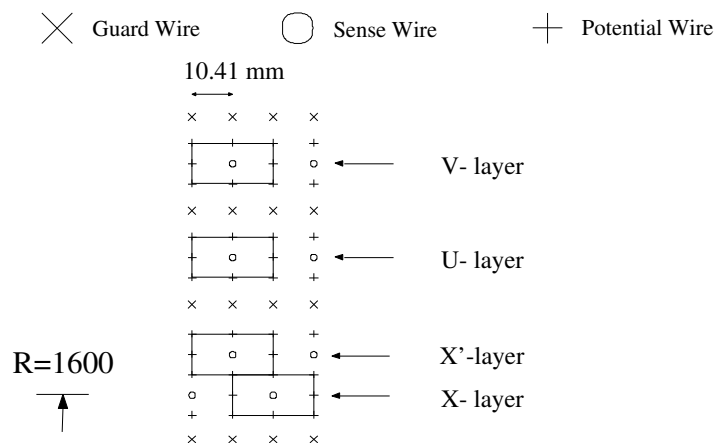


Figure 2.23: The cell structure of BDC.

The read-out electronics of BDC were the same as that of CDC and the threshold voltage of the discriminator was set at 13~15 mV.

Materials in the spectrometer and momentum resolution

The materials through the flight path of particles from the target to BDC are summarized in Table 2.6. By the detector simulation described in Sec. 4.2.4, which takes into account the position resolution of the chambers and the experimental effects, the

²The threshold voltage is magnified 20 times compared to the pulse height before the discriminator, the actual set up values were from 100 to 350 mV.

layer	1	2	3	4
wire direction	X	X'	U	V
location of sense wire from the center of the arc [mm]	1600	1610	1630	1650
wire length [mm]	1403	1403	-	-
cell width [degree]	0.75	0.75	0.75	0.75
cell width [mm]	20.81	20.94	21.21	21.47
tilt angle [radian]	0	0	0.1058	0.1071
number of sense wire	116	116	109	109

Table 2.5: BDC wire configuration.

momentum resolution for the electron is given by the formula [22],

$$(2.2) \quad \sigma_p/p = \sqrt{(1.37\% \cdot p[\text{GeV}/c])^2 + 0.41\%^2},$$

as shown in Fig. 2.24. Here, the fit for the trajectories was performed over two electron tracks simultaneously, requiring two tracks come from the common point on the target. The first term is due to the position resolution of the chambers, and next term is due to the Coulomb scattering.

2.6 Start timing counter

The time zero of an event was defined by the start timing counters (STC), since we could not count the beam protons one by one because of their high rate ($\sim 6\text{--}9 \times 10^8$ protons per spill). The schematic view of STC is shown in Fig. 2.25. We located STC at 380 mm from the center of the spectrometer, covering from $\pm 12^\circ$ to $\pm 60^\circ$ in the horizontal angle and $\pm 23^\circ$ in the vertical angle. In each arm STC was segmented into 8 units horizontally.

The scintillator of STC was made of Bicron BC404. The dimension of the scintillator segment was 400 mm in height, 40 mm in width and 5 mm in thickness. The scintillation light was transferred through light guides to a pair of photomultipliers attached with optical grease at the top and bottom ends. The photomultipliers were H6154 of Hamamatsu Photonics, whose diameter of the photo-cathode was 2 inches and structure of the dynodes was a fine-mesh type. The number of dynodes was 19 with the typical gain of 1×10^6 at the present field strength of 0.71 T. Since the coincidence rate of the top and bottom photomultipliers reached 1.5 M counts per spill in forward segments, the high voltage breeder was modified to supply enough current to the last three dynodes. The breeder circuit is shown in Figure 2.26. Typical breeder current was 0.4 mA which was increased to 4 mA at the last three dynodes. Discriminated signals from the top and bottom photomultipliers were fed into the mean timer and provided the timing of each segment. The timings of all the STC segments

Counter	material	radius [mm]	thickness X [mm]	λ_{rad} [mm]	X/λ_{rad} [%]
VTC	Ar-C ₂ H ₆ (50:50)	0.00	245.00	340350.0	0.072
	Wire(Cu-Be)	-	0.0173	14.3	0.121
	Wire(W)	-	0.0004	3.5	0.011
	Mylar	245.00	0.05	287.0	0.017
	air	245.05	134.95	304200.0	0.044
STC	scintillator	380.00	5.00	425.0	1.176
	lapping	385.00	0.20	287.0	0.070
	air	385.20	14.80	304200.0	0.005
CDC	Mylar	400.00	0.05	287.0	0.017
	Ar-C ₂ H ₆ (50:50)	400.05	479.95	340350.0	0.141
	Wire (Cu-Be)	-	0.031	14.3	0.217
	Wire (W)	-	0.0005	3.5	0.014
	Mylar	880.00	0.05	287.0	0.017
	air	880.05	19.90	304200.0	0.007
FGC	Mylar	899.95	0.05	287.0	0.017
	isobutane	900.00	660.00	169300.0	0.390
	acrylic mirror	1560.00	3.00	344.0	0.872
	aluminum cover	1563.00	1.00	89.0	1.124
	air	1564.00	5.95	304200.0	0.002
BDC	Mylar	1569.95	5.95	287.0	0.017
	Ar-C ₂ H ₆ (50:50)	1570.00	110.00	340350.0	0.032
	Wire (Cu-Be)	-	0.010	14.3	0.070
	Wire (W)	-	0.0001	3.5	0.003
SUM					4.458

Table 2.6: List of the materials and their radiation lengths from the center of CDC to the radius of 1680 mm where BDCs were located.

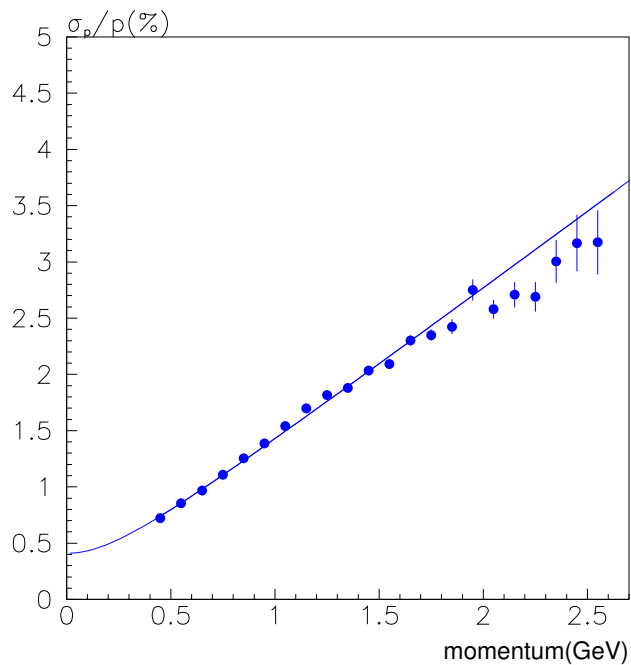


Figure 2.24: Momentum resolution for electron evaluated by the detector simulation. The solid curve is the fit result with Eq.(2.2).

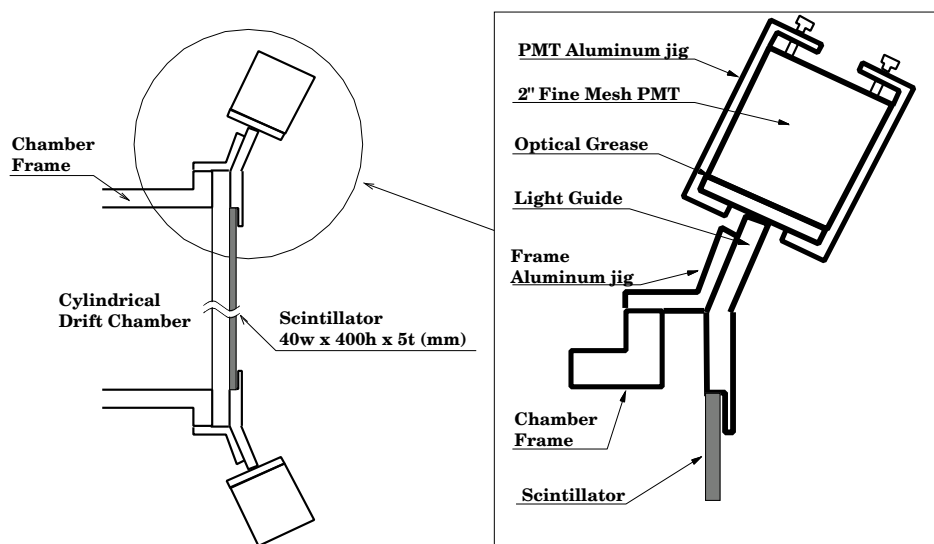


Figure 2.25: Schematic view of STC.

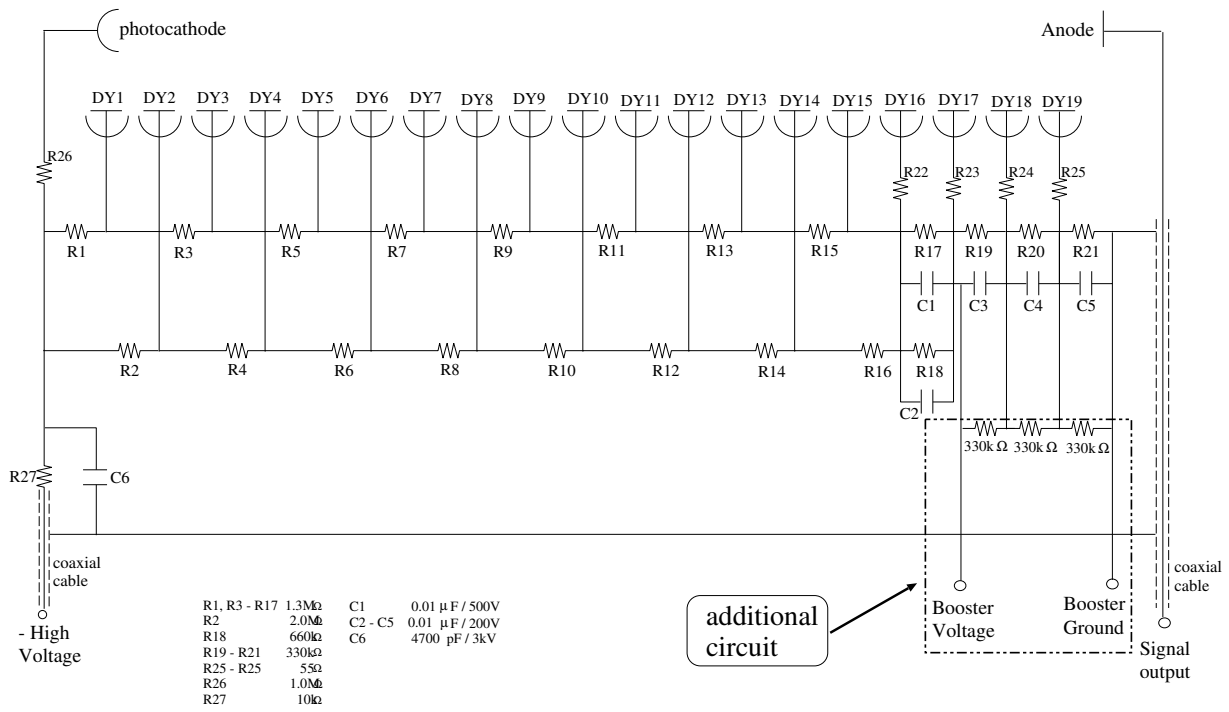


Figure 2.26: The breeder circuit of the photomultiplier used for STC (Hamamatsu H6154).

were adjusted within 1 nsec. These signals were OR-ed and used as the event time-zero signal. The counting rate of OR-ed signal was up to 6 M/spill. Typical time resolution of STC was obtained to be about 250 ps after the time slewing correction.

2.7 Electron identification counters

2.7.1 Front gas-Čerenkov counter

The first stage of the electron identification was done with the front gas-Čerenkov counters (FGC), which cover the whole region of the electron acceptance, from $\pm 12^\circ$ to $\pm 90^\circ$ horizontally and $\pm 23^\circ$ vertically. They were horizontally segmented into thirteen units in each arm so that one segment covered 6° . The cross section of FGC is schematically shown in Fig. 2.27, together with the light collection scheme.

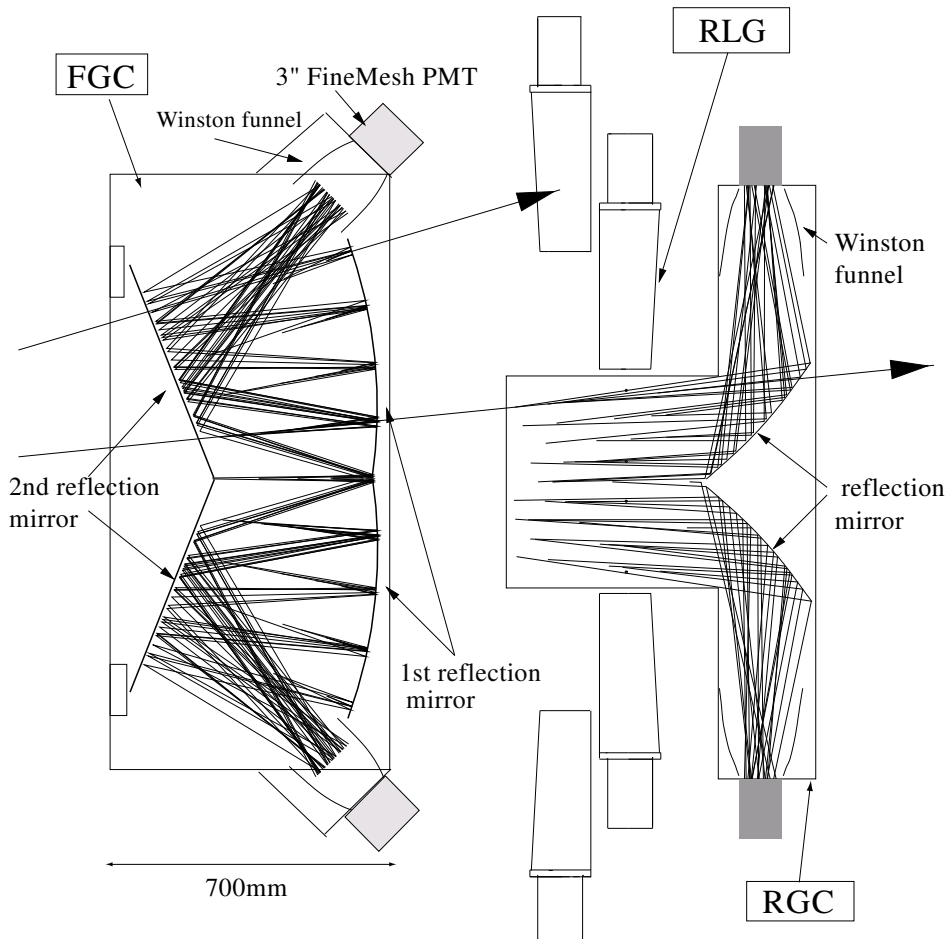


Figure 2.27: Schematic view of FGC, RGC and RLG.

Iso-butane gas with the refractive index of 1.00127 (1.0019) at room temperature

(0°C) was used as the Čerenkov photon radiator. The threshold momentum for pions is 2.7 GeV/ c at room temperature, and 2.3 GeV/ c at 0°C. The detector was operated at about 15°C. Since the path length of particles in the counter was rather short, we used the gas having high refractive index. Another merit of iso-butane was its transparency for the ultra-violet lights down to the wave length of 220 nm. It is important for the detection of the Čerenkov light because the intensity of Čerenkov light is higher at a short wavelength with a $1/\lambda^2$ dependence.

A radiated Čerenkov photons were reflected twice on the flat and the arc mirrors as shown in Figure 2.27. Thin mirrors were preferred to suppress multiple scattering. For the flat mirror we used 0.05 mm aluminized Mylar supported with a honeycomb backplane made of paper. The arc mirrors were made by a 3 mm-thick Acrylic plastic on which aluminum and SiO were successively evaporated. Light is reflected also at the side walls for the segmentation. Here, we used MgF₂-coated aluminized Mylar which has 88% reflectance for the wave length down to 200 nm.

The Čerenkov photons were focused with a Winston funnel [30] attached on the photomultipliers. They were also made by Al-SiO evaporated Acryl. Since the photomultipliers of FGCs were operated under the magnetic field of about 0.2 T, we used R5542 of Hamamatsu Photonics which had 19 stages of fine-mesh dynodes. For the detection of Čerenkov photons, their window was made of UV-transparent glass with a cut-off wavelength of around 240 nm and a diameter of 3 inches.

We tested a 1/2 sector model with no magnetic field. The vertical and horizontal incident angle dependence of the efficiency and the number of mean photo-electron were obtained using 500 MeV/ c electrons. The results are summarized in Figure 2.28 and 2.29. We obtained more than five photo-electrons in all the angular region required for the spectrometer. Please note that with the horizontal angle more than 0.15 radians the electrons pass more than one segment so that the pulse from the neighbor segment must be added. The horizontal incident angle of 0.2 radian corresponds to the momentum of 400 MeV/ c . Figure 2.30 shows the ADC spectrum of 1 GeV/ c pions. The pion rejection could be 8 % when the threshold is set to one photo-electron.

2.7.2 Rear gas-čerenkov counter

The rear gas-Čerenkov counters (RGC) which covered $\pm 12^\circ$ to $\pm 54^\circ$ horizontally and $\pm 6^\circ$ vertically with 7 horizontal segments in each arm. These regions corresponded to the kaon-arm acceptance, where particles fly through RGC and reach HD and FTOF counters located behind RGC. The cross section of RGC is schematically shown in Figure 2.27, together with the light collection scheme.

Iso-butane gas was used for the radiator as same as FGC. A radiated Čerenkov photons were reflected once on the arc mirror which was made by the 3 mm thick Acrylic plastic on which aluminum and SiO were evaporated. Light is reflected also at the side walls for the segmentation. The photons were focused with a Winston funnel [30] attached on the photomultipliers. We used R1652 of Hamamatsu Photonics with a diameter of 3 inches.

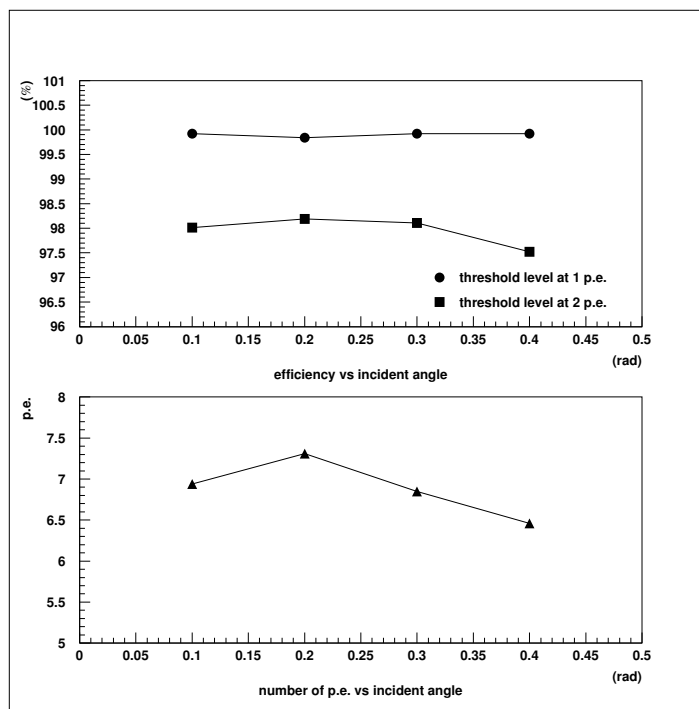


Figure 2.28: The efficiency and the number of photo-electron of the FGC test module as functions of the vertical angle of incident electrons. The triangles show the number of photo-electrons and the circles and the rectangles show the efficiency for the threshold levels corresponding to one photo-electron and two photo-electrons, respectively.

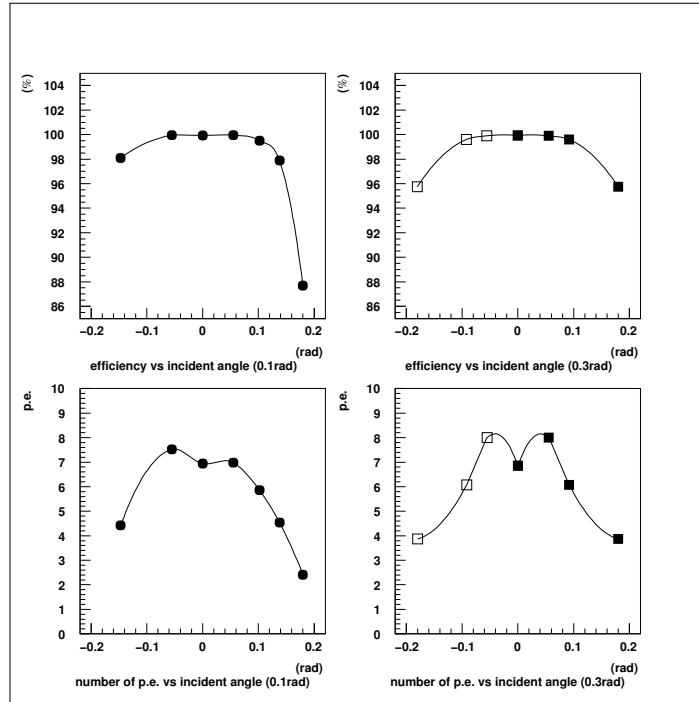


Figure 2.29: The efficiency (upper figures) and the number of photo-electron (lower figures) of the FGC test module as function of the horizontal angle of incident electrons. The closed circles are the data for the electrons with the vertical angle of 0.1 radian and the closed rectangles of 0.3 radians. The open rectangles are the points added assuming the symmetry.

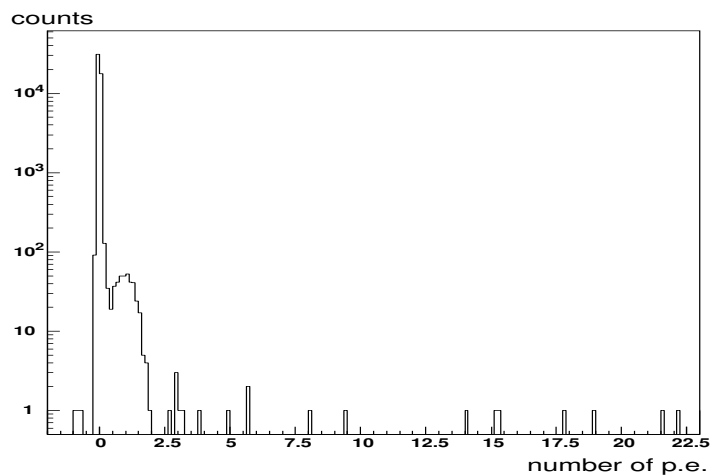


Figure 2.30: FGC response for 1 GeV/c pions. The horizontal axis is normalized to the number of photo-electrons.

We tested a 1/2 sector model with no magnetic field. The vertical and horizontal incident-angle dependence of the efficiency and the number of mean photo-electron were obtained using 1.0 GeV/ c electron as summarized in Figure 2.31 and 2.32. We obtained the number of photo-electrons of more than three in the acceptance required for the spectrometer. The data point at 0.0125 rad has less than three photo-electrons (Figure 2.31) due to the acceptance of the test module. The pion rejection is also demonstrated in Figure 2.33, which shows the ADC spectrum of 1 GeV/ c pions. When the threshold is set to 10 ADC channel, which realize the 99% efficiency for electrons, the pion rejection power is estimated to be 0.3%.

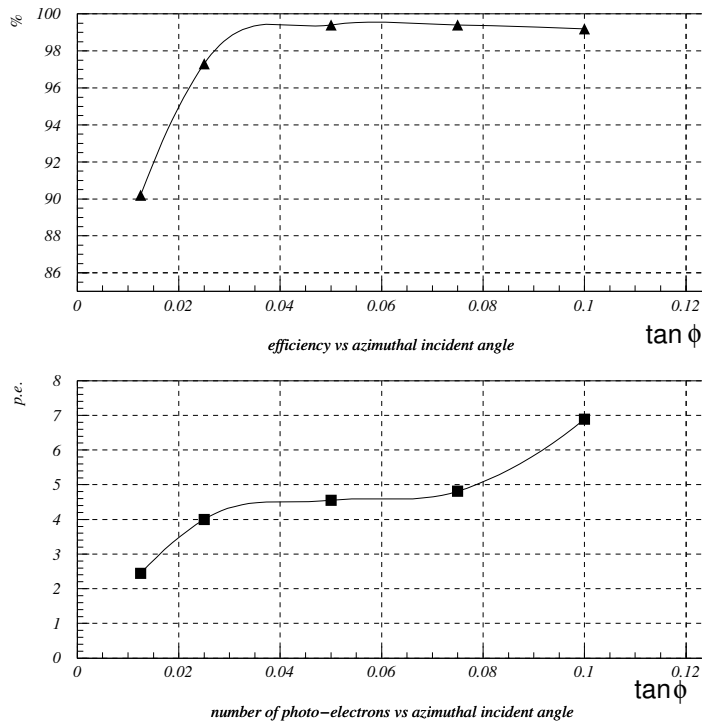


Figure 2.31: The efficiency (top figure) and the number of photo electron (bottom figure) of the RGC test module as functions of the vertical angle of incident electrons.

2.7.3 Rear lead-glass EM calorimeter

The rear lead-glass EM calorimeters (RLG) covered the same horizontal angle as RGCs with 12 segments in each arm, but vertically covered outside the kaon-arm acceptance, from $\pm 9^\circ$ to $\pm 23^\circ$. The one unit of RLG consisted of SF6W lead-glass block, which had the size of 340 mm height, 124 mm width and 114 mm thickness, and PMT 1652 of Hamamatsu Photonics with a diameter of 3 inches. The characteristics of SF6W is listed in Table 2.7. These units were recycled from the EM calorimeter of TOPAZ of TRISTAN at KEK.

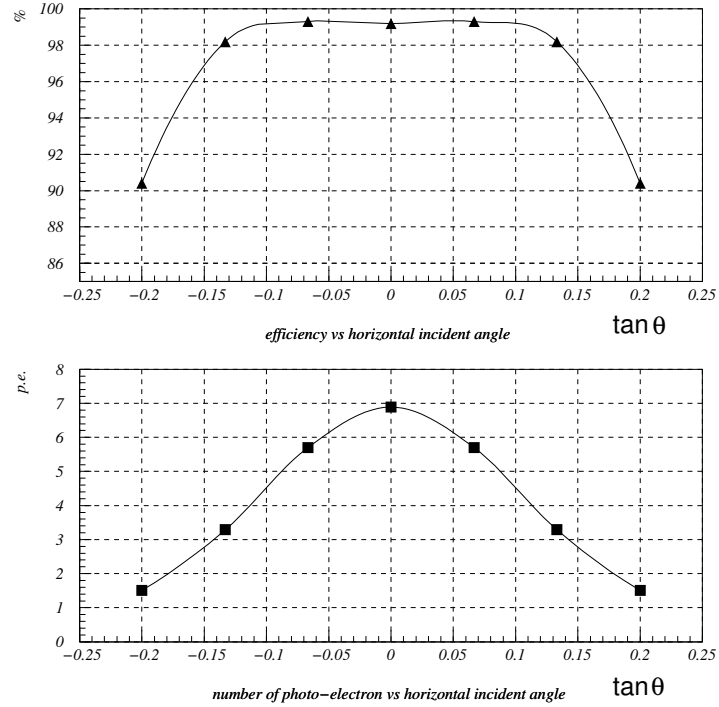


Figure 2.32: The efficiency (top figure) and the number of photo electron (bottom figure) of the RGC test module as function of the horizontal angle of incident electrons.

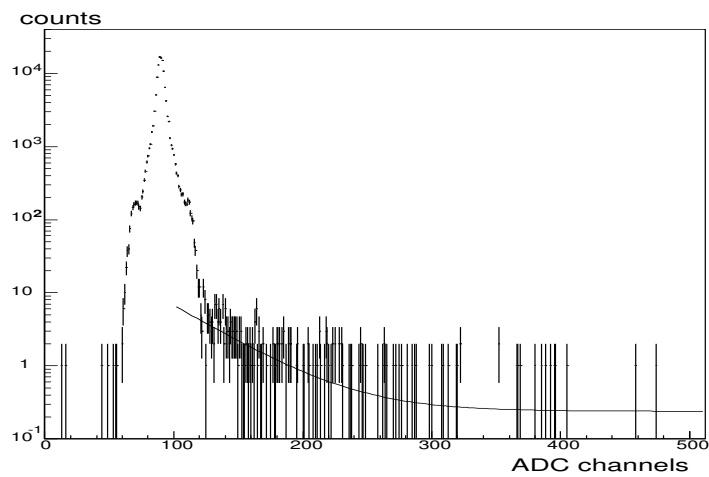


Figure 2.33: RGC response for 1 GeV/c pions.

The three types of the lead-glass calorimeters in the present experiment, RLG, SLG and FLG, used the same type of the recycled lead-glasses as the radiator, and these lead-glass blocks were arranged as particles come into the side of each block as shown in Figure 2.27, in order to cover a large acceptance with the small number of segments. Čerenkov photons from an EM shower were transported vertically by the total reflection to the photomultipliers at the end of the block. Although the effective thickness for the electron shower-development was only 7.5 radiation lengths, typical energy resolution of $15\%/\sqrt{E}$ was obtained for SLG in a test experiment as described in Sec. 2.7.4.

Radiation length	1.69cm
Refractive index	1.805
E_c	12.6MeV
R_M	2.8cm
Density	5.20g/cm ³

Table 2.7: Characteristics of SF6W [31].

2.7.4 Side lead-glass EM calorimeter

In the backward region, the second-stage electron identification was done by the side lead-glass EM calorimeters (SLG) which covered $\pm 57^\circ$ to $\pm 90^\circ$ horizontally and $\pm 23^\circ$ vertically with 9 horizontal segments in each arm. The schematic view of the cross section of FGC and SLG is shown in Figure 2.34.

We reuse the lead-glass calorimeter blocks same as RLG. For SLG, we reshaped and re-polished the blocks in Tochigi Nikon Corporation into a rectangular shape from the original tapered shape, and five units of the lead-glass blocks were stacked vertically and glued epoxy resin to form one segment of the calorimeter. The one segment of SLG had the size of 1650 mm height, 120 mm width and 110 mm thickness. We placed SLG along the return yoke of the magnet.

Čerenkov photons from an EM shower were transported vertically by the total reflection to the photomultipliers at the top and bottom ends. We used R1911 of Hamamatsu Photonics with a diameter of 3 inches.

A test experiment was done with a one-segment model. The position dependence of the light yield was obtained using a 500 MeV/ c electron beam. Although the light yield decreased by 75% in each block as shown in Figures 2.35, the sum of the both end was almost flat. Typical response for pions and electrons was obtained as shown in Fig. 2.36. Typical energy resolution of $15\%/\sqrt{E}$ was obtained. By keeping 95% efficiency for electrons, the pion rejection of 2% was achieved.

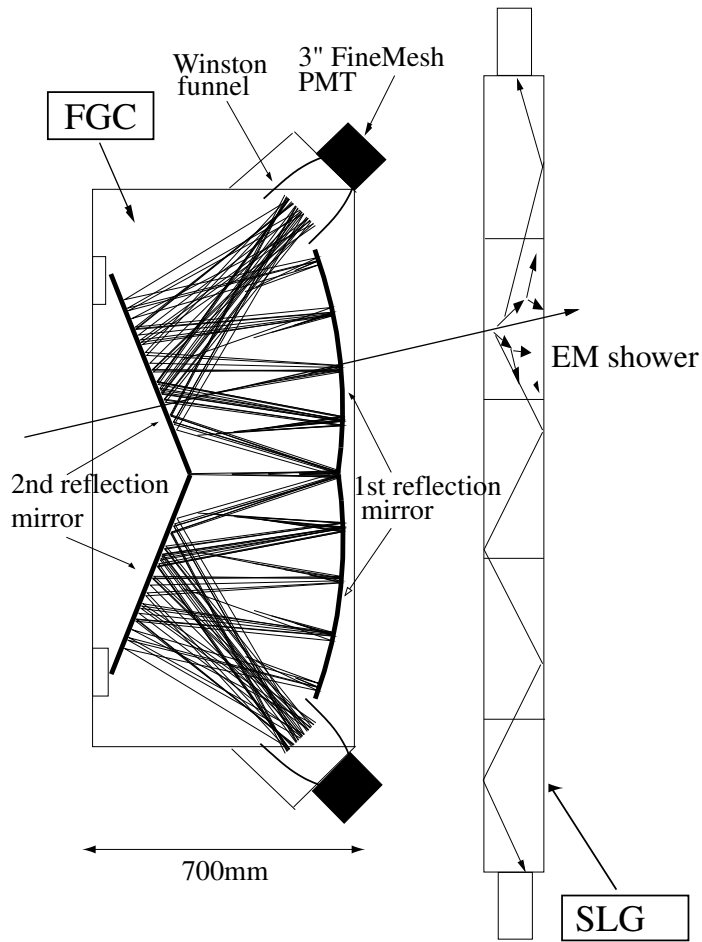


Figure 2.34: Schematic view of FGC and SLG.

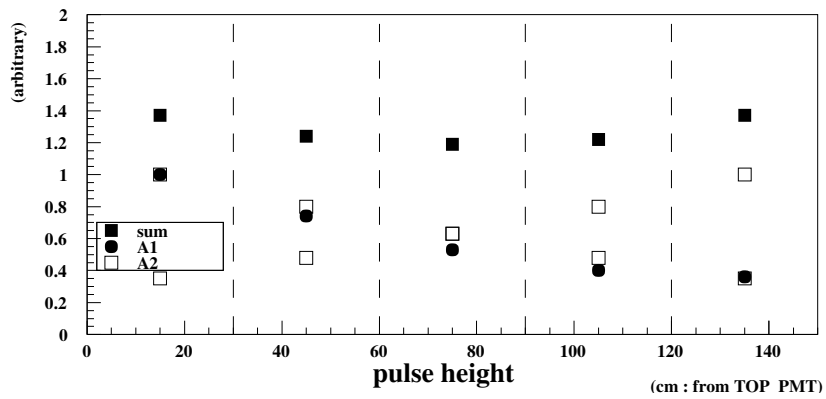


Figure 2.35: Vertical position dependence of the light yield for SLG. The open rectangles and closed circles are the light yield from the top and the bottom PMTs. The closed rectangles are for the sum.

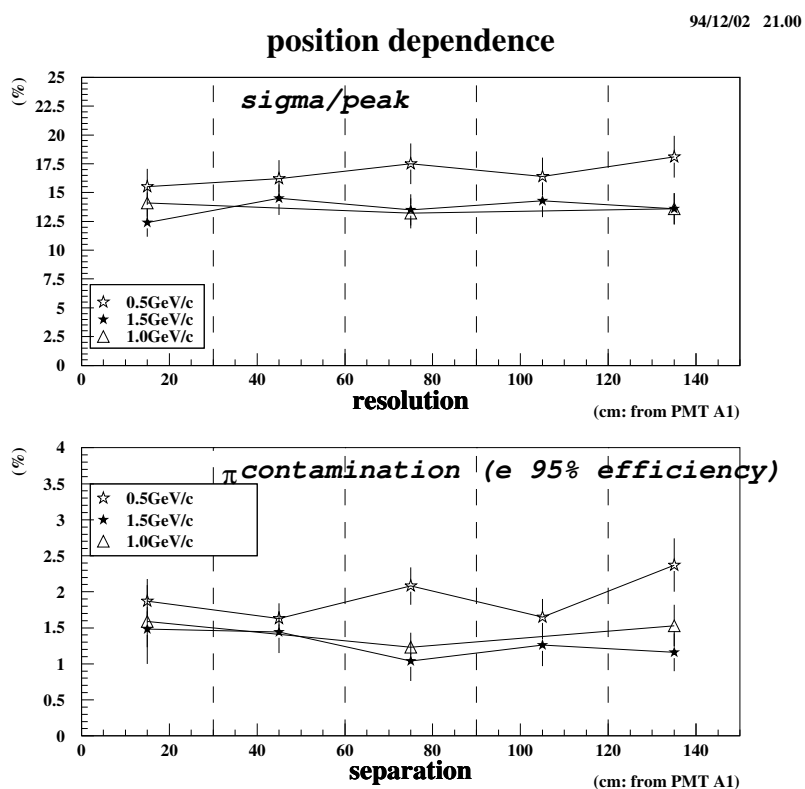


Figure 2.36: The vertical position dependence of the energy resolution (top) and the pion rejection power (bottom) of SLG.

2.7.5 Forward lead-glass EM calorimeter

The forward lead-glass EM calorimeters (FLG) was newly installed in the year 2000. FLG was located just behind the FTOF wall, the most forward region of the spectrometer, to cover the same acceptance as RGC in each arm. FLG has 24 segments in the left arm and 16 segments in the right arm. The 8 segments to cover the most right end of the acceptance were omitted due to the space limitation of the experimental area.

We reused the TRISTAN/TOPAZ lead glass calorimeter blocks as same as RLG and SLG. One segment of FLG consisted of three lead-glass blocks. Only the center block was reshaped and re-polished at Tochigi Nikon Corporation into a rectangular shape from the original tapered shape. The three blocks of the lead-glass blocks were stacked vertically and glued with epoxy resin, as shown in Figure 2.37. The one segment of FLG had the size of 950 mm height, 124 mm width and 110 mm thickness.

Čerenkov photons from an EM shower were transported vertically by the total reflection to the photomultipliers at the top and bottom ends. We used R1652 of Hamamatsu Photonics with a diameter of 3 inches.

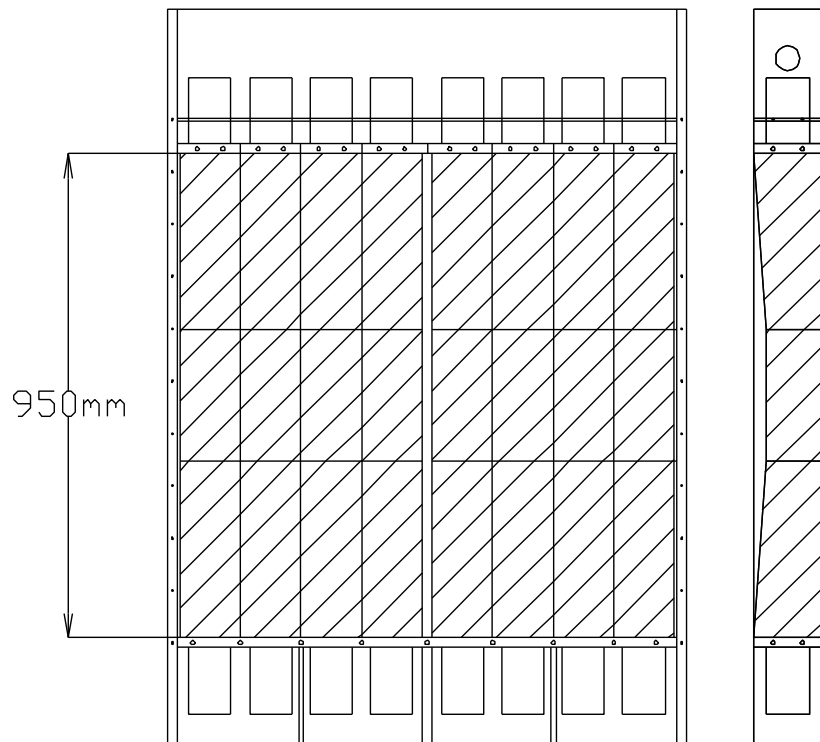


Figure 2.37: Schematic view of FLG. The shaded areas are lead-glass radiators.

2.8 Trigger

The schematic diagram of the trigger control system is shown in Fig. 2.38. The trigger logic for e^+e^- pairs had three levels, and that for K^+K^- pairs had two levels. The both trigger logics worked simultaneously.

In the year 2001, we collected the data with both electron and kaon trigger. In the year 2002, we collected only the electron data. Since we obtained enough event reduction by the first level trigger logic for the electron triggered events, we switched off the second and the third level electron trigger during the 2001 and 2002 data acquisition.

The hit signals from the counters and the chambers were sent to the first level trigger logics. If the condition of the electron first level trigger logic or the kaon first level trigger logic was fulfilled, the counter signals were held and the status of the frontend electronics was set as “busy” state. Then the gates for ADC were opened and the common start or stop timing signals for TDCs were sent. The higher level trigger logic was invoked at the same time. The busy state was kept until the clear signal was generated.

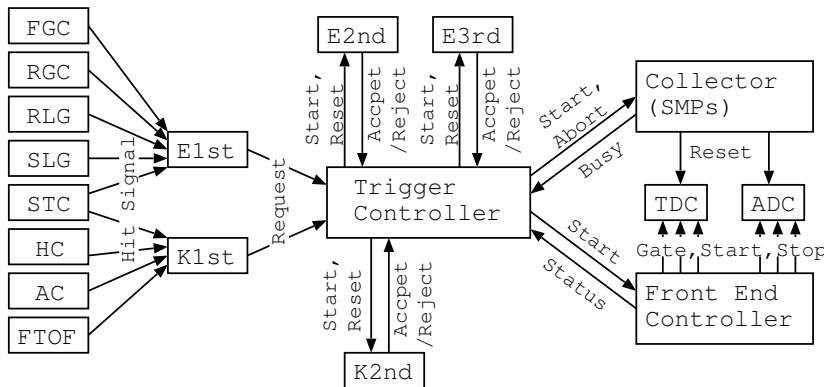


Figure 2.38: The trigger control system.

If the triggered event fulfilled all the levels of the electron or kaon trigger requirements, the event accept signal was issued and the data in the ADC and TDC modules were transferred to the memory modules. When the data transfer was completed, the busy state was cleared and the trigger logic became ready for the next event. In this case, typical duration of the busy state was $600 \mu\text{s}$.

If the event did not satisfy the higher level trigger logic, the clear signal was sent to the ADCs and TDCs and the busy state was also cleared. In this case, typical duration of the busy state was $50 \mu\text{s}$.

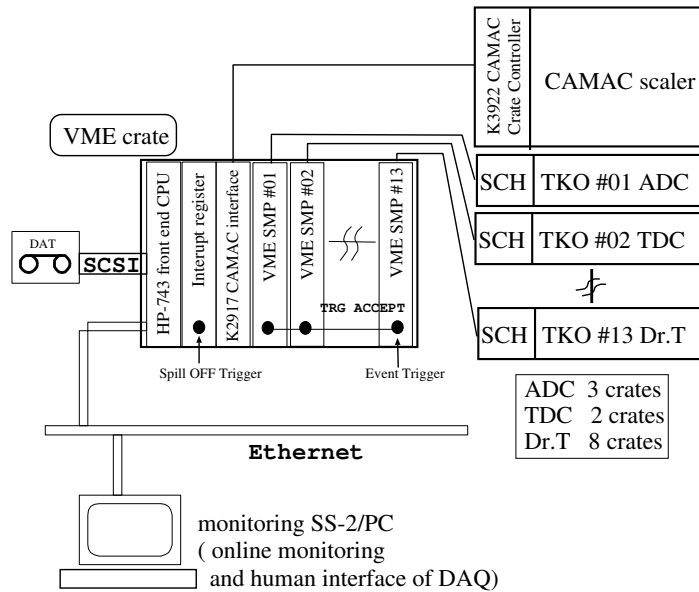


Figure 2.40: The schematic view of data acquisition system.

The Hewlett-Packard Model 743 (HP-743), VME on-board workstation, played a main role in the front-end data-acquisition system. There were thirteen Super Memory Partner (SMP) modules and a Kinetic K2917 VME-CAMAC interface-board in the VME crate. There were also thirteen TKO crates, two of them contain high resolution TDCs, three of them ADCs, and eight of them TDCs for drift chambers (Dr.T). The SMPs work as an interface module between the VME bus and the TKO bus via the Super Controller Head (SCH) module which was installed in each TKO crate.

Once the trigger signal was supplied to the ACCEPT input in the front panel of SMP, data scanning for all the channels of ADC's and TDC's in the TKO boxes was performed by SCH's, and the scanned data were stored in the local memories in SMPs. A busy signal was issued by SMPs during the scanning of the data, and further triggers were prohibited by the trigger control system. The process was repeated during the spill on, and at the spill end, these stored data were read out by HP-743 via VME bus and written in the digital data storage (DDS-4) tape, as well as the scaler data via the VME-CAMAC interface boards connected to the Kinetic K3922 CAMAC crate controller.

Software for the data collection, recording, transfer and monitoring was written in programming language C/C++. The data collection process (collector), the recording process (recorder) and transfer process (sender) were also running on HP-743, on which HP-RT v2.0 was operated.

The "collector" read the accumulated data on SMPs and CAMAC scalers through the VME bus at the timing of the spill-end notified by the VME interrupt register. Device drivers for TKO and CAMAC on HP-RT, used in "collector", were developed

to about 1k event per spill, and the live time of the data acquisition system was about 56%.

In 2002 beam time, the data are also transferred to Mass Storage system in a semi-realtime way. The recorded data on the DDS-4 tape are read out by another IBM PC (Linux) in the counting house, transferred to RIKEN-CCJ [39] via Internet using the command `bbcp` [40] and archived in HPSS [41] in CCJ. The typical transfer rate between KEK and RIKEN was about 2 Mbyte/sec. The amount of the data taken was about 1.2 Tbyte in 2001 and about 1.1 Tbyte in 2002.

Chapter 3

Analysis

3.1 Electron trigger data set

In this thesis, we report the analysis results of the electron-triggered data collected for 34 days in November 2001 and 32 days from February to March 2002. In 2001, we recorded 3.1×10^8 events with electron triggers on tapes. The number of used beam protons on targets were 3.8×10^{14} over 435 k spills. The average proton intensity was 8.7×10^8 per spill. In 2002, we recorded 5.1×10^8 events using 3.2×10^{14} protons on targets over 507k spills. The average proton intensity was 6.3×10^8 per spill. The beam and the target conditions are summarized in Table 3.1. In 2001 we took data with both the kaon and the electron triggers while in 2002 we took only the electron-triggered data.

Table 3.1: The beam and the target conditions.

	2001	2002
averaged beam intensity [protons/spill]	8.7×10^8	6.3×10^8
target configuration (interaction length [%])	Cu (0.054) $\times 2$, C (0.11)	Cu (0.054) $\times 4$, C (0.21)
number of events	3.1×10^8	5.1×10^8

In the following sections we describe calibrations and alignments of the detectors, track finding and fitting procedures, and selection criteria for the final e^+e^- sample with the electron identification counters.

3.2 Calibration

3.2.1 Drift time measurement and determination of drift length

For the drift time measurements of CDC and BDC, we used TKO 32-channel drift-chamber TDC modules (Dr.T II) with a common-stop logic produced by Rinei Precision

Instruments Corporation (REPIC). The full scale of this module is $1 \mu\text{s}$ and the typical time resolution is 0.35 ns . The time gain of Dr.T II was obtained with use of a CAMAC TDC tester (RPC070) produced also by REPIC. The tester has a time jitter of 55 ps for $1 \mu\text{s}$ full scale. The obtained time gain was typically $0.70 \pm 0.01 \text{ ns/channel}$.

We determined the relative time offset of all the CDC and the BDC signals with respect to the event time-zero using the drift time spectra. The time spectra had an edge of minimum drift length as shown in Fig. 3.1(a). The peak position of the differentiated time spectrum around the edge (Fig. 3.1(b)) provided the relative time offset for each wire.

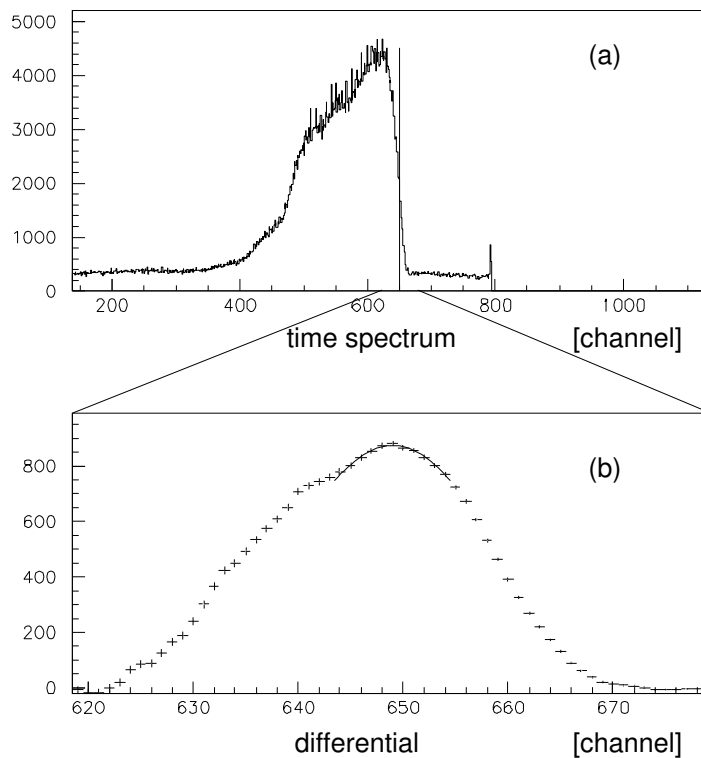


Figure 3.1: Typical TDC spectrum (a) and its differential (b).

This calibration was done run by run to cope with the possible temperature dependent drift in signal cable delays and in the propagation time of the trigger logic. The run dependence of the time offset was shown in Fig. 3.2. The typical drift was within 3 ns .

In order to obtain the hit position x in a drift cell from the measured drift time t , the $x-t$ relations for every type of the drift cells were initially obtained with the drift chamber simulation code GARFIELD [27]. By using the initial $x-t$ relations, hit positions were temporarily given and the trajectories of charged particles were reconstructed using the Runge-Kutta fitting method described in Sec. 3.3. We iteratively improved the $x-t$ relations to minimize systematic shifts of residuals between the tracks and the

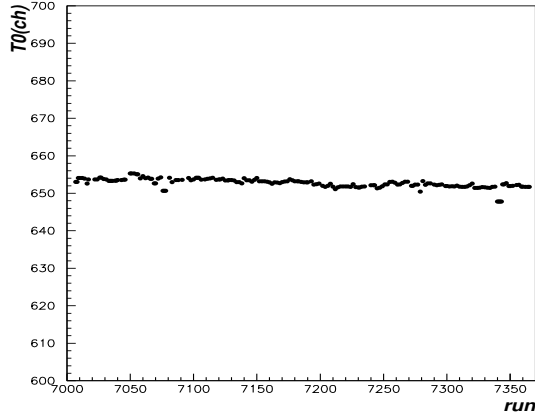


Figure 3.2: Run dependence of time offset of a typical wire in the year 2002.

hit positions as a function of drift length, by scaling the drift velocity and shifting the common time zero in the $x-t$ relations. The effect of the incident angle of tracks with respect to the drift cell was small and neglected. Figure 3.3 shows the residual distributions in CDC. We obtained typically $350 \mu\text{m}$ of the position resolution as shown in Figure 3.3. To reproduce the observed residual distributions more precisely, we practically introduced a double Gaussian formula as the the position resolution of the tracking devices. We iteratively determined the widths and the amplitude ratios of the two Gaussians by the Monte-Carlo track simulation with those two-Gaussian resolutions to reproduce the observed residual distributions. The detail of the procedure can be found in [28]. Table 3.2 shows the obtained position resolution in each chamber layer.

super layer	layer	σ_1 [mm]	σ_2 [mm]	ratio
CDC inner	(X,X',U)	(0.197, 0.203, 0.286)	0.595	0.436
CDC middle	(V,V',X,X')	(0.238, 0.217, 0.183, 0.181)	0.644	0.367
CDC outer	(U,X,X')	(0.285, 0.212, 0.261)	0.718	0.395
BDC	(X,X',U,V)	(0.292, 0.289, 0.340, 0.261)	0.661	0.488

Table 3.2: Estimated intrinsic resolution of the chamber layers. The values σ_1 are the widths for the main component of the double Gaussian distribution, σ_2 are those for the second component, and “ratio” are the amplitude ratios of the second/main.

3.2.2 Global position alignment of tracking devices

In the present analysis, the origin of the coordinate was set at the center of CDC. All the other chambers and the counters were aligned to the CDC coordinate. The magnet position with respect to CDC was measured by surveys performed before and after

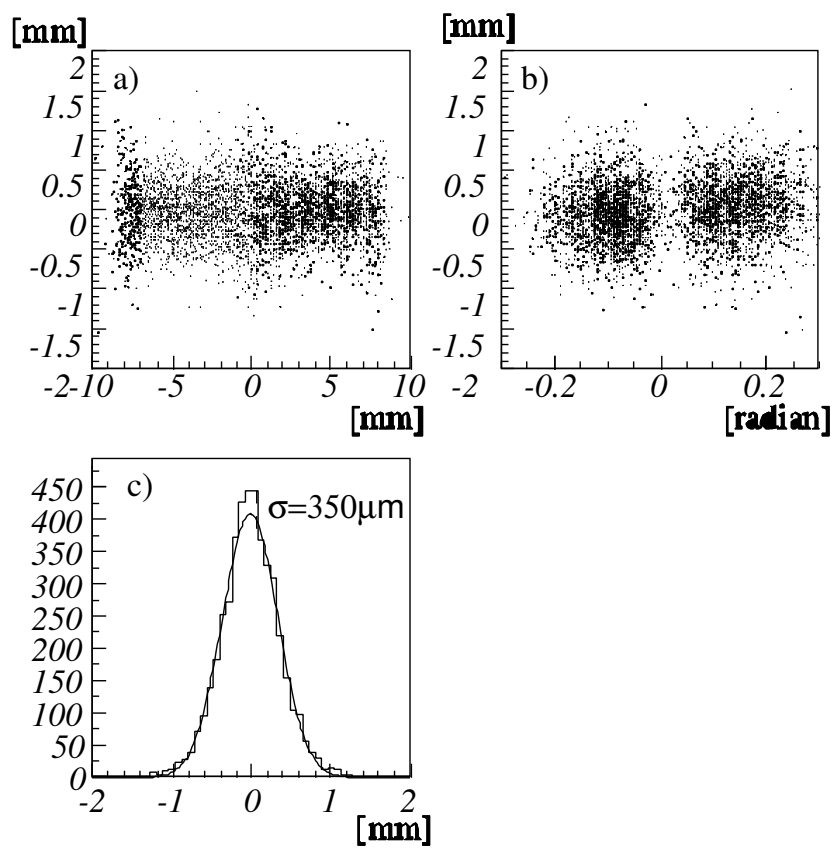


Figure 3.3: The residuals in CDC as a function of the drift time in (a) and of the incident angle in (b). The panel (c) shows the overall resolution.

the beam times. The alignment of BDC with respect to CDC was also surveyed and refined using the data taken without magnetic field.

In the alignment procedure, the BDC hit positions were compared with the straight tracks obtained with CDC hits. Hit positions in BDC were determined using all the X-X'-U-V combination in BDC, and the difference of the BDC hit positions from the extrapolated CDC tracks, here we call it “residual”, was systematically analyzed to determine all the six parameters of three dimensional translations and rotations of BDC (see Appendix A in Ref. [42]). The active area of BDC was divided into 30 regions, to provide the residual distributions as a function of the angle in the x - y plane and the height (z coordinate). Translate and rotation matrices were determined to minimize the systematic shifts in the residual distributions as typically shown in Fig. 3.4. The obtained parameters, the differences from the nominal positions, are summarized in Table 3.3.

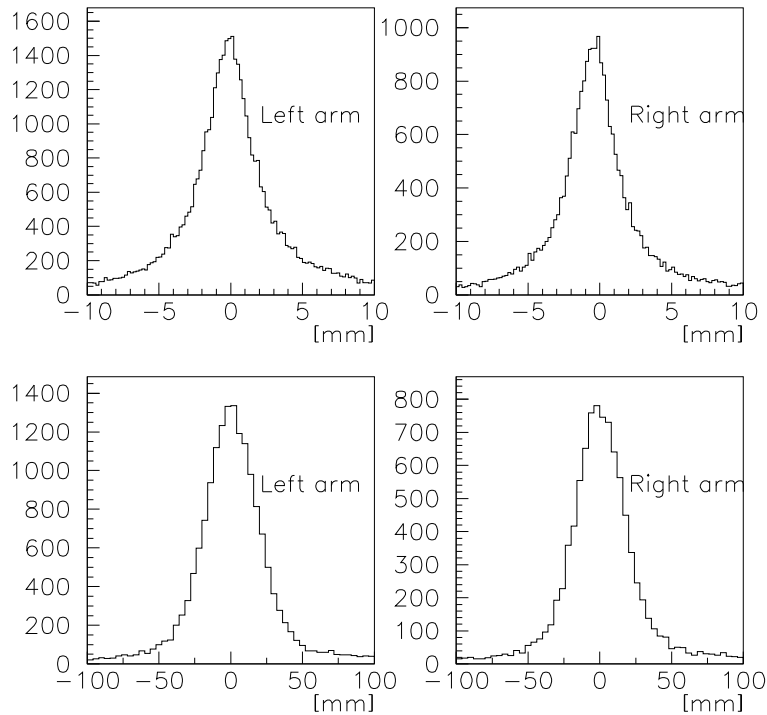


Figure 3.4: The residual distributions between BDC hit positions and CDC extrapolated tracks. The upper figures show the residuals in the radial direction and the lowers are in the vertical direction.

2001 (a)			
arm	dx [mm]	dy [mm]	dz [mm]
left	$+2.40 \pm 0.90$	-0.85 ± 0.65	$+2.54 \pm 0.33$
right	$+2.35 \pm 0.99$	$+0.47 \pm 0.70$	-0.35 ± 0.44
	τ_x [m rad]	τ_y [m rad]	τ_z [m rad]
left	-0.33 ± 0.55	$+1.59 \pm 0.59$	$+2.30 \pm 0.39$
right	-0.19 ± 0.58	$+0.02 \pm 0.61$	-1.69 ± 0.37
2001 (b)			
arm	dx [mm]	dy [mm]	dz [mm]
left	$+2.30 \pm 0.92$	-0.62 ± 0.67	$+2.15 \pm 0.14$
right	$+1.94 \pm 0.79$	$+0.47 \pm 0.58$	-1.06 ± 0.13
	τ_x [m rad]	τ_y [m rad]	τ_z [m rad]
left	-0.13 ± 0.37	$+1.32 \pm 0.35$	$+2.12 \pm 0.29$
right	-0.24 ± 0.16	-0.22 ± 0.17	-1.49 ± 0.25
2002			
arm	dx [mm]	dy [mm]	dz [mm]
left	$+2.44 \pm 0.54$	-1.11 ± 0.42	$+2.60 \pm 0.15$
right	$+2.20 \pm 0.73$	-0.05 ± 0.52	-0.39 ± 0.21
	τ_x [m rad]	τ_y [m rad]	τ_z [m rad]
left	-0.20 ± 0.43	$+1.42 \pm 0.37$	$+1.08 \pm 0.20$
right	-0.38 ± 0.46	-0.24 ± 0.45	-2.79 ± 0.24

Table 3.3: The translation and rotation parameters of BDC with respect to the nominal position. There are two sets of the parameters for the 2001 data because of the earthquake occurred during the data taking period. To obtain the BDC position, BDC should be translated by (dx, dy, dz) first, then rotated by (τ_x, τ_y, τ_z) around the three axes which cross the origin of the global coordinate.

3.2.3 Gain calibration of lead glass calorimeter

Lead glass calorimeters were calibrated using the electron data sample. Since energy deposit of a electron in a calorimeter is proportional to its momenta, we adjusted the gain of each segment as the energy deposit divided by the track momentum (E/p) became unity.

After the track reconstruction, segments of the calorimeters were associated to a track. Since the energy deposit on the calorimeter can spread over a few segments, the pulse heights in the associated segments were summed up if the distance between the segment center and the track was within ± 2.2 , 2.0 and 2.5 times the counter width for RLG, SLG and FLG, respectively. The matching between the track and the associated hit in the electron identification counters as shown later in Sec. 3.3.4 (Fig. 3.18). We iteratively calibrated E/p to be unity, where E is the energy sum of the associated segments. For SLG and FLG, the pulse heights of top and bottom PMTs were also summed up since Čerenkov photons were transported vertically to the both ends of the segment by the total reflection. Event by event, the gain of a PMT was adjusted when its pulse height was larger than the other side. This procedure, which was continued until the gain got stabilized, ensure the gain balance between each segment and also top and bottom PMTs.

Figure 3.5 shows a scatter plot of the E versus p of pure electron samples which is explained in Sec. 3.3.4. The peak values of E/p for all the PMT in the calorimeter segments are plotted in Fig. 3.6, showing that the gain was adjusted within 4% accuracy.

3.3 Event reconstruction

3.3.1 Track reconstruction

The track reconstruction was done in two stages.

At the first stage, the probable combinations of the chamber hits in CDC and BDC were selected separately. Fitting in CDC on the bending plane was approximated with a quadratic function, which was extrapolated to BDC to find probable associations. At this stage, events which had e^+ or e^- candidates in both arms were kept and other events were discarded.

At the second stage, we refined all the track candidates, even though they share same hits, by fitting them with the Runge-Kutta method, and we selected good tracks according to the fit quality.

The second stage required about 10 times as long CPU time as the first stage for an event. The total consumed CPU hours in the track reconstruction was about 10^5 cpu-hours with a 3.06 GHz Xeon CPU. We could do this owing to the CPU power in RIKEN/CCJ and RIKEN Super Combined cluster, where 256 Xeon CPUs were available.

The details of the track reconstruction are described in the following sections.

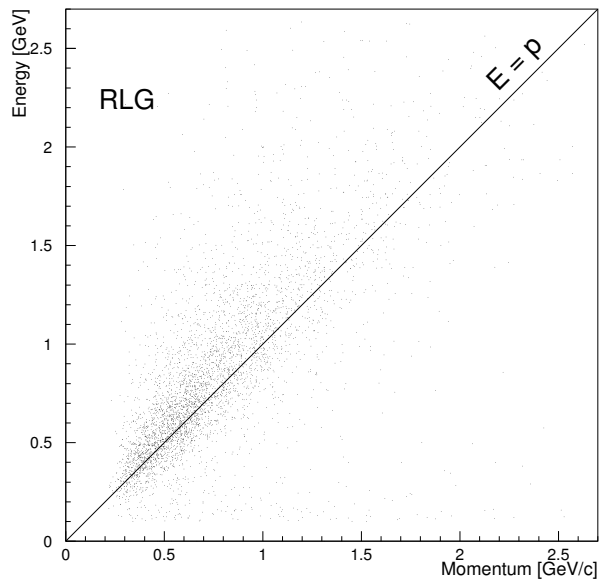


Figure 3.5: The correlation between the RLG energy and the track momentum for the pure electron sample which is explained in Sec. 3.3.4.

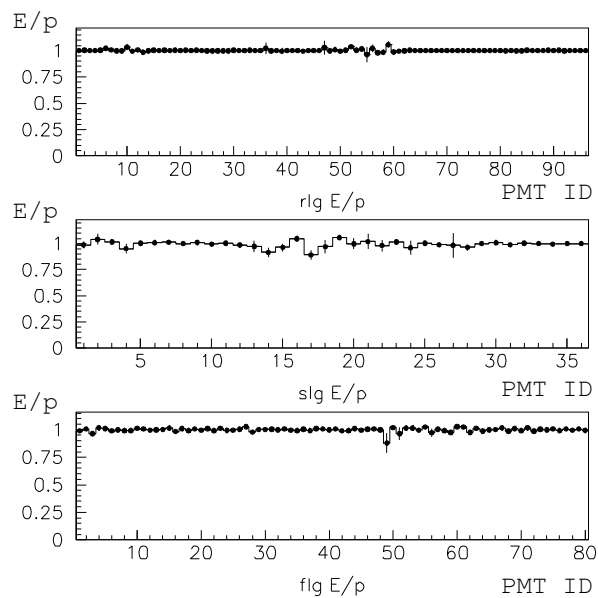


Figure 3.6: The E/p ratios of all the PMTs of the segments of RLG, SLG, and FLG. The ID is numbered from top to bottom PMT, from forward to backward, and from left to right arm. The error bars only show the statistical errors.

First stage: track finding in CDC and BDC

As described in Sec. 2.5.1, CDC had ten layers of drift cells which were grouped into three super layers. Track candidates were first searched using the X and X' layers. Since we cannot determine whether the drift direction is left or right without track fitting, both hits were treated as two independent hits. To reduce CPU time for the track finding, a hit combination in the X and X' layers was regarded as a hit pair with the position at the center of the two hits. A hit without an associated hit in the adjacent layer was also kept as a hit pair candidate.

All the possible combinations of three hit pair candidates over the three super layers were regarded as track candidates if the following conditions were satisfied.

- (A) Since the magnetic field was almost vertical and constant at the location of CDC, a trajectory of a charged particle was approximately a circle in the x - y (horizontal) plane and a straight line in the r - z (vertical) plane. The circle which passes over the three hit combination gives the simple track momentum on the x - y plane. This momentum should be greater than $0.16 \text{ GeV}/c$.
- (B) The circle should cross the target region within a distance of 50 mm from either one of the targets.
- (C) Each three super layer should have at least one hit in X or X' layer, and the total number of CDC hits in the X and X' layers should be greater than three.

Then, the hits of X-X' layers were examined by the fitting with the quadratic function whether the reduced χ^2 of the fit was less than 5.5 and the residual in each layer was smaller than six standard deviations or not.

Next, associated hits in the tilt layers were searched for each track candidate. Since there was a pair of the V-V' layers in the middle super layer, hit pairs were made similarly to the X-X' layers. The search region of hit points in the tilt layers was limited within the five drift cells adjacent to the hit positions in X-X' layers. This region were determined by the tilt angle of 0.11 rad. We required that the assigned hits in the tilt layers was greater than two.

Now the track candidates were fit with a quadratic function in the horizontal plane and a straight line in the vertical plane, and kept as the candidates as far as the residuals of all the hits were within three standard deviations. Each super layers was required to have at least two hits.

Track candidates in BDC were searched independently. At least three hits out of four in the BDC layers (X, X', U, V) were required to form a track segment in BDC. The combination of X and X' was only made if they were apart less than a quarter of the cell size, otherwise they were treated as two independent hits. Associated U and V hits were required to be in the neighboring nine cells from the hit position of the X-X' planes, which was determined by the tilt angle of 0.11 rad. To associate two hits from U and V layers in a track segment, we required the vertical distance between

X-X'-U and X-X'-V combinations to be less than 290 mm. Otherwise, we made two track segments as X-X'-U and X-X'-V.

Then the CDC track was extrapolated to BDC in order to form a CDC-BDC track candidate, where the horizontal position matching within ± 4.3 mm was required to the hits in the X and X' layers in BDC, and the vertical position matching within ± 60 mm was required to the hits in the U and V layers in BDC.

Next, we required the loose track matching with the electron identification counters requiring a matching window of ± 2 counter size. The ADC sum within the matching window were required for the gas Čerenkov counters to have enough pulse height just above the noise level (16 channel for FGC and 7 channel for RGC), and for the calorimeters to have energy deposit above 100 MeV. Each event was required to contain e^+ or e^- candidate in both arms.

Second stage: refining of the hit selection with Runge-Kutta method

In the second stage, the CDC-BDC tracks, which survived in the first stage, were fit with the Runge-Kutta method to determine the refined momentum and the precise trajectory. The particle trajectories were traced in a 50 mm step through the magnetic field map described in Sec. 2.4. Around the layers of the drift chambers the trajectories were traced in a 1 mm step to give the precise hit position. The Runge-Kutta track tracing started from the surface of a virtual cylinder with a diameter of 100 mm located at the center of the magnet. The initial starting point and the initial momentum vector for the minimization were given by the track candidate obtained at the first stage. In each trace of the Runge-Kutta method, a reduced χ^2 was calculated along all the associated hits. The χ^2 value was minimized with a help of the minimization code MINUIT [43].

At this stage the Runge-Kutta fitting was applied for all the possible combination of CDC and BDC track candidates. The CDC-BDC combination which gave the best χ^2 value was selected as the final track candidate among the combinations which shared same hits.

3.3.2 Mass scale and resolution

To evaluate the performance of the spectrometer and the track reconstruction the invariant mass distributions were examined for the observed peaks of $\Lambda \rightarrow p\pi^-$ and $K_S^0 \rightarrow \pi^+\pi^-$ decays as shown in Fig. 3.7.

The observed peak widths and centroids of the resonances were compared with the expected mass shape by a detailed detector simulation using GEANT4 toolkit [44]. The momentum distributions of Λ and K_S^0 were taken from the data. The effects on the invariant mass spectra caused by multiple scatterings and energy losses of particles, the tracking performance with the chamber resolution were taken into account. The expected peak position and resolution of K_S^0 are 496.9 MeV/ c^2 and 3.4 MeV/ c^2 , whereas the obtained peak position was 496.8 ± 0.2 MeV/ c^2 with the Gaussian σ of $3.9 \pm$

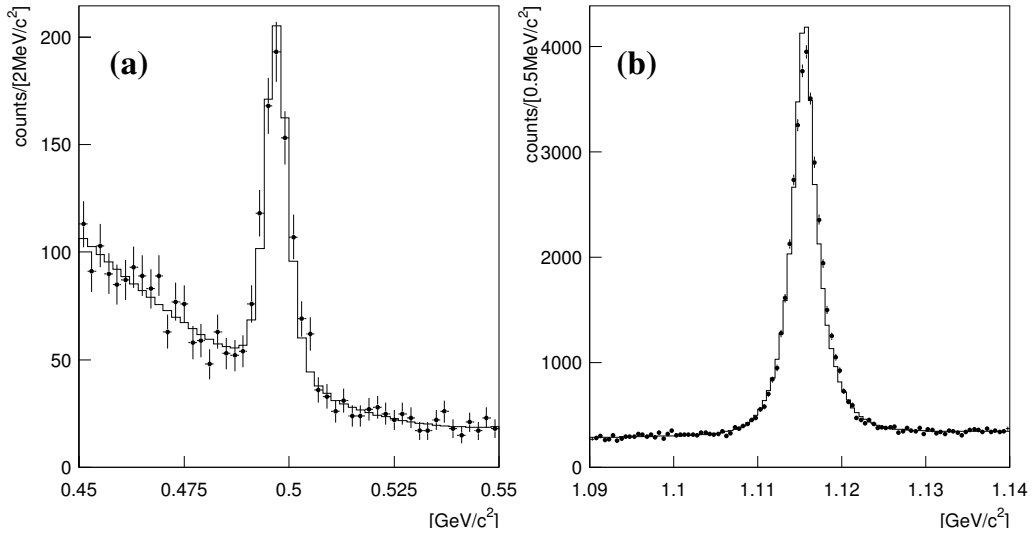


Figure 3.7: (a) Invariant mass spectrum of $\pi^+\pi^-$. The histogram is the fit result, which is a sum of the simulated shape over a quadratic background. (b) Invariant mass spectrum of $p\pi^-$. The histogram is the fit result, which is a sum of the simulated resonance shape over a linear background.

$0.4 \text{ MeV}/c^2$. They are quite consistent with each other. As for Λ , although the spectral shape of both the data and the simulation can not be described with a Gaussian, the observed spectra were fit with the simulated shape to examine the consistency. The simulated spectrum reproduces the data almost perfectly as shown in Fig. 3.7(b).

Mass Scale and Resolution for $\phi \rightarrow e^+e^-$ decays

In the case of the analyses for $\Lambda \rightarrow p\pi^-$ and $K_S^0 \rightarrow \pi^+\pi^-$, a misalignment of the tracking devices was not so important. In our acceptance, the daughter particles from the both decay channels had a small opening angle and were detected in the same arm of our spectrometer. Thus the mass distributions of the mother particles, especially their absolute scale, were insensitive to small misalignments of the tracking devices. In $\phi \rightarrow e^+e^-$ decays, the daughter particles, electron and positron, have a large opening angle and we analyzed only the events when we detected an electron and a positron in the different arms. In such a case, the effect from the misalignment cannot be neglected. As discussed in Sec. 2.4, the uncertainty of the magnetic field strength is an order of 0.3% corresponding to $3 \text{ MeV}/c^2$ of the mass scale uncertainty around the ϕ meson mass. The BDC alignment errors shown in Table 3.3 correspond typically to $2 \text{ MeV}/c^2$ of the mass scale uncertainty and $2 \text{ MeV}/c^2$ of an additional mass resolution source, as lately discussed in this section. This means our calibrations and alignment were not precise enough to the level of $3 \text{ MeV}/c^2$. Below we show how we determined the corrections on the mass scale and the additional smearing on the mass resolution

from the data.

We selected the region of $\beta\gamma_\phi > 1.5$ in both the simulation and the data to avoid a possible effect from the in-medium mass modification. We fitted the data with the simulated mass shape of the ϕ meson with varying the mass offset and the mass resolution of the ϕ meson in the simulation. The change of the mass resolution was done by convoluting additional Gaussian to the mass shape. Figure 3.8 and 3.9 show the obtained χ^2 values as functions of the mass offset and the mass resolution. In the determination of the mass offset, we fitted the LR and RL event data separately because the BDC misalignment could cause an opposite-sign offset in each. Here 'LR event' means the event containing e^+ in the left arm and e^- in the right arm of the spectrometer, and 'RL event' means vice versa. For the study of additional smearing on the mass resolution, we fitted the mass distributions for all the data together because the statistics was not enough to determine meaningful mass resolution in each distribution. The best fit values and errors are listed in Table 3.4. The systematic errors were estimated by changing the fit region, the binning size and the background shape (quadratic or cubic curve). The additional smearing on the mass resolution was obtained to be $3.6 \pm 1.3 \text{ MeV}/c^2$, with which the simulated mass resolution of $10.1 \text{ MeV}/c^2$ get worse, but only to $10.7 \text{ MeV}/c^2$.

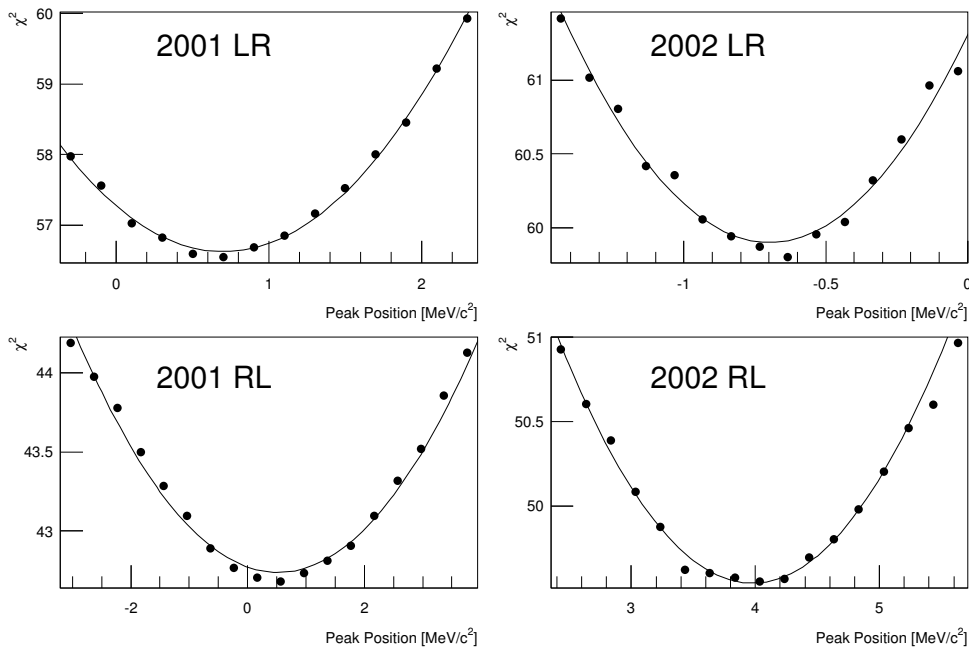


Figure 3.8: The obtained χ^2 values as functions of the mass offset added to the simulation shape. The bold circles represent the obtained χ^2 and the lines represents the fit results with a quadratic curve. The four panels are for the different data sets (see text).

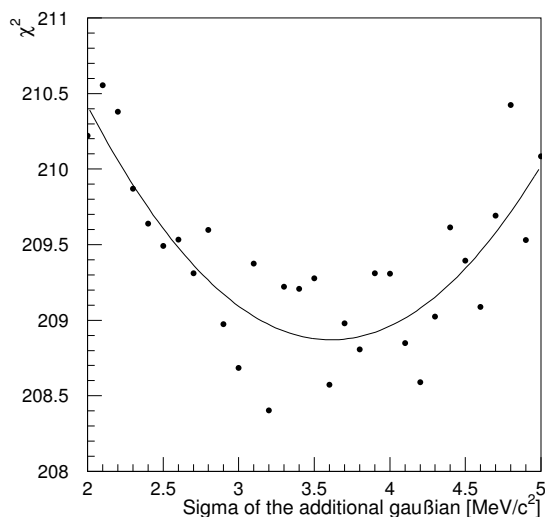


Figure 3.9: The χ^2 values as a function of additional smearing on the mass resolution. The circles represent the obtained χ^2 and the line represents the fit result with a quadratic curve.

	2001		2002	
	$Offset_{LR}$	$Offset_{RL}$	$Offset_{LR}$	$Offset_{RL}$
peak position difference [MeV/ c^2]	$0.7 \pm 0.9^{+0.0}_{-0.6}$	$0.6 \pm 2.8^{+0.5}_{-0.7}$	$-0.7 \pm 0.6^{+0.0}_{-0.4}$	$4.2 \pm 1.3^{+0.1}_{-0.2}$
additional Gaussian width [MeV/ c^2]	$3.6 \pm 1.3^{+1.2}_{-0.0}$			

Table 3.4: The best fit values of the mass offset and the mass resolution to be used to modify the simulated mass shape. Error values are statistical (first) and systematic (second). The systematic errors are evaluated by changing the fit region, the bin width and the background shape in the fit (quadratic or cubic curve).

It is worth mention that in the first order approximations the BDC misalignment effects oppositely in the mass offsets in the LR and RL events. Thus we consider that the average of the offsets attributes to the magnetic field uncertainty and the difference to the BDC alignment. The averaged mass offset was $0.7 \pm 1.5 \text{ MeV}/c^2$ and $1.8 \pm 0.7 \text{ MeV}/c^2$ for the year 2001 and 2002, respectively. These values are within the uncertainty of the magnetic field map, 0.3%, as described in Sec. 2.4. Please note that the magnetic field is different between the year 2001 and 2002 as described in Sec. 2.4.

We examined how the mass offset difference between the LR and RL events “ $Offset_{LR} - Offset_{RL}$ ” and the mass resolution changed according to the BDC misalignment, with use of the simulation. Approximately, BDC rotation around the z axis (vertical direction) changes “ $Offset_{LR} - Offset_{RL}$ ” and other rotations and translations deteriorate the mass resolution. The left panel in Fig. 3.10 shows the effect of the BDC rotation around the z axis on the “ $Offset_{LR} - Offset_{RL}$ ”. The left-arm BDC was artificially rotated anticlockwise around the z axis, while the right-arm BDC was rotated in the opposite direction with the same angle. The right panel in Fig. 3.10 shows the effect on the mass resolution with the BDC translation (right arm only) along the x axis. It can be concluded that the offsets and the resolution given in Table. 3.4 are understandable almost within $1 \sim 2\sigma$ of the accuracy of the BDC alignment described in Section 3.2.2.

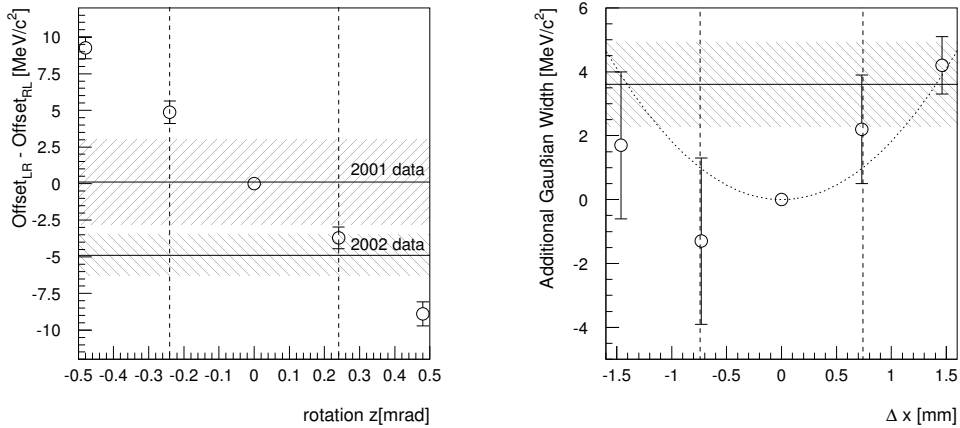


Figure 3.10: The left panel shows the effect of the rotation around z axis on the peak position difference “ $Offset_{LR} - Offset_{RL}$ ”. The right panel shows the effect of the translation along x axis on the mass resolution. The horizontal solid lines represent the results of the best fits with the hatched bands as the statistical errors. The vertical dotted lines show the uncertainty (1σ) of the BDC alignment.

We modified the simulated mass shape according to the values in Table 3.4, and used the modified one in the data fits presented in Sec. 4.3. The systematic errors in Table 3.4 were used to estimate the systematic errors for the amount of the excess in

Sec. 4.4.1.

3.3.3 Vertex reconstruction

The vertex point of an event was determined by minimizing S , the weighted quadratic sum of the distances from the vertex to each track, which is defined as follows;

$$(3.1) \quad S = \frac{1}{3N_t - 4} \sum_{j=1}^{N_t} \left(\left(\frac{d_x^j}{\sigma_x} \right)^2 + \left(\frac{d_y^j}{\sigma_y} \right)^2 + \left(\frac{d_z^j}{\sigma_z} \right)^2 \right),$$

where N_t is the number of tracks in an event, $\mathbf{d}^j = (d_x^j, d_y^j, d_z^j)$ is the distance vector between the vertex point and the j -th track, and σ_i represents the error of the vertex determination in each axis. The factor σ_i were determined as $\sigma_x = 1.44$ mm, $\sigma_y = 1.80$ mm, and $\sigma_z = 7.15$ mm. First, the vertex points were obtained by MINUIT as the point where S became the minimum with all tracks. After the fitting process was converged, tracks with the condition $((d_x^j/\sigma_x)^2 + (d_y^j/\sigma_y)^2 + (d_z^j/\sigma_z)^2) > 10$ were discarded as they were considered not from the vertex point. If some tracks were discarded, the fitting process was repeated with the remaining tracks. If only one track remained, this event was considered not to have a proper vertex point. When S for the final vertex was larger than 5, the event was also discarded. The reconstructed vertex points were required to be within 3.5 standard deviations from either of the target centers.

The reconstructed vertex distribution for the 2002 data is shown in Fig. 3.11. The five targets are clearly seen. The obtained target positions and the vertex resolutions are listed in Tables 3.5. In order to identify an interaction target i , we defined $\chi_{T_i}^2$ for the i -th target as

$$(3.2) \quad \chi_{T_i}^2 = \sum_{j=x,y,z} \left(\frac{(d_j - c_{ij})}{\sigma_{ij}} \right)^2,$$

where $\mathbf{d} = (d_x, d_y, d_z)$ is the reconstructed vertex position, \mathbf{c}_i is the crossing point between the beam and target i , and $\boldsymbol{\sigma}_i = (\sigma_{ix}, \sigma_{iy}, \sigma_{iz})$ is the vertex resolution around target i as listed in Table 3.5. The interaction target disk was identified to be the one with which $\chi_{T_i}^2$ was the minimum.

Once the interaction target was determined, we repeated the Runge-Kutta fit procedure by requiring that e^+ and e^- tracks were originated from the same point on the interaction target. This procedure improved the mass resolution by a factor of 1.5. The x positions of the targets were fixed to the measured values shown in Table 3.5. In this fit, we minimized χ_C^2 , the squared sum of the residuals, the hit positions to the tracks and the vertex point to the nominal beam position. The χ_C^2 can be expressed as

$$(3.3) \quad \chi_C^2 = \sum_{s=\pm 1} \sum_l \left(\frac{(h_l^s - e_l^s)}{\sigma_l} \right)^2 + \sum_{j=y,z} \left(\frac{(v_j - c_j)}{\sigma'_j} \right)^2,$$

here h_l^s and e_l^s are the hit position and the track position, respectively, with a charge s on the drift chamber layer l ; σ_l is the position resolution of layer l ; \mathbf{v} is the vertex

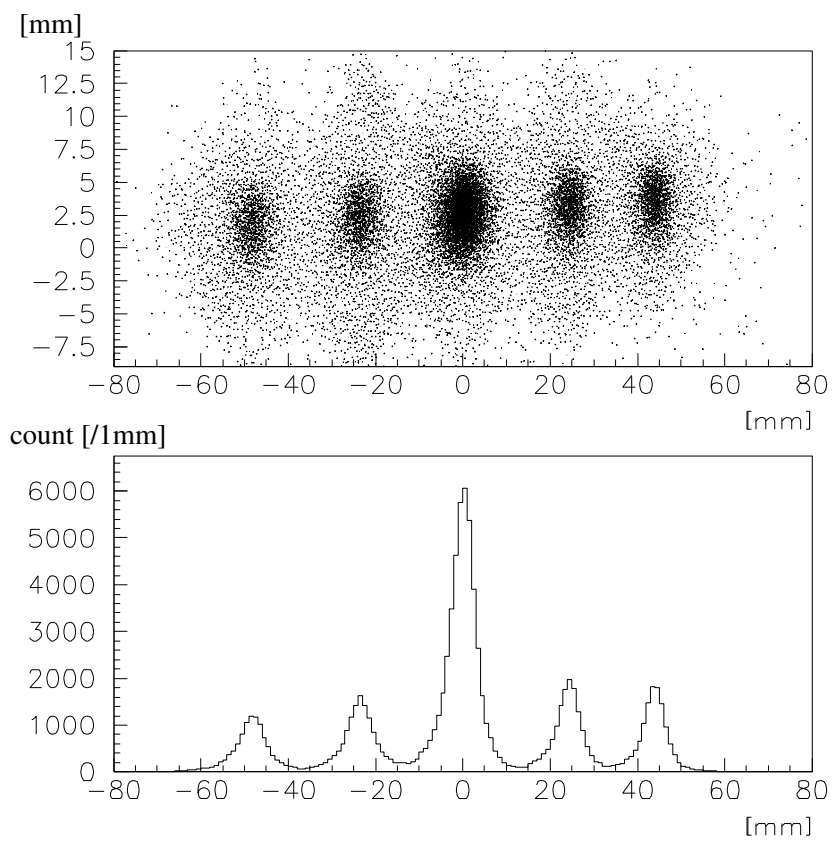


Figure 3.11: Vertex distribution in the $x-y$ plane (upper) and the projection in the x axis (lower) of the 2002 data.

point on the interaction target; and \mathbf{c} is the beam center position on the interaction target. Although we measured only the beam size σ'_y as described in Sec. 2.3, we set both σ'_y and σ'_z at 1.59 mm for the year 2001 and 0.83 mm for the year 2002 assuming that σ'_z was the same as σ'_y .¹

After the fit was converged, we selected events whose χ^2_C/ndf shown in Fig. 3.12 was smaller than 5, where ndf is the number of degrees of freedom. The number of parameter is eight, i.e., y and z coordinates of the vertex point on the target and the momentum vector (p_x^s, p_y^s, p_z^s) for each track at the vertex. The typical number of hits in a track was 26 (maximum is 28).

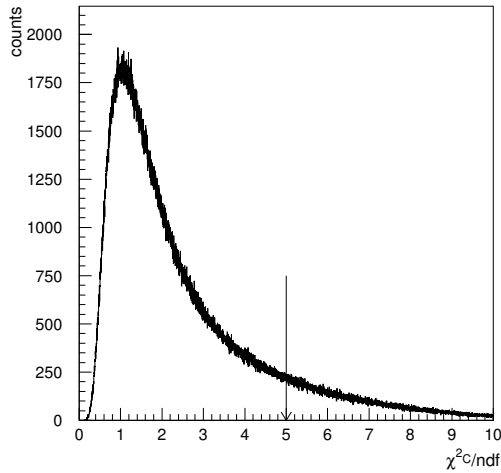


Figure 3.12: The distribution of χ^2_C/ndf . The region below the arrow was used for the final sample.

3.3.4 Electron identification

The electron identification was performed with two or three stages of iso-butane-filled gas-Čerenkov counters or lead-glass EM calorimeters in the momentum range up to 2.7 GeV/c. The upper limit in the momentum range was set to avoid pion contamination above the gas Čerenkov threshold. The observed momentum distributions of electrons and positrons are shown in Fig. 3.13 and Fig. 3.14. Figure 3.14 was obtained by dividing the data into three regions by $\beta\gamma$ of the reconstructed e^+e^- pairs.

¹On the beam tuning prior to the beam time, we tuned the beam profile on the luminescence board to be a circle.

Table 3.5: The mean values of target positions (x, y, z) and the precisions of the vertex determination ($\sigma_x, \sigma_y, \sigma_z$) in the year 2001 and 2002.

2001					
target	Cu-1	C	Cu-2		
x	-47.04 [mm]	-0.14 [mm]	45.46 [mm]		
y	3.13	4.03	4.91		
z	0.61	0.62	0.67		
σ_x	3.73	3.48	2.71		
σ_y	3.24	3.74	2.42		
σ_z	3.68	3.70	3.14		

2002					
target	Cu-1	Cu-2	C	Cu-4	Cu-5
x	-48.03 [mm]	-23.41 [mm]	0.17 [mm]	24.60 [mm]	44.21 [mm]
y	0.89	1.31	1.72	2.22	2.57
z	0.55	0.54	0.52	0.54	0.57
σ_x	3.21	3.35	3.20	1.98	2.01
σ_y	1.98	2.27	1.97	2.94	2.61
σ_z	4.33	4.54	3.85	3.98	3.74

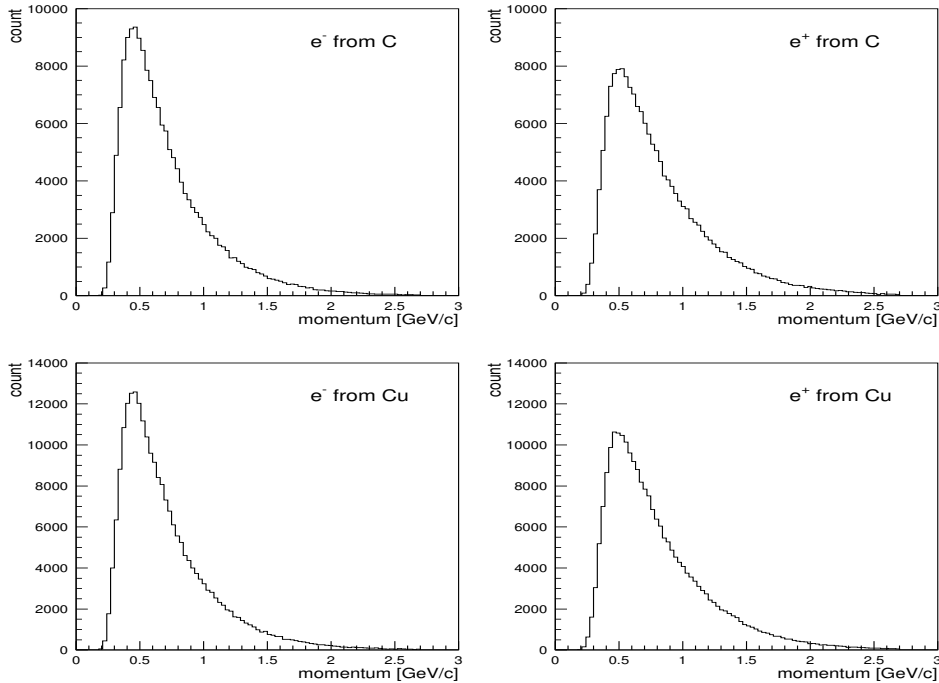


Figure 3.13: The momentum distributions of e^- (left) and e^+ (right) in the final sample. The upper panels are for the C target and the lower panels are for the Cu target.

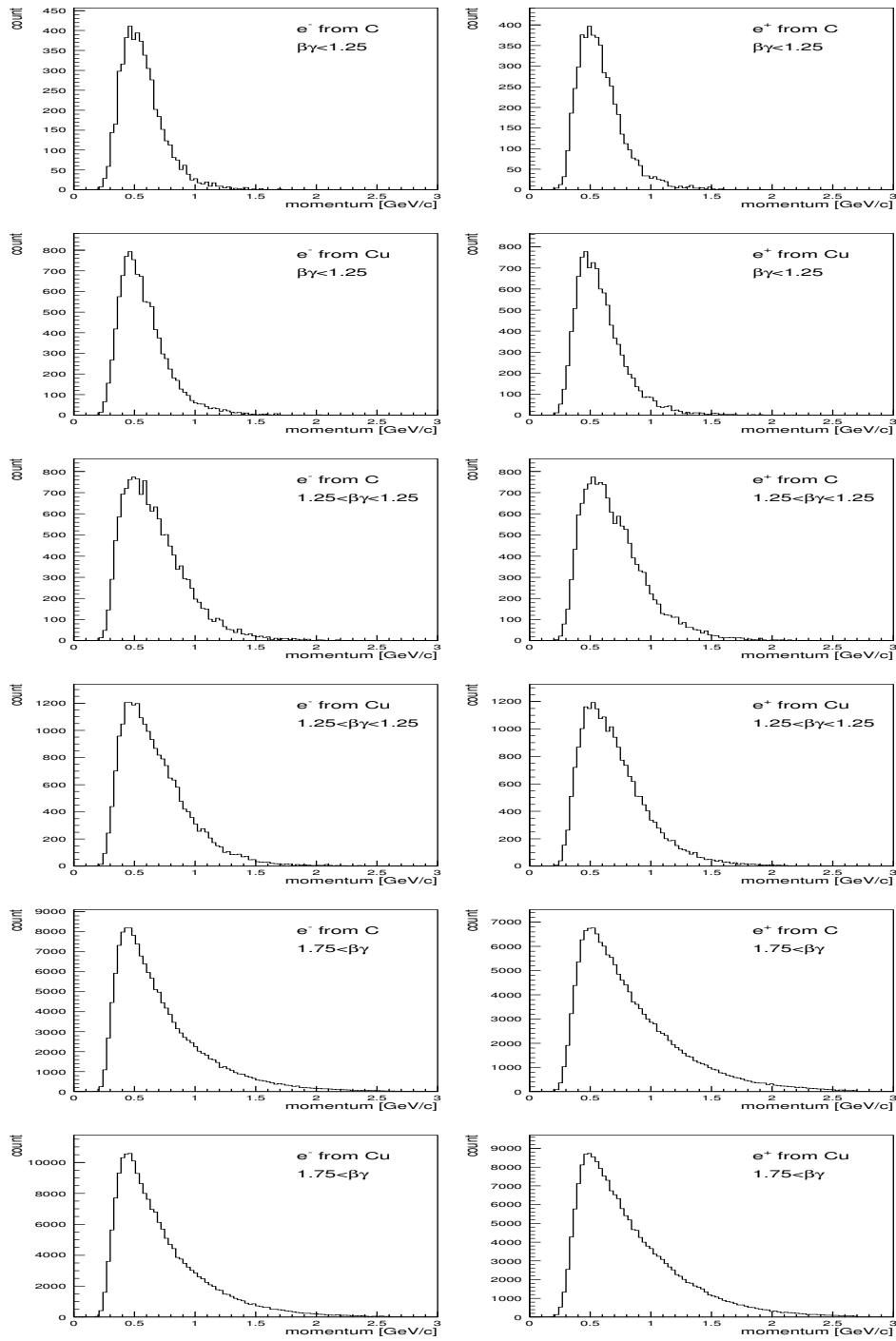


Figure 3.14: The momentum distributions of e^- (left) and e^+ (right) in the final sample divided by $\beta\gamma$ of the reconstructed e^+e^- pairs. The target and the $\beta\gamma$ region are indicated in each panel.

Electron identification with gas Čerenkov counters

The FGC and RGC hit position was defined as a weighted mean over a cluster of segments in which the Runge-Kutta track passed plus the nearest neighbors as a margin. As the weights the ADC sums of the top and the bottom PMTs were used. The horizontal position matching of the FGC and RGC hit positions to the Runge-Kutta tracks are shown in Fig. 3.15. We defined a matching window of the FGC and RGC to be within ± 1.0 segment size. We required an electron candidate to have the ADC sum of the hit cluster exceeding 400 channels in FGC and 100 channels in RGC. The typical ADC spectrum of the cluster is shown in Fig. 3.16. We required the dip angle (vertical direction) of the associated track to be within ± 0.45 rad for FGC and ± 0.15 rad for RGC, based on the vertical acceptance of ± 0.4 rad and ± 0.1 rad for FGC and RGC, respectively.

We also required an electron candidate to have the associate TDC hit in the gas Čerenkov counters. For the TDC measurements, the OR-ed signals of the upper and the lower PMTs were used. The TDC signal of the electron identification counters associated to the tracks made a clear peak as shown in Fig. 3.17.

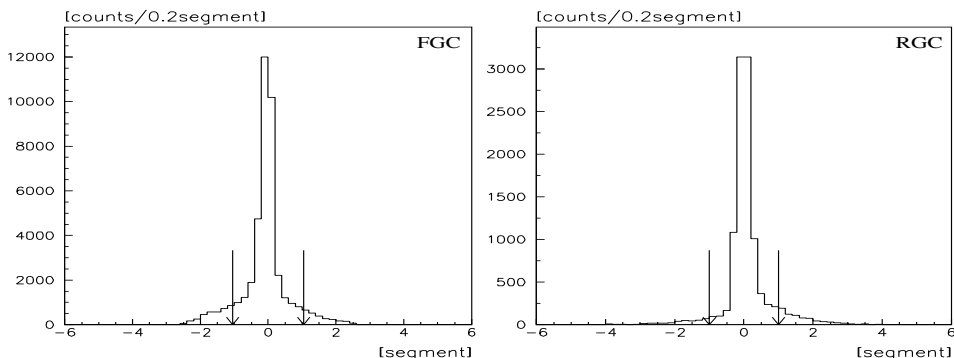


Figure 3.15: Horizontal matching between the electron tracks and the FGC hits at $r = 1200$ mm (left), and the RGC hits at $r = 2105$ mm (right). Electron tracks are selected as described in Sec. 3.3.4. The arrows indicate the region for the electron selection.

Electron identification with lead glass calorimeters

The horizontal position matching of RLG, SLG, and FLG to the Runge-Kutta tracks is shown in Fig. 3.18. We defined a matching window to be within ± 1 counter size for RLG and SLG, and ± 1.5 counter size for FLG. The hit positions were defined as a weighted average with the same manner as the gas Čerenkov counters. The hit was considered to be an electron candidate when the sum of the energies from the horizontally-associated three segments exceeded 0.3 GeV and the summed energy over the momentum (E/p) was greater than 0.6, as shown Fig. 3.19. The limit corresponds

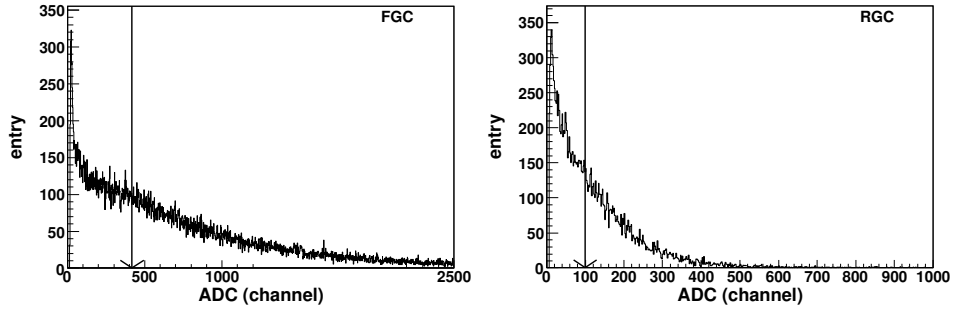


Figure 3.16: A typical ADC sum spectrum of FGC (left) and RGC (right). The arrows indicate the threshold for the electron selection.

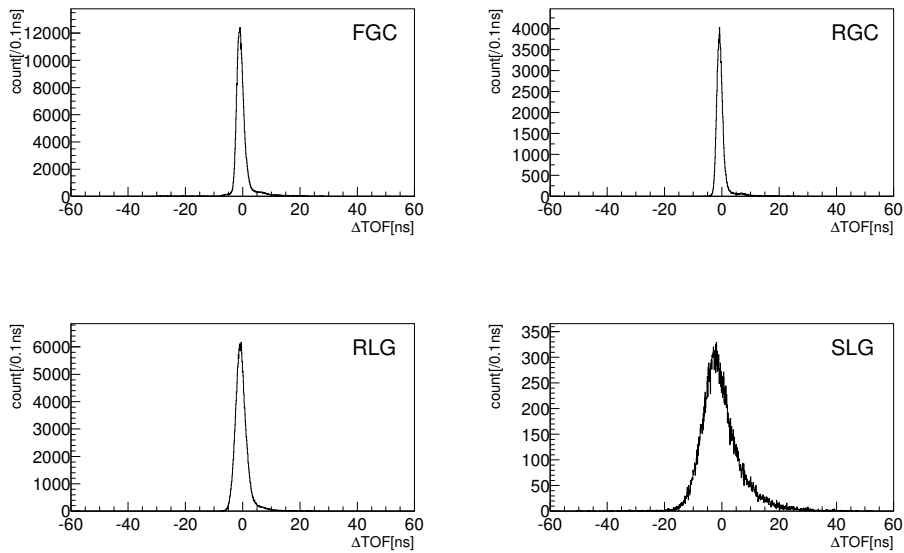


Figure 3.17: Measured TOF distributions of the electron identification counters. The abscissas are $\Delta\text{TOF} = t - t_0$, where t is a measured TOF and t_0 is the expected TOF value for $\beta = 1$ particles.

to two standard deviations of the E/p distribution. Since the vertical acceptance of RLG is $270 \text{ mm} < |z| < 880 \text{ mm}$ from the beam line, we required the vertical position of the track at RLG, at $r = 1730 \text{ mm}$, to be in the range of $\pm 170 \text{ mm}$ to $\pm 980 \text{ mm}$, including 100 mm as a margin. Similarly, the vertical position of the track was required to be in the range of -575 mm to 575 mm for FLG, since the vertical acceptance of FLG is from -475 mm to 475 mm . The dip angle of the track associated to SLG was required to be within $\pm 0.45 \text{ rad}$.

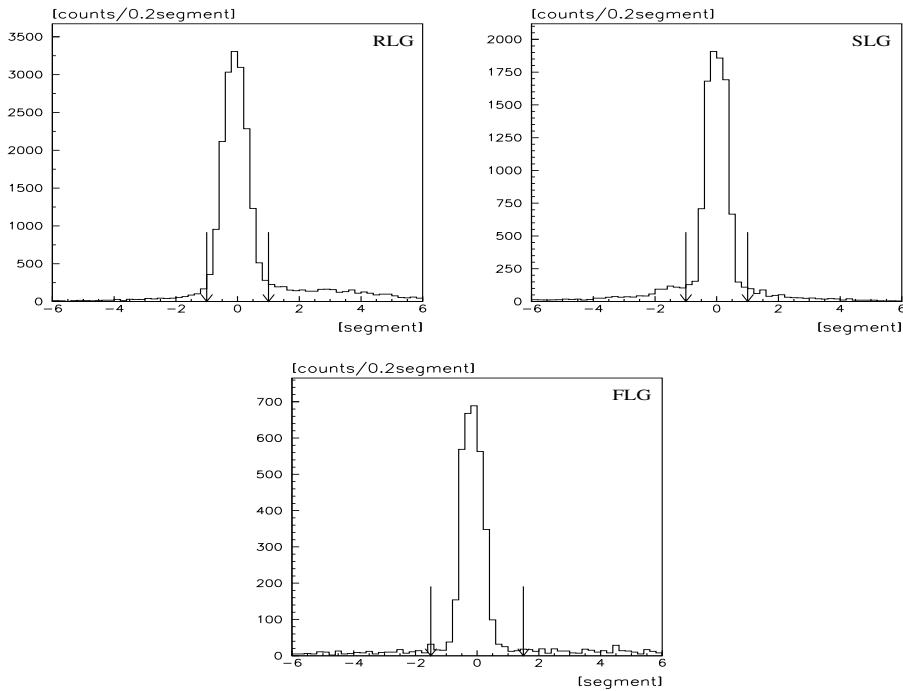


Figure 3.18: Horizontal matching between electron tracks and RLG, SLG, and FLG hits. The arrows indicate the region for the electron selection.

We also required the e^+e^- pairs to have the associated TDC data in the calorimeters except for FLG, since FLG did not participate in the trigger logic and had no TDC information. In Fig. 3.17, the distributions of the TOF values of $\Delta\text{TOF} = t - t_0$ are shown.

Other Cuts for Final e^+e^- Sample

If we could reconstruct more than one e^+e^- pair in a same event, the event is more likely to contain γ -conversions or π^0 Dalitz decays thus such an event was excluded from the final sample. The amount of the eliminated events was 9%.

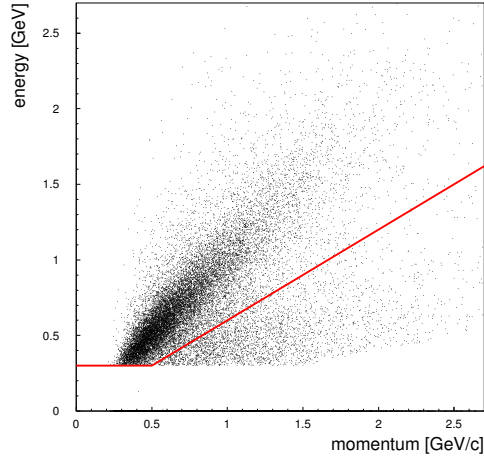


Figure 3.19: The correlation between energy and momentum in RLG. The region above the red solid lines is used for the electron selection.

Efficiency evaluation by the pure electron sample

In order to evaluate the efficiency of the electron identification, we used a pure electron sample from γ conversions and π^0 Dalitz decays. We eliminated the trigger-bias in the selection of the pure electron sample as follows. First, one e^+ track and one e^- track which satisfied the trigger condition were excluded. If there are two or more e^+ or e^- tracks which satisfied the trigger condition in the same event, one of them was randomly excluded as the trigger particle. For the remaining tracks, we required that a dip angle difference between two tracks should be less than 0.01 rad and the invariant mass was less than $0.01 \text{ GeV}/c^2$, to ensure that they were originated from π^0 Dalitz decays or γ conversions. The invariant mass distribution of those unbiased pure electron sample is shown in Fig. 3.20. The clear peak at a zero mass correspond to conversion and Dalitz pair electrons. Using these unbiased electrons, the detection efficiencies were evaluated.

The electron identification efficiencies of the five electron-ID counters, i.e., FGC, RGC, SLG, RLG and FLG, as a function of the momentum are shown in Figs. 3.21. The efficiency curves were fitted with a phenomenological function;

$$(3.4) \quad f = a - b/p^c$$

where a, b, c are the fit parameters, and p is the momentum of electrons. The obtained parameters are listed in Table 3.6. These efficiency functions were applied in the Monte Carlo simulation described in Sec. 4.2.4. The efficiency to identify e^+e^- pairs in the ϕ mass region ($1.00\text{--}1.05 \text{ GeV}/c^2$) was obtained to be 53% for the final sample.

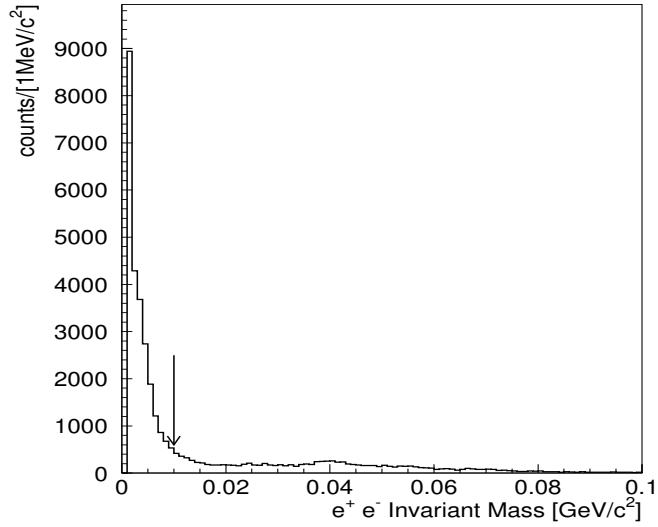


Figure 3.20: Invariant mass spectrum of the selected electron pairs as the pure electron sample (see text). The region below the arrow was used for the pure electron sample for the detector efficiency analyses.

counter	a	b	c
FGC	0.867	0.207	0.76
RGC	0.623	1.8×10^{-6}	9.3
RLG	0.921	9.9×10^{-6}	8.2
SLG	0.882	1.7×10^{-4}	6.8
FLG	0.913	1.2×10^{-6}	10.0

Table 3.6: The parameters of the electron efficiency curves given by Eq. (3.4).

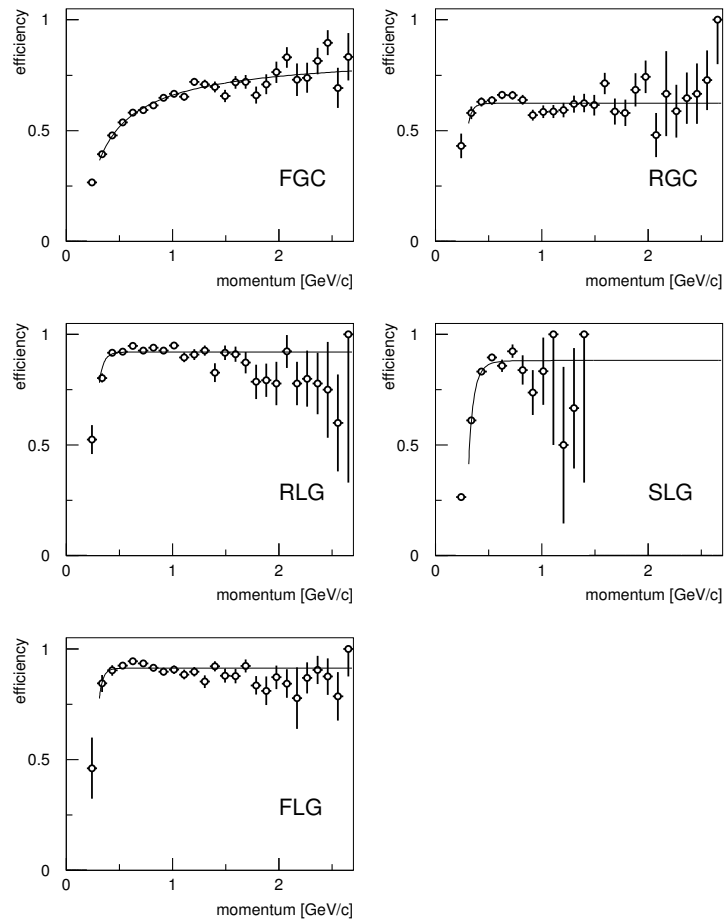


Figure 3.21: The electron identification efficiencies of FGC, RGC, RLG, SLG and FLG as functions of track momenta. Solid curves represent fit results with Eq. (3.4).

3.3.5 Contamination by electron misidentification

There remained a certain amount of $e^\pm\pi^\mp$ pairs in the final e^+e^- data sample, although remaining $\pi^+\pi^-$ pairs were negligible. In order to evaluate such contaminations, we examined the signal to noise ratio S/N of ϕ mesons S and background N in the mass region from 1.0 to 1.05 GeV/c^2 . We fitted the invariant mass spectra with a quadratic curve for the background and a Breit-Wigner curve convoluted with Gaußian for the resonance shape to obtain the number of the signal S and the background N . The contamination component appears only in the N , thus we put $N = e + c$, where e is from uncorrelated e^+e^- pairs and c is from misidentified electrons. Figure 3.22 shows the ratio S/N with different cuts for the electron identification. When the electron selections are tightened enough until the misidentification is negligible, we find that the ratio S/N becomes better and saturates to be S/e . Saturated S/N ($= S/e$) values were found to be 1.39 ± 0.07 and 1.31 ± 0.06 for $p + C$ and $p + \text{Cu}$ reactions, respectively.

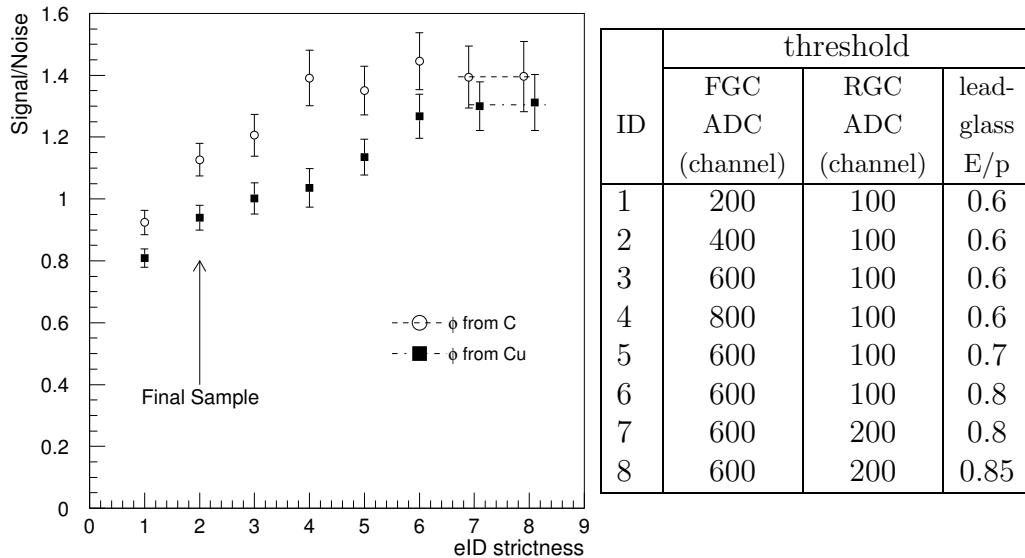


Figure 3.22: The signal to noise ratio S/N of e^+e^- pairs in the mass region from 1.0 to 1.05 GeV/c^2 for various electron identification conditions. The conditions are summarized in the table (right). The larger ID number corresponds to more strict condition. The values are the thresholds applied to the electron identification counters.

The S/N ($= S/(e + c)$) in the final e^+e^- sample (corresponding to ID = 2) were obtained to be 1.13 ± 0.05 and 0.94 ± 0.04 for $p + C$ and $p + \text{Cu}$ reactions, respectively. Since saturated values of S/N are independent of the electron purity, the

$e^\pm\pi^\mp$ contaminations can be obtained as

$$(3.5) \quad c = N - \frac{S}{(S/N)_{\text{saturate}}}.$$

We estimated the amount of the backgrounds due to the particle misidentification as $9.0 \pm 2.5\%$ and $14.4 \pm 2.1\%$, and due to the uncorrelated e^+e^- pairs as $38.0 \pm 2.7\%$ and $37.1 \pm 2.3\%$, for $p + \text{C}$ and $p + \text{Cu}$ reactions, respectively.

Chapter 4

Results and Discussions

In this chapter, we present the e^+e^- invariant mass distributions and compare them with the expected mass shape for the in-vacuum ϕ decays. As a result, an excess is observed over the expected shape. We discuss the theoretical interpretation for the observed difference between the data and the expected mass shape.

4.1 Observed mass spectra of e^+e^- pairs

We reconstructed the invariant mass spectra from the measured three momenta of e^+ and e^- . Figure 4.1 shows the obtained invariant mass distributions in all the mass region and in the ϕ meson mass region. The detector acceptance and the mass scale are not corrected here. We used e^+e^- events in which a positron and an electron were detected in the different arms only. The suppression in the low-mass region is due to the detector acceptance and above event selection. The spectra for carbon contain both 2001 and 2002 data and the spectra for copper contain the two copper targets in 2001 and the four in 2002.

4.2 Expected mass shape for in-vacuum decay of ϕ mesons

In the present work, determination of the resonance shape of the ϕ meson is very important. In the following sections we describe physical processes and experimental effects which affect on the in-vacuum shape of $\phi \rightarrow e^+e^-$ in the present experiment.

4.2.1 Resonance shape of $\phi \rightarrow e^+e^-$ decay

For the ϕ meson resonance shape, we used the non-relativistic Breit-Wigner curve

$$(4.1) \quad M_\phi(m) \propto \frac{1}{(m - m_\phi)^2 + (\Gamma_\phi^{tot}/2)^2}$$

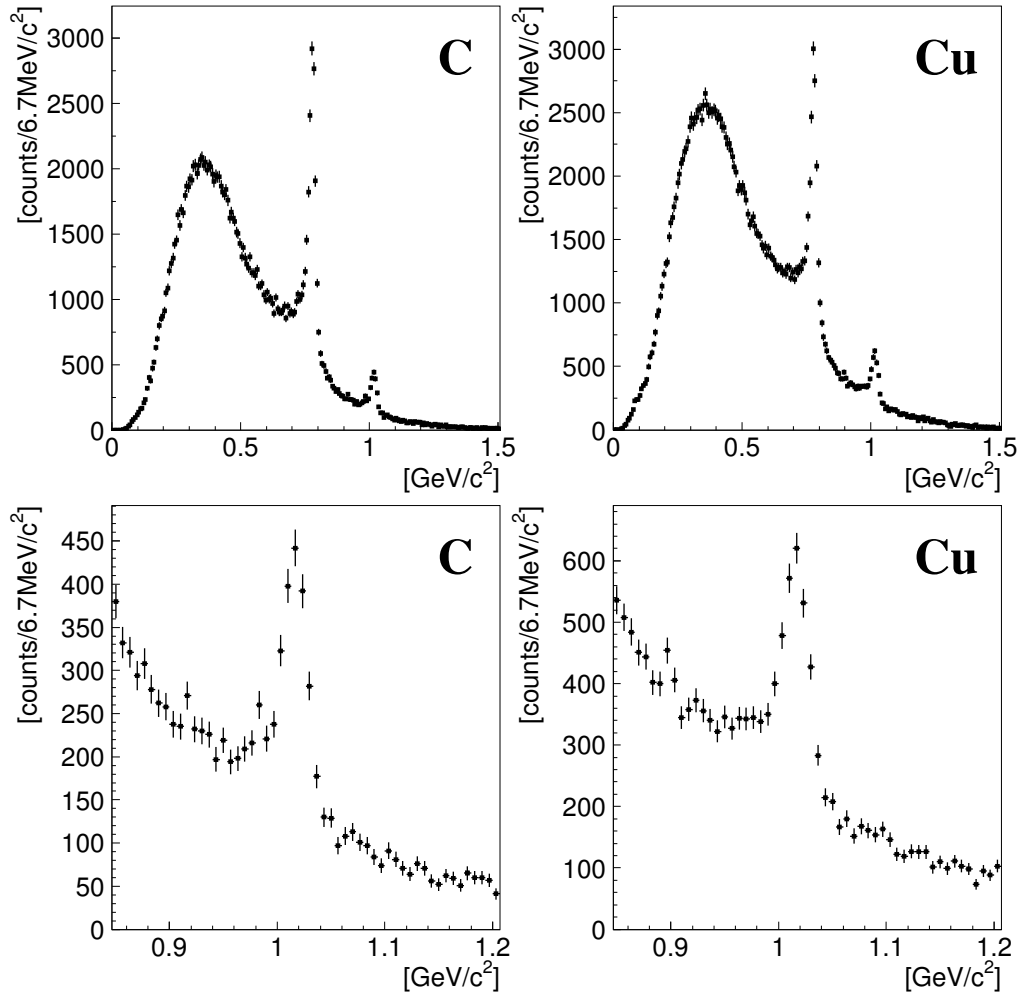


Figure 4.1: Obtained e^+e^- invariant mass distributions for the carbon (left) and the copper (right) targets. The upper panels are for all the e^+e^- pairs, and the lower panels are the zoom up views for the ϕ meson mass region (0.85 - 1.2 GeV/c^2).

with natural mass ($m_\phi = 1019.456 \text{ MeV}/c^2$) and total decay width ($\Gamma_\phi^{tot} = 4.26 \text{ MeV}/c^2$). The difference between non-relativistic Breit-Wigner curve (4.1) and relativistic Breit-Wigner curve for the $\phi \rightarrow e^+e^-$ decay is very small and can be characterized as a pole mass shift of $0.2 \text{ MeV}/c^2$, as shown in Figure 4.2. This difference is considered as a systematic uncertainty on the shapes as described later in Section 4.4.1. Here, the relativistic Breit-Wigner curve for $\phi \rightarrow e^+e^-$ decay is expressed as:

$$(4.2) \quad M_\phi(m) \propto \frac{mm_\phi\Gamma_\phi^{ee}(m)}{(m^2 - m_\phi^2)^2 + m_\phi^2\Gamma_\phi^{tot}(m)^2},$$

where $\Gamma_\phi^{ee}(m)$ and $\Gamma_\phi^{tot}(m)$ are the momentum dependent partial and total widths. $\Gamma_\phi^{tot}(m)$ is defined by

$$\Gamma_\phi^{tot}(m) = \Gamma_\phi^{tot} \cdot (m_\phi/m) \cdot (k^{tot}(m)/k_\phi^{tot})^3,$$

where $k^{tot}(m) = \sqrt{m^2/4 - m_K^2}$ and $k_\phi^{tot} = \sqrt{m_\phi^2/4 - m_K^2}$ are phase space factors, with $m_K = 493.677 \text{ MeV}/c^2$ as the kaon mass. $\Gamma_\phi^{ee}(m)$ is defined as

$$\Gamma_\phi^{ee}(m) = \Gamma_\phi^{ee} \cdot (m_\phi/m) \cdot (k^{ee}(m)/k_\phi^{ee})^3,$$

where $k^{ee}(m) = \sqrt{m^2/4 - m_e^2}$ and $k_\phi^{ee} = \sqrt{m_\phi^2/4 - m_e^2}$ are phase space factors, with $m_e = 0.511 \text{ MeV}/c^2$ as the electron mass. Γ_ϕ^{ee} is the partial width of $\phi \rightarrow e^+e^-$ decay, defined as $\Gamma_\phi^{ee} = \Gamma_\phi^{tot} \times Br(\phi \rightarrow e^+e^-)$.

4.2.2 Physics processes which distort mass shape

In Figure 4.3 and 4.4 we show the higher-order Feynman diagrams, which distort the width and the decay rate of $\phi \rightarrow e^+e^-$ decays. They are the internal Bremsstrahlung, the vertex corrections, and the vacuum polarization. Amongst them, the internal Bremsstrahlung is most important, since the present experiment does not have any capability to eliminate a photon accompanied with a e^+e^- pair.

We evaluated an effect of the internal radiative corrections for the $\phi \rightarrow e^+e^-$ invariant mass spectrum according to [45]. The internal bremsstrahlung process, whose Feynman diagram is shown in Figure 4.3,

$$\phi(\vec{p}_0) \rightarrow e^-(\vec{p}_1) + e^+(\vec{p}_2) + \gamma(\vec{k})$$

is distributed in the phase space as [45]:

$$(4.3) \quad P(\zeta, \tau) \equiv \frac{1}{\Gamma_0} \frac{d^2\Gamma(\phi \rightarrow e^+e^-\gamma)}{d\zeta d\tau} \\ = \frac{\alpha}{2\pi} \left[\left(\frac{1+\zeta^2}{1-\zeta} \right) \left(\frac{1}{\tau} + \frac{1}{1-\zeta-\tau} \right) - \frac{a}{2} \left(\frac{1}{\tau^2} + \frac{1}{(1-\zeta-\tau)^2} \right) - 2 \right],$$

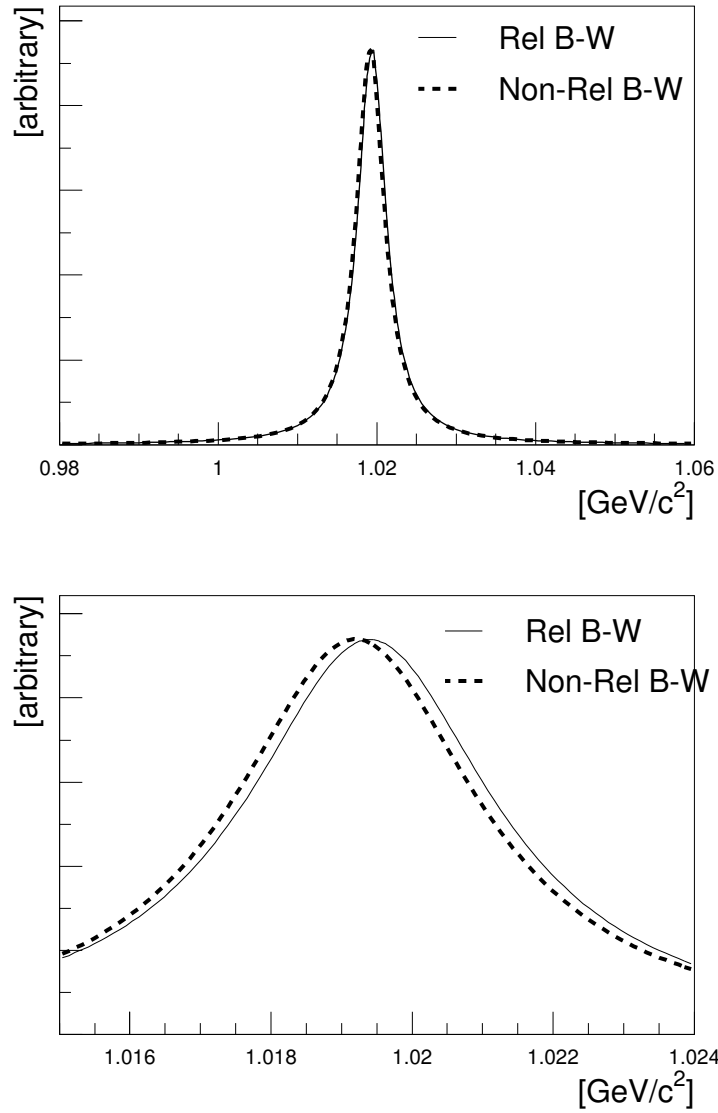


Figure 4.2: The relativistic and non-relativistic Breit-Wigner curves. The solid line and the dashed line represent the non-relativistic and relativistic Breit-Wigner curves, respectively. The lower panel is the magnification of the upper panel in the mass region from 1.015 to 1.024 GeV/c^2 .

where α is the fine structure constant, $\zeta = (\vec{p}_1 + \vec{p}_2)^2/M_\phi^2$, $\tau = (\vec{p}_0 - \vec{p}_1)^2/M_\phi^2$ and $a = 4m_e^2/M_\phi^2$. The probability distribution of photon energy $P(E_\gamma)$ is obtained by integrating $P(\zeta, \tau)$:

$$(4.4) \quad P(E_\gamma) \equiv \frac{1}{\Gamma_0} \frac{d\Gamma(\phi \rightarrow e^+e^-\gamma)}{dE_\gamma} = \frac{\alpha}{\pi} \frac{1}{E_\gamma} \left(1 + \frac{m^4}{M_\phi^4}\right) \left(\ln \frac{1+r}{1-r} - r\right),$$

where E_γ is the photon energy in the rest frame of the decaying particle, m is the invariant mass of the dilepton and $r = \sqrt{1 - a/\zeta}$. The probability distribution $P(E_\gamma)$ has singularity for $E_\gamma \rightarrow 0$. Taking into account the contributions from the virtual radiative correction, whose Feynman diagrams are shown in Figure 4.4, the divergence at $E_\gamma \rightarrow 0$ is cancelled out. Now, we split the amplitude of the Feynman diagram of the Figure 4.3 to a soft part and a hard part by setting $E_{min} = 0.1$ MeV as the splitting point.

In the hard part, we applied the above distributions to the process with photon energy E_γ greater than E_{min} . The fraction of decays corresponding to the emission of hard photons can be obtained by the integration of the $P(E_\gamma)$:

$$(4.5) \quad C_{hard}(E_{min}) \equiv \frac{1}{\Gamma_0} \cdot \Gamma(\phi \rightarrow e^+e^-\gamma, E_\gamma > E_{min}) = \int_{E_{min}}^{M_\phi(1-a)/2} P(E_\gamma) dE_\gamma.$$

If $E_{min} \ll M/2$, the result of the integration, neglecting terms of order $O(a)$, is known in Ref. [46]:

$$(4.6) \quad C_{hard}(E_{min}) = \frac{\alpha}{2\pi} \left[4 \ln \frac{M_\phi}{2E_{min}} \left(\ln \frac{M_\phi^2}{m_e^2} - 1 \right) - 3 \ln \frac{M_\phi^2}{m_e^2} - \frac{2}{3}\pi^2 + \frac{11}{2} \right].$$

In the soft part, the sum of the contributions from virtual radiative corrections and emitted soft photons ($\equiv C_{soft}$) is known as [46]:

$$(4.7) \quad C_{soft}(E_{min}) = \frac{\alpha}{2\pi} \left[-4 \ln \frac{M_\phi}{2E_{min}} \left(\ln \frac{M_\phi^2}{m_e^2} - 1 \right) + 3 \ln \frac{M_\phi^2}{m_e^2} + \frac{2}{3}\pi^2 - 4 \right].$$

The total width taking into account e^+e^- , $e^+e^-\gamma$ configurations is

$$(4.8) \quad \begin{aligned} \Gamma_{all}(\phi \rightarrow e^+e^-, e^+e^-\gamma) &= (1 + C_{soft} + C_{hard}) \cdot \Gamma_0(\phi \rightarrow e^+e^-) \\ &= \left(1 + \frac{\alpha}{2\pi} \frac{3}{2}\right) \cdot \Gamma_0(\phi \rightarrow e^+e^-). \end{aligned}$$

This means that inclusion of $e^+e^-\gamma$ decays increases the e^+e^- decay width by only $O(\alpha)$, however C_{soft} becomes negative so that the modification of the mass spectrum by C_{hard} becomes significant. Reference [45] showed the fraction of the events in the tail of di-electron mass spectra due to the internal radiative correction does not depend on the value of E_{min} when E_{min} is small enough.

Now, we can determine the probability of the emission of the hard photon by $(C_{hard})/(1 + C_{soft} + C_{hard})$. The effect from the soft photon emission ($0 < E_\gamma <$

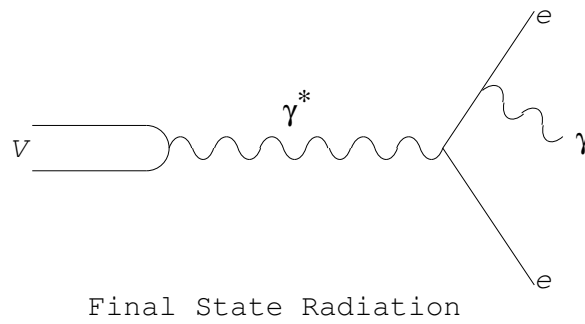


Figure 4.3: Feynman diagram for the internal bremsstrahlung in $V \rightarrow e^+e^-$ decays.

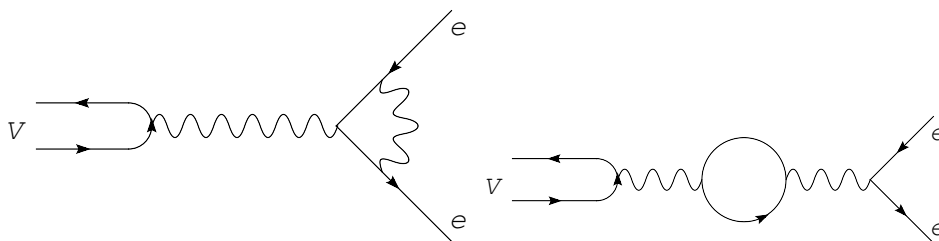


Figure 4.4: Feynman diagrams for the virtual radiative corrections. The left and right figures represent the vertex correction term and the vacuum polarization term, respectively.

$E_{min} = 0.1$ MeV) on the mass spectrum is negligible, and the momentum distributions of the e^+ and e^- in the hard photon emission process can be obtained by Eq. (4.3).

In the actual calculation, we took into account the effect from higher order corrections according to Ref. [47]. In the soft part, Eq.(4.7) can be written as

$$(4.9) \quad 1 + C_{soft} = 1 + \delta + \beta \ln\left(\frac{2E_{min}}{M_\phi}\right),$$

where β and δ are defined as

$$\beta \equiv \frac{2\alpha}{\pi} \left(\ln \frac{M_\phi^2}{m_e^2} - 1 \right), \quad \delta \equiv 3 \ln \frac{M_\phi^2}{m_e^2} + \frac{2}{3}\pi^2 - 4.$$

For small E_{min} , C_{soft} becomes large and negative such that it becomes necessary to estimate higher order corrections. Taking into account the higher order corrections, $1 + C_{soft}$ can be approximated as

$$(4.10) \quad (1 + C_{soft})^* = (1 + \delta) \left(\frac{2E_{min}}{M_\phi} \right)^\beta.$$

Corresponding to the above correction in the soft part, Eq.(4.4) in the hard part has to be modified to keep the continuity of the probability distribution function $P(E_\gamma)$ at $E_\gamma = E_{min}$;

$$(4.11) \quad P(E_\gamma)^* = (P(E_\gamma) + \frac{\beta \cdot \delta}{E_\gamma}) \left(\frac{2E_\gamma}{M_\phi} \right)^\beta.$$

We applied Eq.(4.10) and Eq.(4.11) to obtain the mass shape of the ϕ meson including internal radiative corrections. Figure 4.5 shows the mass shapes of the ϕ meson with and without the internal radiative corrections. We used the shape including the internal radiative corrections for the fit of the data.

4.2.3 Effect of the coulomb potential of target nuclei

The effect of the Coulomb potential of target nuclei was small enough to be ignored as follows. The magnitude of this effect was estimated with a Monte-Carlo calculation, in which only the Coulomb field of a target nucleus was considered. The potential $V(r)$ made by the target nucleus is given as

$$(4.12) \quad V(r) = \begin{cases} \frac{Ze^2}{2R_C} \left(3 - \left(\frac{r}{R_C} \right)^2 \right) & r \leq R_C \\ \frac{Ze^2}{r} & R_C \leq r \end{cases}$$

where Ze is the charge of the target nucleus, e is the charge of positron, R_C is the radius of the target nucleus and r is the radial distance from the center of the target nucleus. Mesons are generated in the nucleus according to the nuclear density profile.

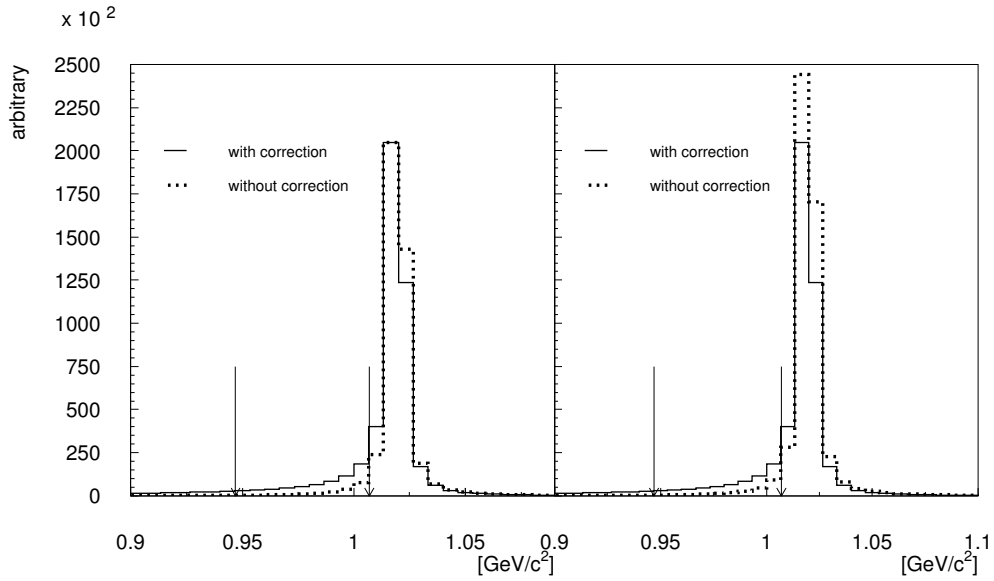


Figure 4.5: The mass distributions of e^+e^- pairs in $\phi \rightarrow e^+e^-$ and $\phi \rightarrow e^+e^-\gamma$ decays (with the internal radiative corrections) evaluated by the Monte Carlo technique. The solid lines represent the distributions taking into account the internal radiative corrections according to the literatures [45, 46], and the dashed lines represent the distributions without the corrections, in other words, the non-relativistic Breit-Wigner curve. In the left panel, the two lines are normalized at the peak. In the right panel, they are normalized by their integrals. The regions indicated by the arrows are from 0.947 to 1.007 GeV/c^2 , the excess region described in the text.

We considered ^{12}C and ^{63}Cu as target nuclei, whose radii (R_C in Eq. (4.12)) are 2.3 fm and 4.1 fm, respectively. The momenta of mesons were distributed as those produced by JAM. The mesons were considered to fly without any interaction, and decay into e^+e^- according to their natural total width. We have followed e^+ and e^- trajectories and bent them with the Coulomb potential $V(r)$ until they reached 10 nm away from the target nucleus. Then we reconstructed the invariant mass from the pairs. The results of the calculation for the differences between the original meson mass and the reconstructed mass in the ω meson case are shown in Figure 4.6. The changes of invariant mass shapes are negligible in the present experiment.

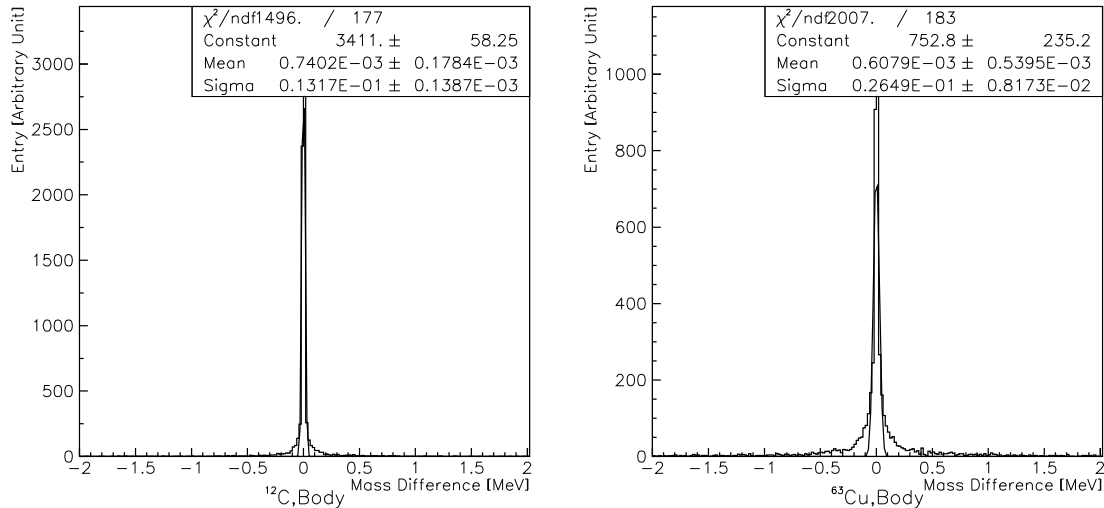


Figure 4.6: The effect of electromagnetic field of target nuclei, carbon (left) and copper (right). The solid lines represent the fit results with Gaussians

4.2.4 Monte Carlo simulation of the detector response

Other important sources which distort the resonance shape are in the detectors; interactions of particles in the detector materials and resolutions to measure particle trajectories.

In order to evaluate the invariant mass spectra to be observed, we performed a detailed detector simulation using GEANT4 toolkit [44]. All the experimental effects that affect the invariant mass spectrum, such as multiple scattering and energy loss of particles, tracking performance with the chamber resolutions are considered. We examined the reproducibility of the detector simulation using $K_s^0 \rightarrow \pi^+\pi^-$ and $\Lambda \rightarrow p\pi^-$ decays. The observed resolution and centroids of the resonances were well reproduced by this simulation, as described in Sec. 3.3.2. The effect from misalignments of the tracking devices was discussed in Section 3.3.2. This effect was studied separately and

4.3. THE FIT OF THE MASS SPECTRA WITH THE EXPECTED RESONANCE SHAPE87

	LR	RL
The number of the ϕ mesons in the data	3290	991
The data to JAM ratio of the ϕ mesons	0.0218 ± 0.0007	0.016 ± 0.001

Table 4.1: The number of the ϕ mesons in the data and the data to JAM ratio for LR and RL events.

the simulated mass shape was corrected, in the mass scale by a few MeV/c^2 and in the mass resolution from $10.1 \text{ MeV}/c^2$ to $10.7 \text{ MeV}/c^2$ (see Section 3.3.2).

For the ϕ meson kinematical distributions, we used the results of the nuclear cascade code, JAM 1.011.00 [48]. Figure 4.7 shows kinematical distributions of e^+e^- pairs in the ϕ meson mass region from 0.95 to $1.05 \text{ GeV}/c^2$. In obtaining those distributions of the experimental data, we subtracted the background by the side-band method. To obtain the background distributions in the ϕ meson mass region, the distributions in the regions 0.85 – $0.95 \text{ GeV}/c^2$ and 1.05 – $1.15 \text{ GeV}/c^2$ were averaged, and normalized by the number of the background events. The numbers of the background events were obtained from the quadratic curve in the fit result. The distributions of the data were reproduced well by JAM. We replaced the mass distribution of JAM by the one described in Section 4.2.2, and the mass-kinematical correlation in JAM was not used.

Although the JAM distributions reproduced well the real data, there remained discrepancies of about 25% concerning the ratio of the LR events (e^+ in the left arm and e^- in the right) to the RL events (vice versa). Table 4.1 shows the number of the ϕ mesons in the data and the ratio of the data to the JAM result for both event types. To reflect this discrepancy in the mass shape simulations, we used the observed LR/RL ratio in stead of the JAM LR/RL ratio, in order to sum up the simulated mass shapes in the LR events and the RL events.

Figure 4.8 shows the simulated ϕ meson mass shape to be applied in the data fitting. The tail component due to the internal radiative corrections and effects from the detector materials (energy loss and multiple scattering) is seen on the low mass side of the ϕ meson peak. The amount of the tail in the mass region from 0.947 to $1.007 \text{ GeV}/c^2$ is 11% (4% from the internal radiative corrections and 7% from the detector material) of all the ϕ mesons. This value of 11% is same for both target since we have employed very thin target (in the year 2002, $X_0 = 0.43\%$ and 0.54% for C and Cu target, respectively) so that the radiative tail due to the target thickness is negligibly small.

4.3 The fit of the mass spectra with the expected resonance shape

We fitted the observed mass spectra with the simulated resonance shape of $\phi \rightarrow e^+e^-$ decays described in the section 4.2 and a quadratic background curve. Figure 4.9 shows

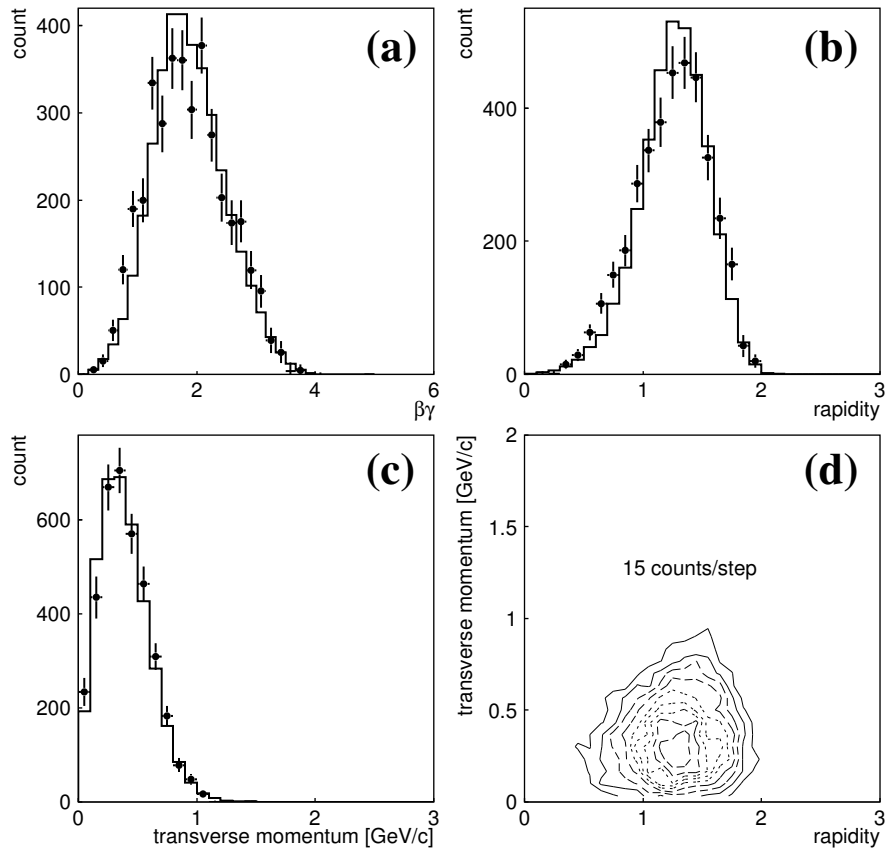


Figure 4.7: Kinematical distributions of e^+e^- pairs in the ϕ mass region from 0.95 to 1.05 GeV/ c^2 , as functions of (a) $\beta\gamma$, (b) rapidity, (c) transverse momentum, and (d) transverse momentum versus rapidity. The closed circles represent the real data and the histograms represent the simulation results obtained by using JAM and the detector simulation.

4.3. THE FIT OF THE MASS SPECTRA WITH THE EXPECTED RESONANCE SHAPE⁸⁹

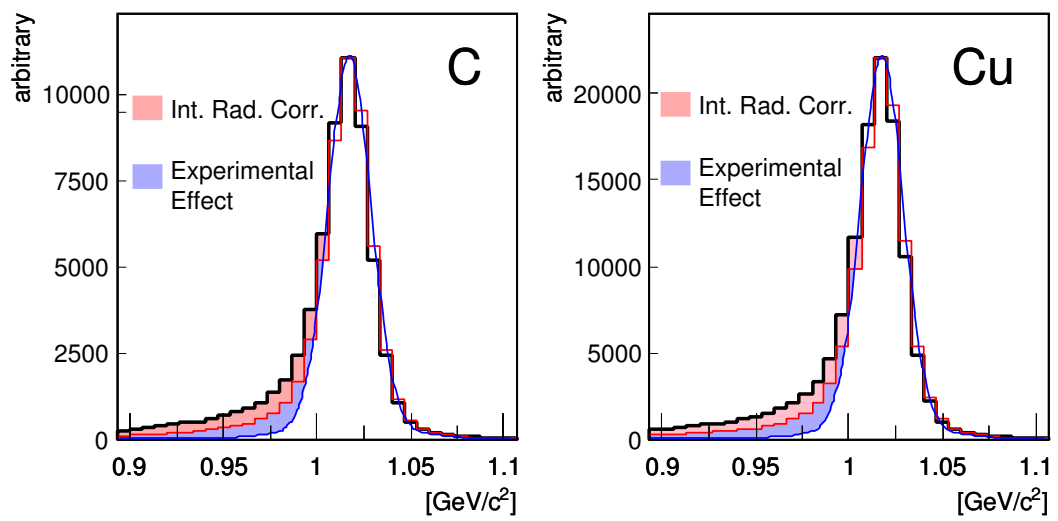


Figure 4.8: The simulation results for the expected mass shape of $\phi \rightarrow e^+e^-$ decays. The left and right panels are the results for the carbon and the copper targets, respectively. The black histogram represents the simulation results including all the effects from internal radiative corrections and the detectors. The red histogram represents the simulation results without the internal radiative corrections. The blue curve is the best fit for the red histogram with the Breit-Wigner curve convoluted with Gaußian. The red and blue areas denote the tail due to the internal radiative corrections and detector effects, respectively.

the fit results for the copper and the carbon target data. The fit regions are from 0.85 to 1.2 GeV/c^2 . The yield of the ϕ meson and coefficients of the quadratic curve were the fit parameters. The data were reproduced well by the fit with χ^2/ndf of 54.2/50 and 54.3/50 for the carbon and the copper data, respectively. There remains, however, a hint of an excess on the low mass side of the ϕ meson peak in the copper data.

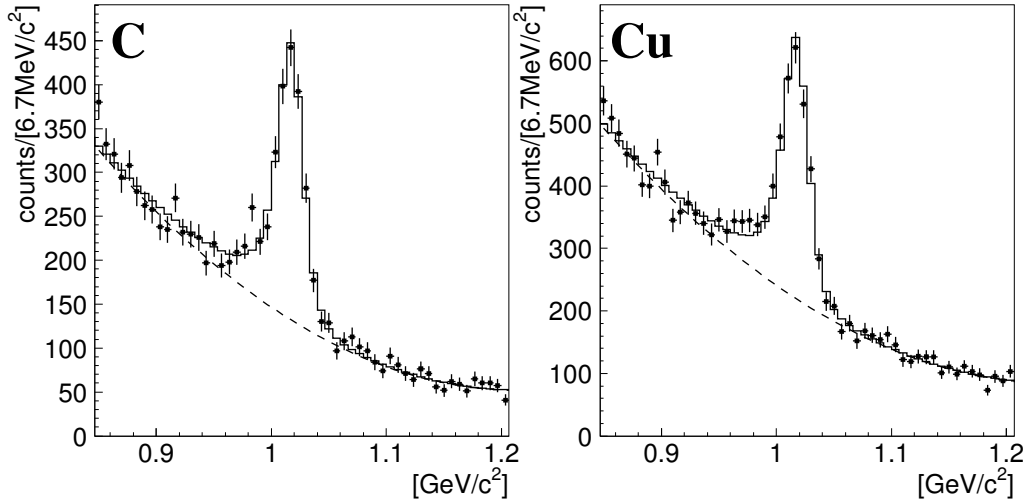


Figure 4.9: The e^+e^- mass distributions in the ϕ meson region with the best fits. The left panel is for the carbon data, and the right panel for the copper data. The closed circles with error bars represent the data. The solid lines represent the fit results with the expected $\phi \rightarrow e^+e^-$ shape and the quadratic background. The dashed lines represent a quadratic background.

To investigate the velocity dependence of the ϕ -meson mass spectra, we divided the data into three $\beta\gamma$ regions of the observed e^+e^- pairs, $\beta\gamma < 1.25$, $1.25 < \beta\gamma < 1.75$, and $1.75 < \beta\gamma$. We fitted each mass spectrum with a quadratic background curve and the expected resonance shape of $\phi \rightarrow e^+e^-$ decays. Please note that the simulation of the resonance shape was done separately for each $\beta\gamma$ region, where $\beta\gamma$ was reconstructed one from e^+e^- pairs in the simulation. The change of the shape as function of $\beta\gamma$ is not so significant as shown in Figure 4.10. The fit results are shown in Figure 4.11. The relative abundance of the ϕ mesons N_ϕ , and the parameters of the quadratic background were obtained from the fit over the region from 0.85 to 1.2 GeV/c^2 .

All the spectra were reproduced well by the fit except for the copper data in the lowest $\beta\gamma$ region, in which the obtained value of χ^2/ndf was 83/50. This means this particular mass spectrum cannot be reproduced by the applied resonance shape at 99% confidence level. Apparently the discrepancy was in the visible excess on the low mass side of the ϕ meson peak. On the other hand it is remarkable that the simulated shape, especially the tail, reproduces the copper data with $\beta\gamma > 1.75$, where we have the largest statistics.

4.3. THE FIT OF THE MASS SPECTRA WITH THE EXPECTED RESONANCE SHAPE91

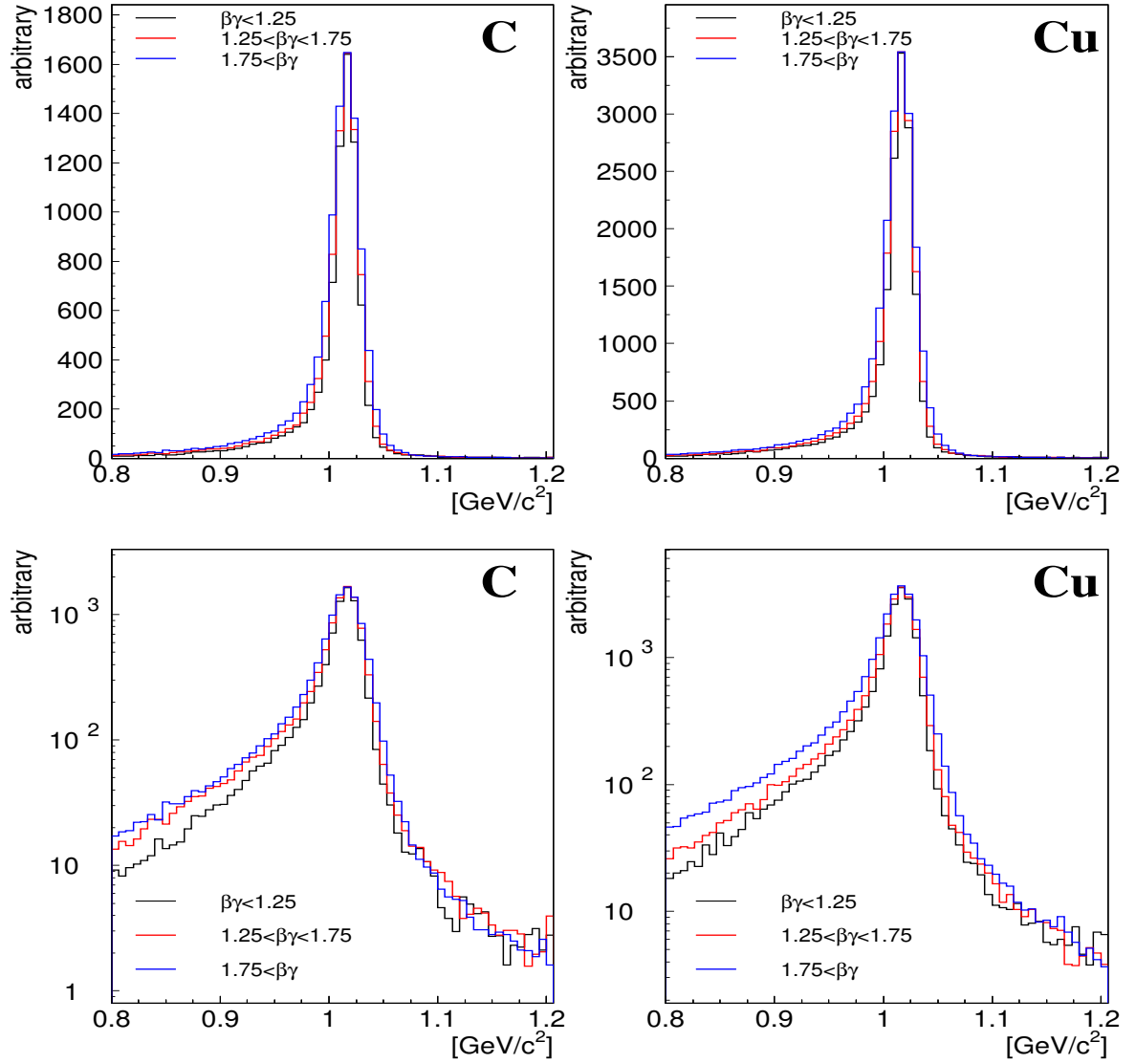


Figure 4.10: The simulated $\phi \rightarrow e^+e^-$ mass shapes as functions of $\beta\gamma$, for carbon and copper targets. Normalization was done at peak. Lower panels are plotted in log scale.

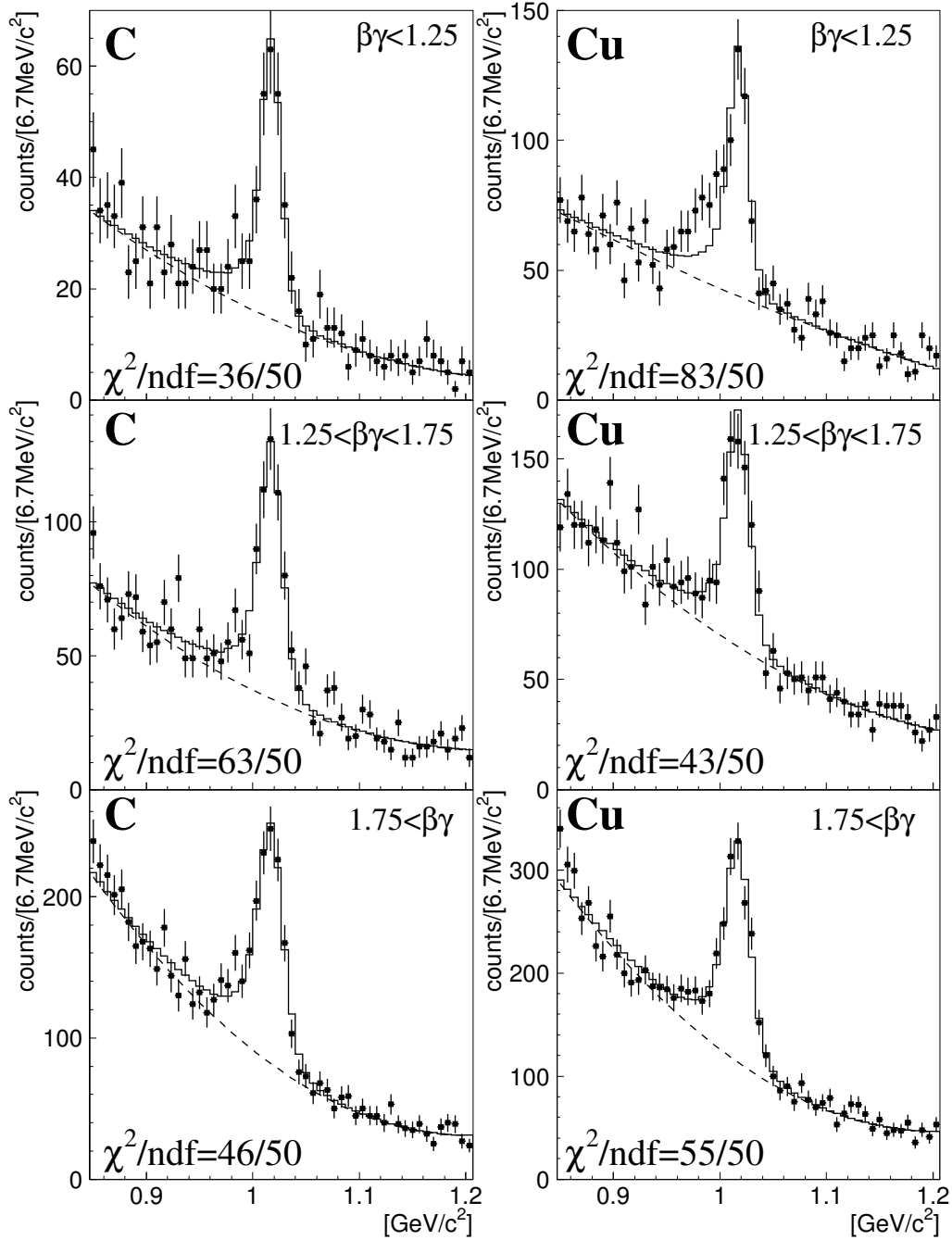


Figure 4.11: The e^+e^- invariant mass distributions for three $\beta\gamma$ regions and for the carbon and the copper targets. The closed circles with error bars represent the data. The solid lines represent the fit results with the expected $\phi \rightarrow e^+e^-$ shape over a quadratic background. The dashed lines represent the backgrounds.

		χ^2/ndf (a)	χ^2/ndf (b)
C	$\beta\gamma < 1.25$	36/50	31/41
	$1.25 < \beta\gamma < 1.75$	63/50	54/41
	$1.75 < \beta\gamma$	46/50	37/41
	all $\beta\gamma$	54/50	41/41
Cu	$\beta\gamma < 1.25$	83/50	57/41
	$1.25 < \beta\gamma < 1.75$	43/50	38/41
	$1.75 < \beta\gamma$	55/50	53/41
	all $\beta\gamma$	54/50	46/41

Table 4.2: The fit χ^2/ndf values (a) including and (b) excluding the excess region ($0.947 - 1.007 \text{ GeV}/c^2$).

4.4 Evaluation of the number of the excess

To evaluate the amount of excess N_{ex} , we repeated the same fit procedure excluding the mass region from 0.947 to $1.007 \text{ GeV}/c^2$ (nine bins)¹, where the excess was observed. The results are shown in Figure 4.12. All the distributions were well reproduced by the fit excluding the excess region. The obtained χ^2/ndf with including and excluding the excess region are listed in table 4.2.

We obtained N_{ex} by subtracting the integral of the fit results from that of the data in the mass region from 0.947 to $1.007 \text{ GeV}/c^2$. We estimated the systematic errors as described later in Section 4.4.1. The obtained values are listed in Table. 4.3. The ratios $N_{ex}/(N_{ex} + N_{\phi})$ are plotted in Figure 4.13. The excess is statistically significant for the copper target data in the lowest $\beta\gamma$ region, whereas these are marginal for other five regions. This excess is considered to be the signal of the mass modification of the ϕ mesons in a target nucleus because such an effect should be enhanced for slower ϕ mesons produced in a larger target nucleus, because of the increase of the in-medium decay rate.

4.4.1 Systematic errors

The systematic errors for N_{ϕ} , N_{ex} and $N_{ex}/(N_{ex} + N_{\phi})$ were evaluated by changing the fit conditions as follows;

- (A) The fit region was changed from $0.85 - 1.2 \text{ GeV}/c^2$ to $0.9 - 1.2 \text{ GeV}/c^2$.
- (B) The bin width was changed from $6.7 \text{ MeV}/c^2$ to 5 or $10 \text{ MeV}/c^2$.
- (C) The mass scale was changed according to the systematic error due to the uncertainty of the magnetic field map and the BDC alignment (see Table 3.4 in

¹In the analysis, we divided the $400 \text{ MeV}/c^2$ mass range ($0.8 - 1.2 \text{ GeV}/c^2$) of the data into 60 bins. Thus the bin width is $6.67 \text{ MeV}/c^2$.

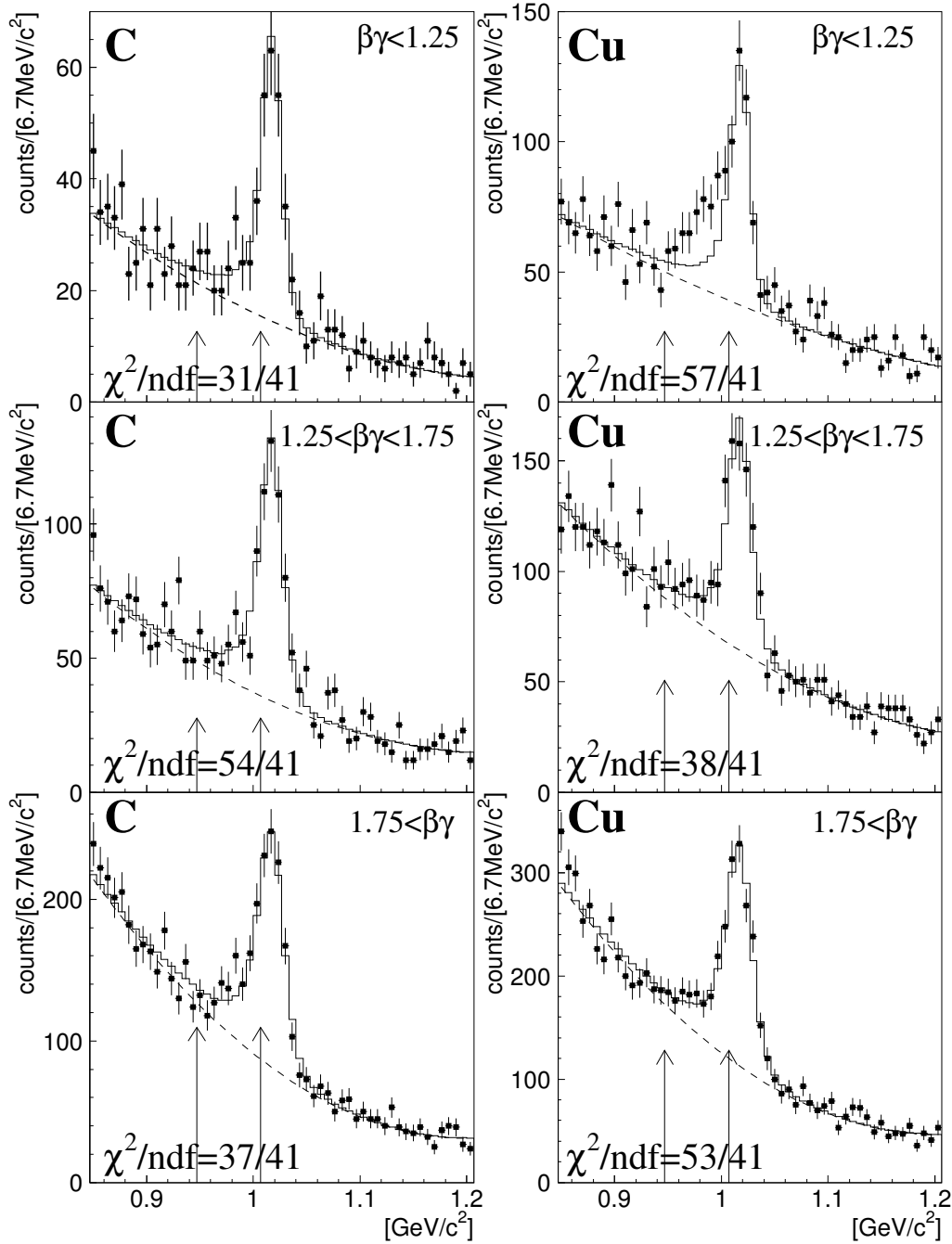


Figure 4.12: The same plot as Figure 4.11 but with the fit results excluding the excess region, $0.947 - 1.007 \text{GeV}/c^2$. The excluded region is indicated by the vertical arrows in each panel. The target and $\beta\gamma$ -region are shown in each panel.

		N_{ex}	N_{ϕ}	$N_{ex}/(N_{ex}+N_{\phi})$
C	$\beta\gamma < 1.25$	$6 \pm 17_{-6}^{+7}$	$257 \pm 26_{-7}^{+6}$	$0.02 \pm 0.06_{-0.01}^{+0.02}$
	$1.25 < \beta\gamma < 1.75$	$-4 \pm 26_{-12}^{+10}$	$547 \pm 41_{-15}^{+13}$	$-0.01 \pm 0.05_{-0.01}^{+0.02}$
	$1.75 < \beta\gamma$	$39 \pm 42_{-25}^{+22}$	$1076 \pm 64_{-15}^{+12}$	$0.04 \pm 0.04_{-0.01}^{+0.02}$
Cu	$\beta\gamma < 1.25$	$133 \pm 28_{-12}^{+5}$	$464 \pm 38_{-5}^{+6}$	$0.22 \pm 0.04_{-0.01}^{+0.01}$
	$1.25 < \beta\gamma < 1.75$	$35 \pm 33_{-12}^{+9}$	$588 \pm 47_{-8}^{+14}$	$0.06 \pm 0.05_{-0.01}^{+0.01}$
	$1.75 < \beta\gamma$	$21 \pm 48_{-29}^{+25}$	$1367 \pm 72_{-27}^{+24}$	$0.02 \pm 0.03_{-0.01}^{+0.02}$

Table 4.3: Numbers of ϕ meson [N_{ϕ}] and excess [N_{ex}] evaluated by the fits excluding the excess region (see text). Error values are statistical (first) and systematic (second).

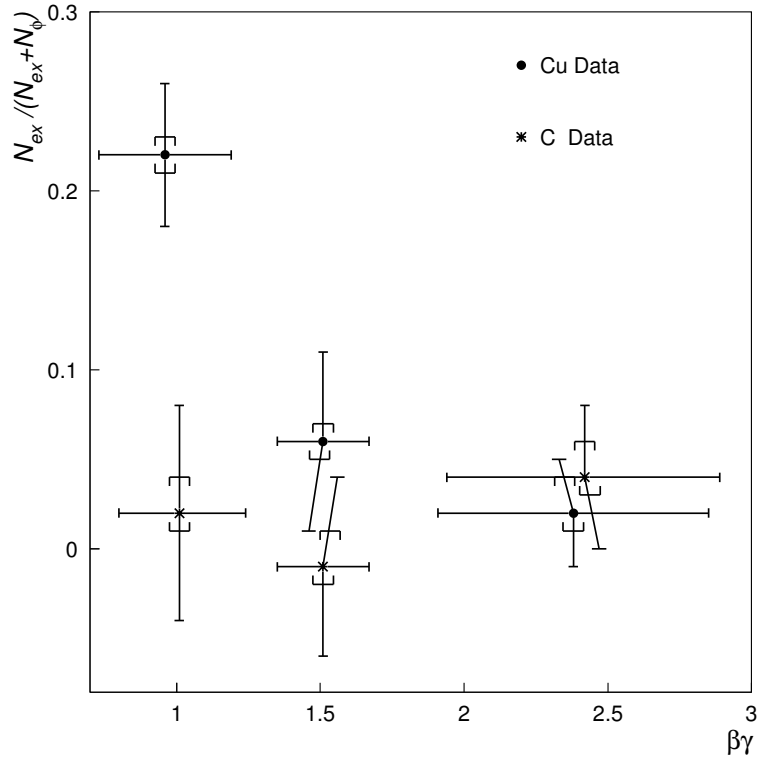


Figure 4.13: The $\beta\gamma$ dependence of $N_{ex}/(N_{\phi} + N_{ex})$. Points represent the data described in Section 4.4. The brackets indicate the systematic errors evaluated in the Section 4.4.1. The vertical error bars indicate the statistical errors and horizontal error bars indicate the standard deviations of the $\beta\gamma$ distribution in each $\beta\gamma$ bin.

Section 3.3.2).

- (D) The additional mass resolution was changed according to the systematic error also due to the uncertainty of the magnetic field map and the BDC alignment (see Table 3.4 in Section 3.3.2).
- (E) The kinematical distributions of the ϕ mesons in the simulation were changed from the one generated by JAM to the observed ones.
- (F) We adopted the cubic curve instead of the quadratic curve for the back ground distribution.
- (G) We changed the shape of the ϕ meson in the simulation from the non-relativistic Breit-Wigner Eq. (4.1) to the relativistic Breit-Wigner Eq. (4.2).

We repeated the fit procedure by applying the changes above and obtained the N_ϕ and N_{ex} independently. Then we averaged the obtained values for N_ϕ and N_{ex} and show them in Table 4.3. For the systematic errors we took the maximum deviations from the averages. For the statistical errors we selected the largest one among the above fit conditions. Figure 4.14 summarizes the stability of N_{ex} and N_ϕ with the above fit conditions.

4.5 Theoretical interpretation

We attempted to reproduce the observed mass spectra with a Monte-Carlo-type model calculation that includes the in-medium mass modification of the ϕ mesons based on the theoretical predictions [7, 9].

4.5.1 Model calculation with mass modification

We have performed a model calculation to examine how the observed excess can be understood within a theoretical scenario of meson mass modification.

We assumed the density dependence of the pole mass change of the ϕ meson as $m_\phi(\rho)/m_\phi(0) = 1 - k_1(\rho/\rho_0)$, where ρ_0 is normal nuclear density following the prediction by Hatsuda and Lee [7]. In fact, the $m_\phi(\rho)$ of their prediction is not a pole mass but an average value of the mass spectrum. In the case of broad resonance as ρ , the pole and the average could be different significantly. But for a narrow resonance like ϕ , the two are expected to be almost the same. Thus we used such a formula for the pole mass modification.

To reproduce the amount of excess observed in our data (22% for slow ϕ in the copper target data), it is necessary to introduce a broadening of the total width of ϕ (Γ_ϕ^{tot}), or at least of the partial width for the $\phi \rightarrow e^+e^-$ decay (Γ_ϕ^{ee}). When no broadening is introduced, the expected rate of in-nucleus decay is just 6(3)% for the ϕ mesons produced in copper (carbon) nuclei even with $\beta\gamma < 1.25$. For the density

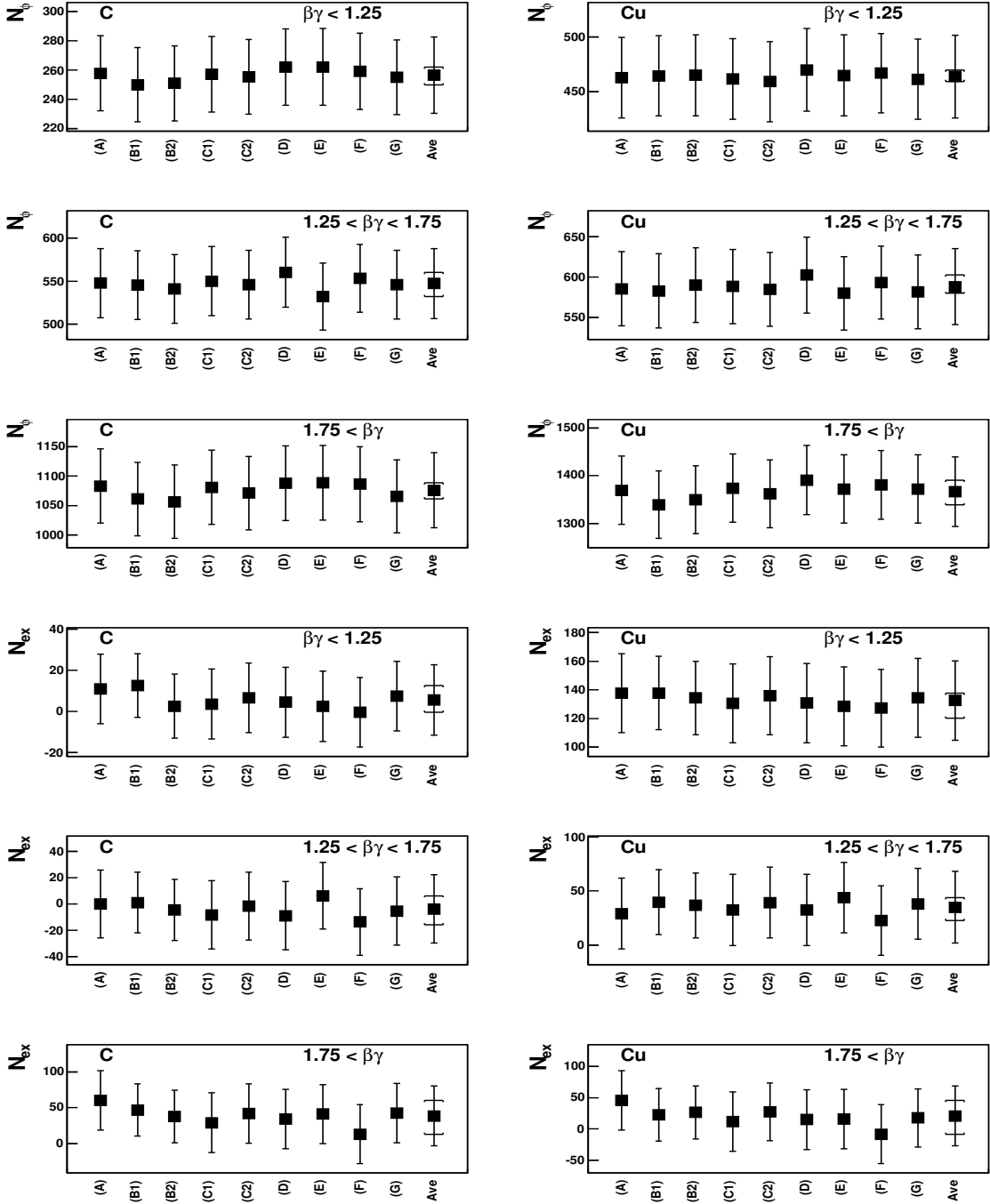


Figure 4.14: The obtained N_ϕ and N_{ex} in the study of systematic errors for the different fit conditions (see text). Upper six panels show N_ϕ and lower six panels show N_{ex} . (B1) and (B2) are for the results with 5 and 10 MeV/ c^2 bin width, respectively. (C1) and (C2) are for the results with plus and minus systematic errors of the mass scale in Table 3.4, respectively. The error bars represent the statistical errors. The averaged value is also shown in the last bin in each panel. The statistical error assigned to the averaged value is the largest value of statistical errors among all the fit conditions. The systematic error indicated on the average by brackets represents the maximum deviation from the average.

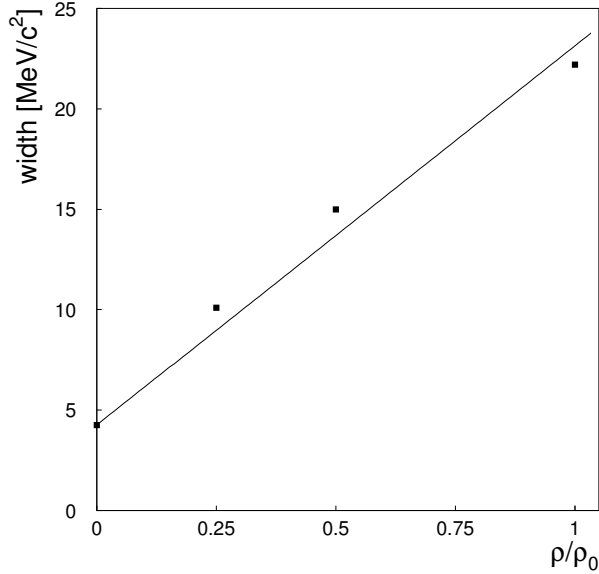


Figure 4.15: The prediction for the in-medium width broadening of the ϕ meson by Oset and Ramos [9]. The points represent the predicted values. The solid line is the best-fit result: $\Gamma_{\phi}^{\text{tot}}(\rho)/\Gamma_{\phi}^{\text{tot}}(0) = 1 + 4.4(\rho/\rho_0)$.

dependence of the total width broadening, we assumed $\Gamma_{\phi}^{\text{tot}}(\rho)/\Gamma_{\phi}^{\text{tot}}(0) = 1 + k_2^{\text{tot}}(\rho/\rho_0)$. Although there are no theoretical foundation for such a linear formula on the width broadening, it is numerically consistent with the prediction by Oset and Ramos [9] for the ϕ meson width broadening in the nucleus. If we take their prediction, we obtain $k_2^{\text{tot}} = 4.4 \pm 0.2$ as shown in Figure 4.15.

For Γ_{ϕ}^{ee} , partial decay width to e^+e^- , we also assumed $\Gamma_{\phi}^{ee}(\rho)/\Gamma_{\phi}^{ee}(0) = 1 + k_2^{ee}(\rho/\rho_0)$, and examined following two cases: (i) the branching ratio $\Gamma_{\phi}^{ee}/\Gamma_{\phi}^{\text{tot}}$ remains unchanged in the medium, i.e. $k_2^{ee} = k_2^{\text{tot}}$, and (ii) Γ_{ϕ}^{ee} doesn't increase in the medium, i.e. $k_2^{ee} = 0$. Although it is desirable to determine the parameter k_2^{tot} and k_2^{ee} independently, the statistics of the present data is insufficient to do so. In vacuum the partial decay widths are determined with the decay Q values and the overlap of the wave functions of s and \bar{s} -quark. The total decay width $\Gamma_{\phi}^{\text{tot}}$ is as narrow as $4.26 \text{ MeV}/c^2$ simply because the decay Q value to the main mode, $K\bar{K}$, is small ($32 \text{ MeV}/c^2$ for K^+K^- and $24 \text{ MeV}/c^2$ for $K^0\bar{K}^0$). Thus there is no reason to believe $\Gamma_{\phi}^{ee}/\Gamma_{\phi}^{\text{tot}}$ to be constant even in nuclear medium. On the other hand, there also is no reason to believe $\Gamma_{\phi}^{ee}(\rho) = \Gamma_{\phi}^{ee}(0)$ since the wave function of the ϕ meson can easily be modified if the chiral symmetry is partially restored. Thus the above two assumptions, (i) and (ii) should be considered as two extreme cases. Please note that the two assumptions have a common parameter space

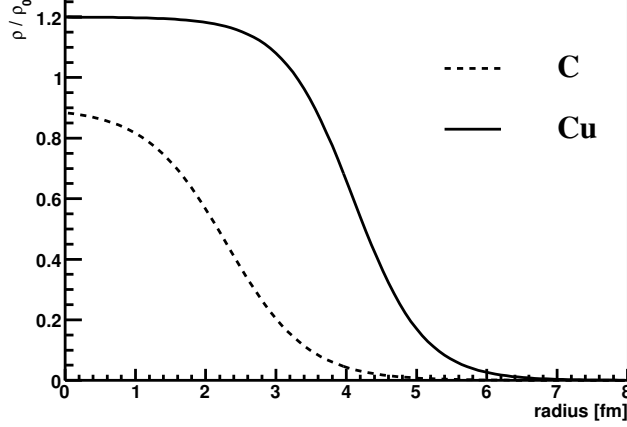


Figure 4.16: Woods-Saxon distributions for the nuclear density profile used in the model calculation. The solid line for the copper nuclei, and the dashed line for carbon nuclei.

when $k_2^{\text{tot}} = 0$.

In the model calculation we considered that ϕ mesons were generated in the target nucleus according to the nuclear density profile. This is reasonable because we measured the mass-number dependence of the ϕ meson production cross section almost as $\sigma(A) \propto A^1$ [49]. Generated ϕ mesons were traced until the decay point with the modified pole mass and the decay width according to the nuclear density distribution. The decay probability increased in the nucleus due to the width broadening. We used the Woods-Saxon distribution for the nuclear density distribution, which is shown in Figure 4.16 as a function of the radial coordinate r with the equation of ;

$$\rho/\rho_0(r) = \frac{N}{1 + \exp(\frac{r-R}{\tau})},$$

where $R = 4.1(2.3)$ fm, $\tau = 0.50(0.57)$ fm and $N = 1.2(0.9)$ for the copper(carbon) target. Here, R is the half density radius of the nucleus and the surface thickness t is related to τ as $t = 4 \times \ln(3) \times \tau = 4.4 \times \tau$ [50]. The values for R and t for copper are given from the data of the p-A scattering [50] and an approximation $R = 1.02 \times A^{1/3}$ and $t = 2.5$ is used for carbon. The normalization factor N was determined to satisfy that the volume integral of these distribution is equal to the mass number of carbon or copper.

We modified the Breit-Wigner shape of the ϕ meson with the parameters k_1 and k_2^{tot} . Then we performed the simulation to take into account the internal radiative corrections and the detector effects. Figure 4.17 and 4.18 show the simulated mass shapes with typical model parameters of k_1 and k_2^{tot} in the cases (i) and (ii). The in-medium modification of ϕ meson makes the tail component in the excess region. In the case (i), the amount of the tail increases with k_2^{tot} , especially in the copper target

		$k_2^{ee} = k_2^{\text{tot}}$ (case (i))					
		k_2^{tot}					
		0	2	4	6	8	10
k_1	0.05	321.96	320.82	324.75	330.84	338.96	342.25
	0.04	320.79	317.36	319.15	326.15	328.28	332.19
	0.035	320.04	315.60	317.59	322.39	324.67	328.59
	0.03	321.63	316.22	318.49	320.54	323.33	327.52
	0.02	322.52	319.40	319.61	318.72	321.40	322.28
		$k_2^{ee} = 0$ (case (ii))					
		k_2^{tot}					
		0	2	4	6	8	10
k_1	0.05	321.96	323.92	322.63	323.03	323.97	323.49
	0.04	320.79	321.30	321.77	321.96	324.71	324.02
	0.035	320.04	321.92	322.36	322.02	321.91	325.84
	0.03	321.63	320.11	322.12	321.05	321.63	324.36
	0.02	322.52	322.99	321.77	323.87	324.09	325.54

Table 4.4: The obtained χ^2 values by the fit with the modified resonance shape of the ϕ meson with various sets of k_1 and k_2^{tot} . Degree of freedom (dof) is 298 in the both cases.

results, while in the case (ii), the spectrum does change very little, and it is noteworthy that the amount of the tail decreases when k_2^{tot} increases because the ratio $\Gamma_\phi^{ee} / \Gamma_\phi^{\text{tot}}$ decreases accordingly.

4.5.2 Best fit parameters for pole shift and width broadening of ϕ meson

For both case (i) and case (ii) assumptions, we searched the parameter space of k_1 and k_2^{tot} to find out the set which gave the best χ^2 . We fit the six invariant mass spectra in Figure 4.11 (2 targets \times 3 $\beta\gamma$ regions) simultaneously with a set of k_1 and k_2^{tot} , without excluding the excess region in the mass spectra.

It is technically difficult to change the mass shape continuously with the parameters k_1 and k_2^{tot} in the χ^2 minimization. Thus, we scanned the parameter region from 0.2 to 0.5 in k_1 and from 0 to 10 in k_2^{tot} . The obtained χ^2 values are listed in Table 4.4. By smoothing the values in Table 4.4 using a quadratic curve for both k_1 and k_2^{tot} axis, the confidence ellipsoids and the best parameter sets were obtained for the case (i) and (ii), as shown in Figure 4.19.

In the case (i), the obtained best-fit parameters are $k_1 = 0.034_{-0.007}^{+0.006}$, $k_2^{\text{tot}} = 2.6_{-1.2}^{+1.8}$, and the minimum $\chi^2(\chi_{\text{min}}^2)/ndf$ is 316.4/298. In the case (ii), the best-fit parameters are $k_1 = 0.033_{-0.008}^{+0.011}$, $k_2^{\text{tot}} = 0^{+5.6}$, and the χ_{min}^2/ndf is 320.8/298. In Figure 4.20 we overplot the best-fit results of the modified mass shape on the observed spectra. Fig-

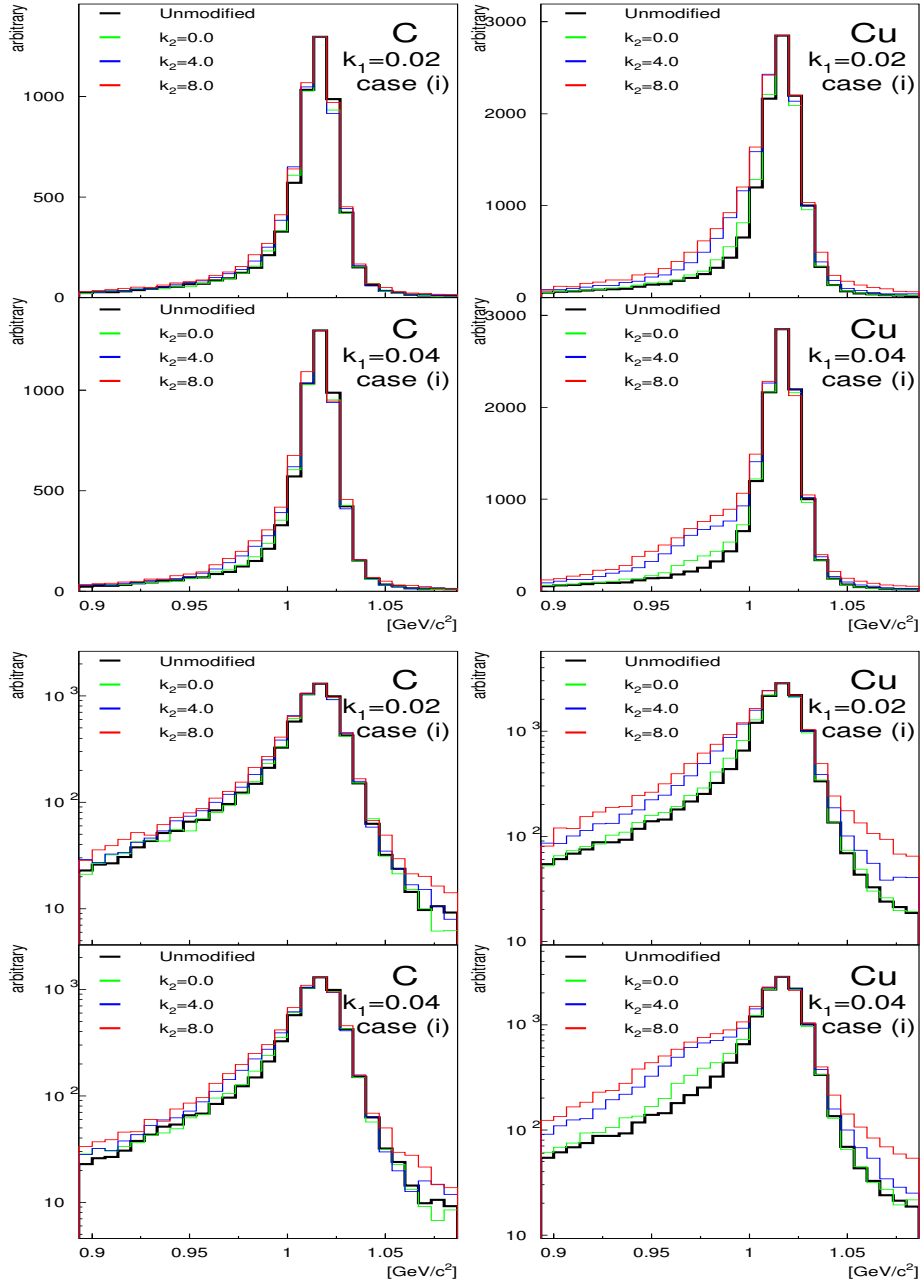


Figure 4.17: The results of the model calculation for the modified ϕ meson resonance shape with typical k_1 and k_2^{tot} in the case (i). The lower four panels are log scale plots of the upper four panels. The internal radiative corrections and the detector effects are taken into account. The green, blue and red lines represent the result with $k_2^{\text{tot}} = 0.0, 4.0, 8.0$, respectively. The black lines show the unmodified ϕ meson shape for the reference. Normalization in each panel was done at the bin with the maximum entries.

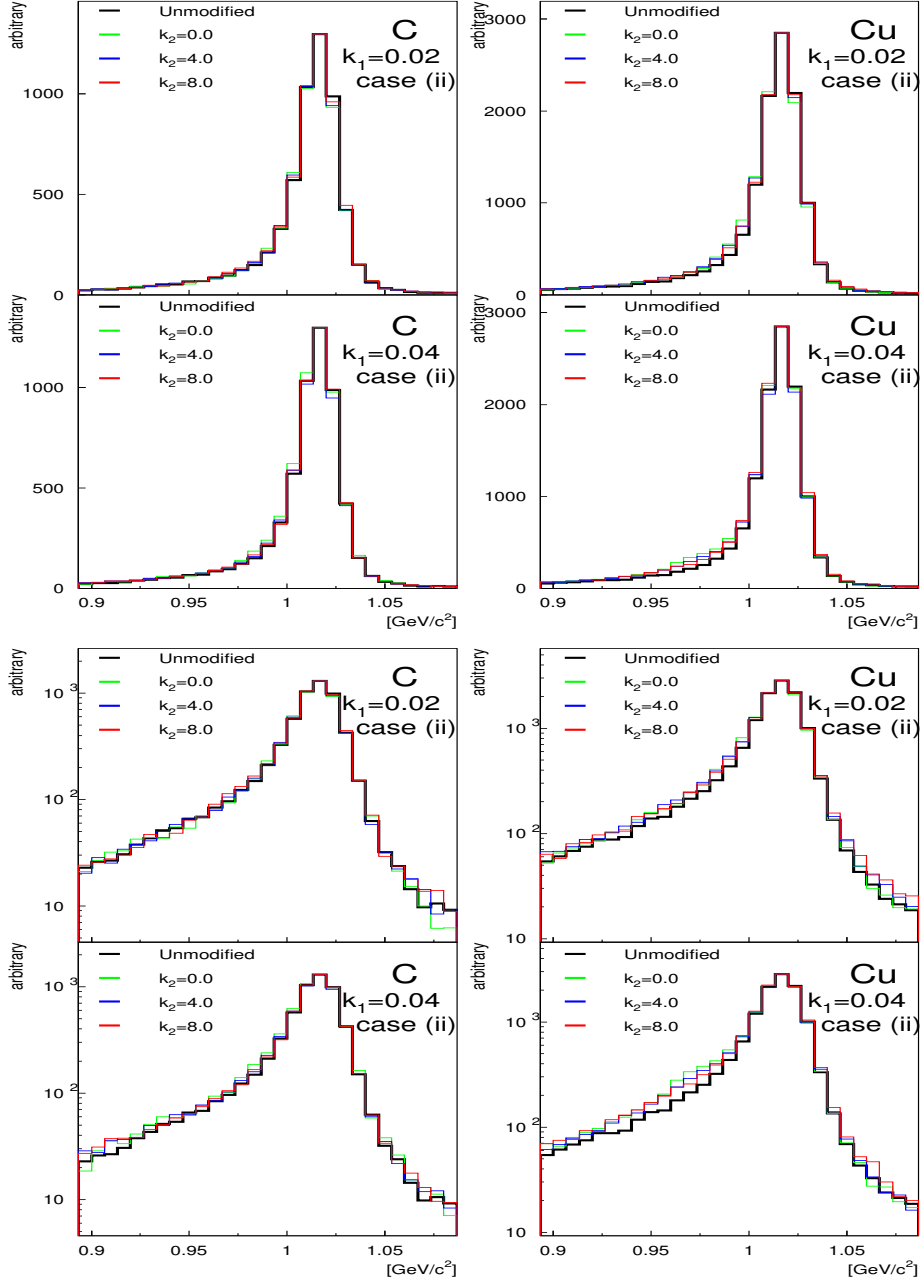


Figure 4.18: The results of the model calculation for the modified ϕ meson resonance shape with typical k_1 and k_2^{tot} in the case (ii). The lower four panels are log scale plots of the upper four panels. The green, blue and red lines represent the result with $k_2^{tot} = 0.0, 4.0, 8.0$, respectively. The black lines show the unmodified ϕ meson shape for the reference. Normalization in each panel was done at the bin with the maximum entries.

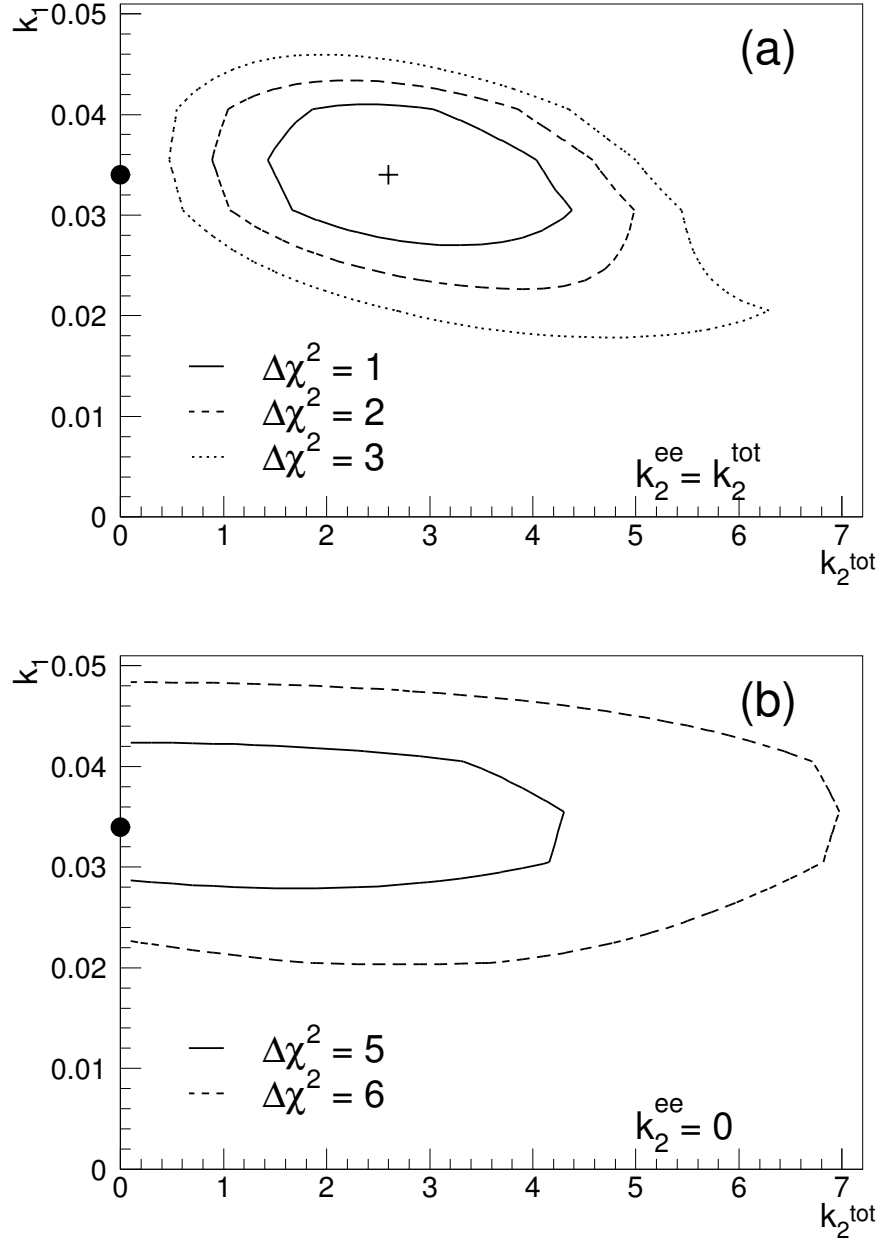


Figure 4.19: Confidence ellipsoids for the modification parameters k_1 and k_2^{tot} . The upper and lower panel corresponds to the case (i): $k_2^{\text{ee}} = k_2^{\text{tot}}$ and (ii): $k_2^{\text{ee}} = 0$, respectively. In each panel, the $\Delta\chi^2$ s denote differences from the minimum χ^2 in the case (i), whose location is shown by the cross in the panel (a). The best fit point in case (ii) is shown by the closed circle in the panel (b), and it is also plotted in (a) since the parameter spaces in both ordinates are common to both figures, i.e. $k_2^{\text{ee}} = k_2^{\text{tot}} = 0$.

ure 4.21 shows the result of the model calculation for the copper target in the lowest $\beta\gamma$ region with the best-fit parameters, $k_1 = 0.034$ and $k_2^{\text{tot}} = k_2^{ee} = 2.6$, together with the shapes for in-vacuum decays and in-medium decays. Here, the ϕ mesons which decayed where the nuclear density was more than half of the maximum were considered as "in-medium" decay ϕ mesons.

It is very interesting that in both cases the χ_{min}^2 was obtained with $k_1 \simeq 0.034$, meaning that the decrease of pole mass of the ϕ meson is strongly suggested from the data. The χ_{min}^2 in the case (ii) (= 320.8) is larger than that in the case (i) (= 316.4) by 4.4. It should be noted that when we fit the data with the simulation shape with the parameters of k_1 and k_2^{tot} determined above, and calculated the χ^2 only for the copper data in the lowest $\beta\gamma$ region, χ^2/ndfs were 66/48 and 74/48 for the case (i) and (ii), respectively. Namely only the case (ii) was statistically rejected at 99% C.L. The data thus favor the increase of Γ_{ϕ}^{ee} , by a factor of 3.6 at normal nuclear density.

Furthermore, we fit only the copper data in the lowest $\beta\gamma$ region, where the major discrepancy occurred, instead of the simultaneous fit for the six spectra. In the case (ii), the fit was rejected again at 99% C.L. and the best-fit parameters of k_1 and k_2^{tot} did not change. In the case (i), the obtained best-fit parameters are $k_1 = 0.031_{-0.003}^{+0.005}$ and $k_2^{\text{tot}} = 6.1_{-1.5}^{+2.3}$ with $\chi^2/\text{ndf} = 63.4/48$, which are consistent within 2σ with the results of the simultaneous fit for the six spectra, but favoring large k_2^{ee} . The best-fit result in the case (i) is shown in Figure 4.22.

4.6 Comparison with ρ and ω mesons

In our earlier publication [5, 42], we reported the modification of the e^+e^- mass spectra for ρ and ω mesons. In the case of ρ and ω mesons, we observed the excess over the known hadronic sources both for carbon and copper targets. In the case of the ϕ meson, however, we observed the excess only in the copper target data with small $\beta\gamma$. This is not inconsistent since the ρ -meson lifetime ($c\tau \simeq 1.3$ fm) is shorter than the typical nuclear size and a significant portion of ρ mesons should decay in both carbon and copper nuclei in the measured kinematical region ($1 < \beta\gamma_{\rho} < 3$), while the ϕ -meson lifetime ($c\tau \simeq 46$ fm) is much longer. Table 4.5 shows the model calculations for the percentages of in-medium decays for ρ and ϕ mesons when there are no width broadening. Here the detector acceptance was not taken into account. For the ϕ meson, the percentages in the region of $\beta\gamma < 1.25$ are also shown. We considered the mesons which decayed where the nuclear density was more than half of the maximum, as "in-medium" decay mesons. It can be concluded that the modification, if exists, should be visible for the ρ meson with both targets, while for the ϕ meson it may well require some kinematical and target selections to see the modification over the limited statistics in the data.

In respect to the pole mass shift and the width broadening, the analyses for ρ and ω mesons with the model calculations have shown the decrease of the pole mass by 9.2% at normal nuclear density, and large width broadening, such as a factor of two

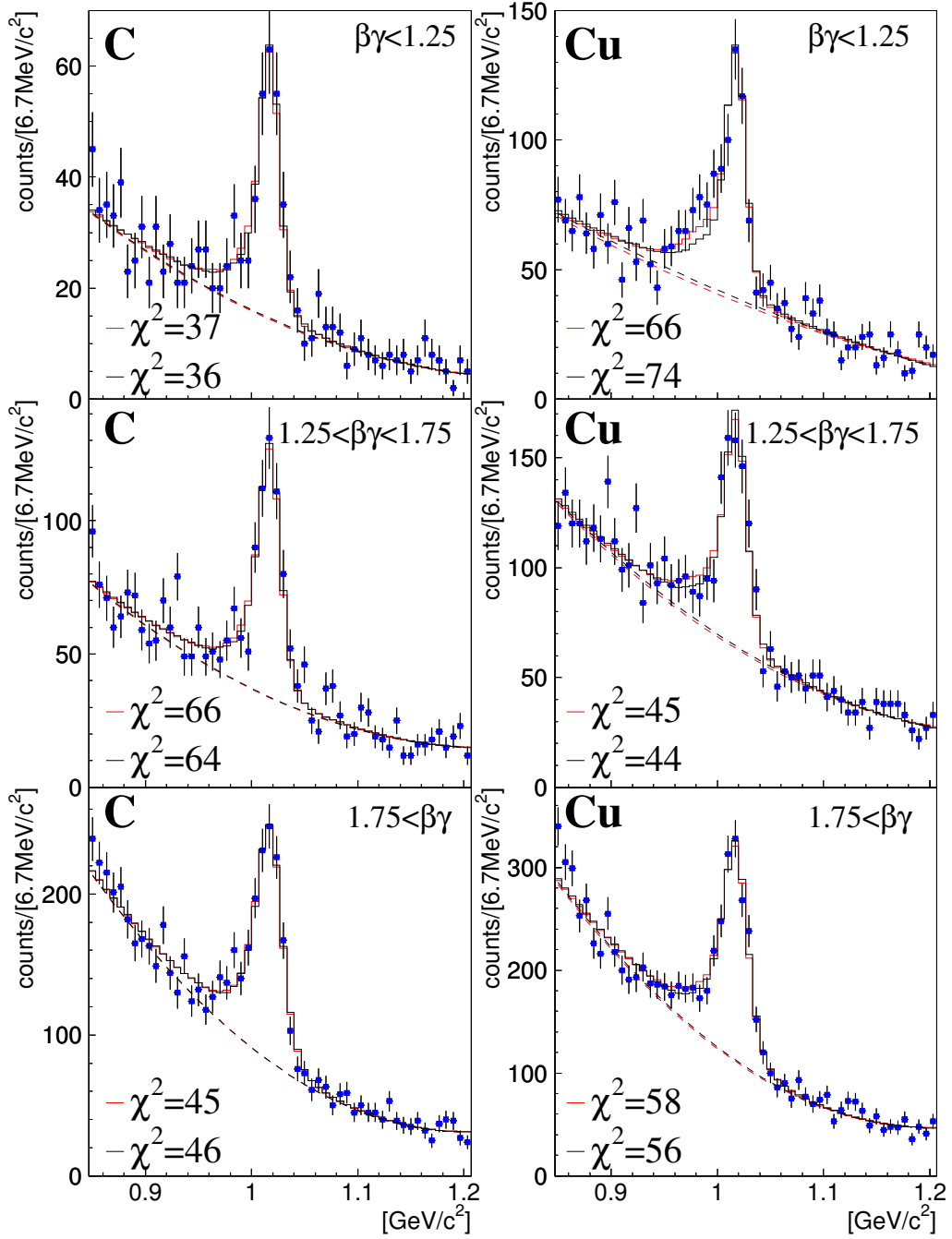


Figure 4.20: The same invariant mass spectra of e^+e^- pairs as Figure 4.11, with the best fit results for the case (i) ($k_2^{ee} = k_2^{\text{tot}}$, red line) and (ii) ($k_2^{ee} = 0$, black line). The solid lines represent the fit results with the modified mass shape and a quadratic background. The dashed lines represent the background curve. The shift parameter k_1 and broadening parameters k_2^{tot} and k_2^{ee} are common to the six spectra in each case. The values of χ^2 's shown in each panel are the sum of the squares of the deviations over 54 data points for the case (i) and (ii) in each spectrum.

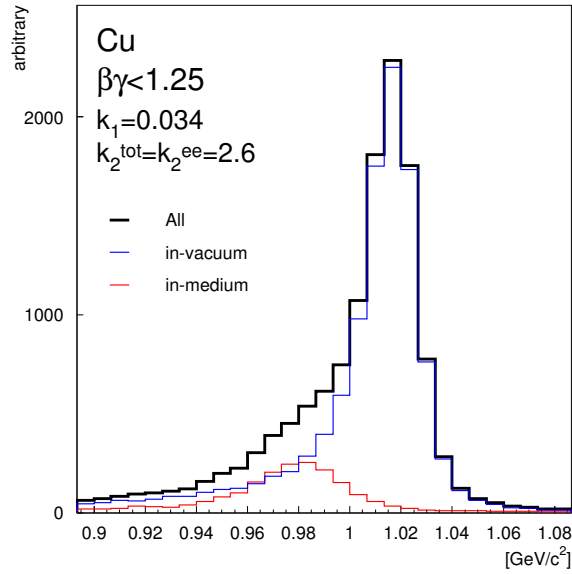


Figure 4.21: The result of the model calculation for the copper target in the lowest $\beta\gamma$ region with the best fit parameters, $k_1 = 0.034$ and $k_2^{\text{tot}} = k_2^{ee} = 2.6$. The blue and red histogram represent the shape for in-vacuum decay and in-medium decay, respectively.

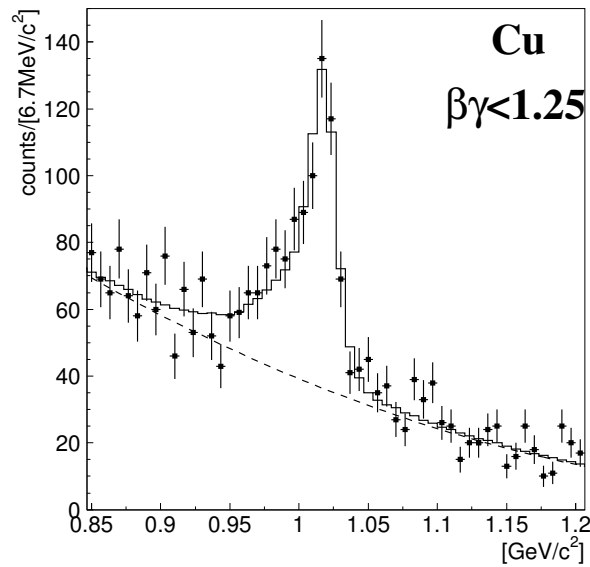


Figure 4.22: The e^+e^- invariant mass spectrum of the copper targets in the lowest $\beta\gamma$ region with the best fit results, $k_1 = 0.031$ and $k_2^{\text{tot}} = 6.1$, for the case (i) ($k_2^{ee} = k_2^{\text{tot}}$). The fit for the parameters k_1 and k_2^{tot} was performed with only this spectrum instead of the simultaneous fit for the six spectra.

	ρ	ϕ	
	all $\beta\gamma$	all $\beta\gamma$	$\beta\gamma < 1.25$
C	49 %	1 %	3 %
Cu	61 %	3 %	6 %

Table 4.5: The percentages of in-medium decays obtained by the simulation without any in-medium modification and intra-nuclear scattering. The ϕ mesons are assumed to be produced uniformly in the nucleus, while the ρ mesons are at the surface of incident hemisphere of the target nucleus. These assumptions are reasonable since the nuclear mass number dependences of vector meson production are roughly $\sigma_\phi(A) \propto A^1$ and $\sigma_\omega(A) \propto A^{0.7}$, as measured in the present experiment [49].

or more, is not favored by the data [42]. In the case of ϕ mesons, the data indicate the decrease of the pole mass by 3.4% and width-broadening by a factor of 3.6 at normal nuclear density, as described in the previous section. The difference between the obtained results for ρ/ω mesons and ϕ mesons is understandable as follows.

As for the width-broadening, according to the theoretical calculation by E. Oset *et al.* [9], which predicts the in-medium width broadening of the ϕ meson, the modification of the ϕ meson properties in the medium is strongly related to the change of the kaon properties in the medium. Thus it is not surprising that the obtained mass modification of ϕ meson is different from that of ρ/ω mesons. Thus far, however, there is no theoretical prediction to explain the observed width broadening of ρ/ω and ϕ mesons simultaneously. For example, the theoretical calculation by Klingl *et al.* [51] concludes the width broadening of the ϕ meson by a factor of about ten, which is based on the chiral meson-baryon effective Lagrangian with inclusion of vector mesons and electromagnetic interactions. But their calculation predicts much larger width broadening for ρ and ω mesons than ϕ meson, which contradicts to our observation in the ρ and ω mass region. It should be mentioned that it is difficult to describe the modification of the ρ meson spectrum by only the two parameters, pole mass shift and the width broadening, because ρ meson has very wide width even in vacuum ($\sim 150\text{MeV}/c^2$), and the in-medium spectrum of the ρ meson can be very different from a simple Breit-Wigner-type shape. Further informations from experiments as well as the development of theoretical studies are desirable.

As for the pole mass shift, the calculations by Hatsuda and Lee [7] predicted $16 \pm 6\%$ decrease of the mass for ρ and ω mesons and only 1–4% decrease for ϕ meson. Such difference occurs because the strangeness content in the nucleon plays important role in the calculation of the ϕ meson modification. The predicted k_1 for the ϕ meson is $(0.15 \pm 0.05)y$, here y is defined as $2\langle \bar{s}s \rangle_N / (\langle \bar{u}u \rangle_N + \langle \bar{d}d \rangle_N)$, as described in the Chapter 1. Our obtained result of the pole mass shift for the ϕ meson, as well as for ρ , ω mesons presented in [5, 42], is in good agreement with this prediction as shown in Figure 4.23. Although many theoretical predictions contradict to each other with regard to the pole mass shift, this agreement demonstrates that the physical nature of

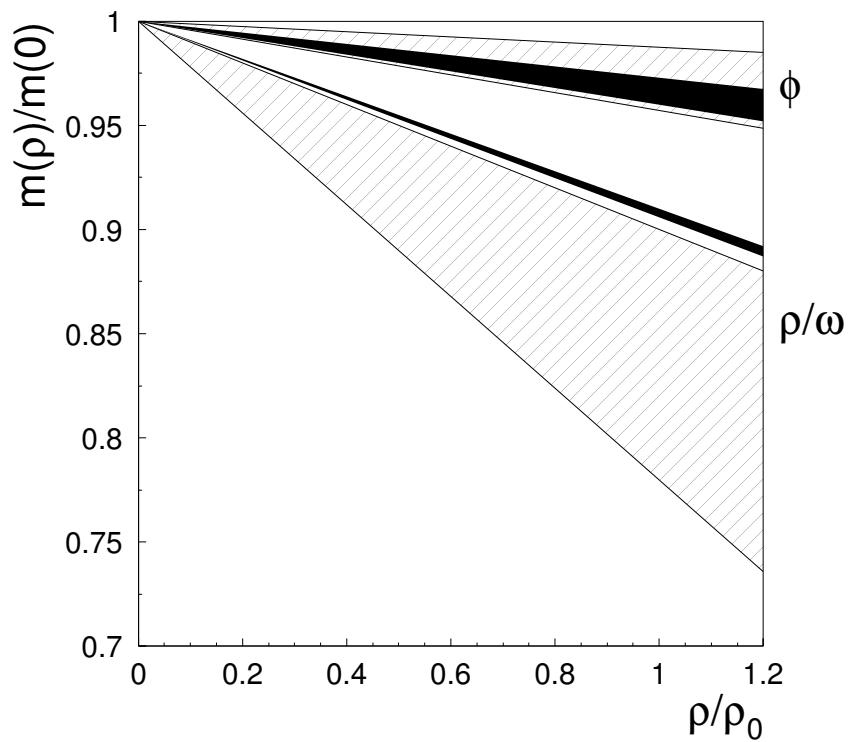


Figure 4.23: Comparison between the theoretical calculation with the hatched area for the uncertainty [7] and our results (black bands). Only statistical errors are taken into account in the widths of the black bands.

our observations for the pole mass shifts of light vector mesons can well be related to the chiral symmetry restoration in nuclear medium.

Chapter 5

Conclusion

We studied the invariant mass distribution of e^+e^- pairs obtained in the 12-GeV $p + A$ reaction at the KEK Proton Synchrotron. The main purpose of this experiment is to observe the modification of the spectral shapes of vector mesons, ρ, ω, ϕ at normal nuclear density.

The spectrometer was newly constructed at the EP1-B high-intensity primary beam-line for the simultaneous detection of $\rho, \omega, \phi \rightarrow e^+e^-$ and $\phi \rightarrow K^+K^-$ decays with high mass resolution. The data taking was performed from the year 1997 to 2002. The results presented in this thesis were obtained from the e^+e^- data taken in the year 2001 and 2002 with carbon (C) and copper (Cu) targets. We achieved the mass resolution for $\phi \rightarrow e^+e^-$ decays of 10.7 MeV/ c^2 when averaged over the present acceptance.

To investigate the velocity dependence of the invariant mass spectra of ϕ mesons, we divided the data into three $\beta\gamma$ regions. The data obtained from the carbon target was well reproduced in all the $\beta\gamma$ regions by the fit using the unmodified mass shape of the ϕ meson. On the other hand, the data obtained from the copper targets revealed a significant excess on the low-mass side of the ϕ meson peak in the slowest $\beta\gamma$ ($\beta\gamma < 1.25$) region, while in the higher $\beta\gamma$ region ($\beta\gamma > 1.25$) the resonance shape was reproducible with the unmodified shape. The χ^2/ndf value of the fit with unmodified mass shape was 83/50 for the copper target data when $\beta\gamma < 1.25$, which means that the fit was rejected at 99% confidence level. We evaluated the amount of the excess in the mass region 0.947-1.007 GeV/ c^2 and obtained $N_{ex} = 133 \pm 28(\text{stat.})_{-12}^{+5}(\text{syst.})$ and $N_\phi = 464 \pm 38(\text{stat.})_{-5}^{+6}(\text{syst.})$ (excluding the excess) for the copper targets data in the lowest $\beta\gamma$ region. This observation is consistent with a picture of the possible mass modification in a nucleus, because the decay probability inside a nucleus is expected to increase for ϕ mesons with lower velocity in a larger target nucleus.

We attempted to reproduce the observed excess with a Monte-Carlo-type model calculation that includes the in-medium mass modification of the ϕ meson. We assumed the density dependence of the ϕ meson mass as $m_\phi(\rho)/m_\phi(0) = 1 - k_1(\rho/\rho_0)$, where ρ_0 denotes the normal nuclear density. For the density dependence of the total width broadening, we assumed $\Gamma_\phi^{\text{tot}}(\rho)/\Gamma_\phi^{\text{tot}}(0) = 1 + k_2^{\text{tot}}(\rho/\rho_0)$. For Γ_ϕ^{ee} we also assumed

$\Gamma_\phi^{ee}(\rho)/\Gamma_\phi^{ee}(0) = 1 + k_2^{ee}(\rho/\rho_0)$, and examined following two cases: (i) the branching ratio $\Gamma_\phi^{ee}/\Gamma_\phi^{\text{tot}}$ remains unchanged in the medium; $k_2^{ee} = k_2^{\text{tot}}$, and (ii) Γ_ϕ^{ee} doesn't increase in the medium; $k_2^{ee} = 0$. When we fitted only the Cu data in the lowest $\beta\gamma$ region, where the anomaly is observed, the case (ii) was rejected at 99% C.L. while the case (i) was not rejected. It means that the data favor an increase of Γ_ϕ^{ee} in a nucleus. In the case (i), the obtained best-fit parameters are $k_1 = 0.034_{-0.007}^{+0.006}$, $k_2^{\text{tot}} = k_2^{ee} = 2.6_{-1.2}^{+1.8}$, meaning that the pole mass of the ϕ meson decreases by 3.4 %, and Γ_ϕ^{tot} and Γ_ϕ^{ee} increase by a factor of 3.6 at normal nuclear density.

The results presented in this thesis are the first and only experimental data which show the modification of the ϕ meson mass spectra in nuclear matter. Together with our earlier reports concerning the ρ and ω meson modification [4, 5], we conclude that the theoretical predictions on the in-medium modification of vector mesons are experimentally established.

Chapter 6

Acknowledgements

First of all, I would like to express my sincere gratitude to Prof. Hideto En'yo, the spokesperson of the present experiment. He gave me the opportunity to participate in the present experiment. I learned many things from him, especially the attitude toward the difficulties in the experiment, and his keen insight always impressed me. He has continuously encouraged and supported me at every stage of this work. I could not complete this work without his patient and tireless advising.

I am deeply grateful to Prof. Ken-ichi Imai, the leader of the experimental nuclear hadron physics (NH) group in Kyoto university, for his guidance, fruitful discussions and helpful advice in many aspects. He spent his time for discussions even in the new year's eve in the year 2006. I also wish to express my special thanks to Prof. Akira Masaïke, who was the head of the particle and nuclei (PN) group in Kyoto university. I benefited greatly from his suggestive advice.

I wish to express my appreciation to all the members of the E325 collaboration. I thank Dr. Satoshi Yokkaichi for his construction of the SLG, helpful consultations and his patience in waiting the output from me. I learned from him many things mainly about DAQ system and programming in the analysis stage as well as the treatment of the large amount of the data in RIKEN Super Combined Cluster (RSCC) and RIKEN-CCJ. I would like to express my appreciation to Dr. Tetsuya Murakami for his helpful comment on this thesis and effective assistance in the beam time. I remember that owing to his help I could find a bit error in a SCH during the beam time. I thank Dr. Masaya Ishino who constructed AC. He taught me lots of things about the analyses using Kaon arms and basics of the scintillation counter. I thank Dr. Kyoichiro Ozawa who constructed CDC and BDC. I learned a lot of things from his tireless effort in the experimental area on the operation and noise reduction of the drift chambers. I thank Dr. Tsuguchika Tabaru who constructed the electron triggers and kaon first level trigger. When I worked with him to improve the electron trigger system, he taught me many things about the electronics and FPGA programming as well as the trigger system. I thank Dr. Megumi Naruki who constructed RLG and FLG and calibrated all of the lead-glass calorimeters. I am thankful to Yoshio Yoshimura for his construction of the second-level kaon trigger. I thank Takuya Miyashita who constructed RGC. I

am thankful to Dr. Satoru Yamada for his helpful assistance in the measurement and calibration of the magnetic field. I thank Fuminori Sakuma who constructed VTC and calibrated the drift chambers excellently. I would like to thank Dr. Michiko Sekimoto. I benefited from her advice about the treatment of the drift chambers. I would like to express my thankfulness to Prof. Osamu Sasaki for his helpful advice on the construction of the read-out board of the drift chambers with ASD ICs. I thank Dr. Satoshi Mihara for his helpful comments on my paper and the excellent designs for many detectors in our spectrometer. I thank Hiroki Kanda, Dr. Masaaki Kitaguchi, Yoshinori Fukao, Manabu Togawa, Dr. Kouji Miwa and Terunao Nakura for their helpful assistance during the beam time. I would like to express my acknowledgement to Prof. Junsei Chiba for his keen advice and suggestions on the data analysis. I am thankful to Prof. Haruhiko Funahashi for his suggestive advice. I was a student of his experimental class in the undergraduate course of Kyoto university. His attractive guidance lead me to this experimental physics field.

I am thankful to Prof. Naohito Saito and Dr. Kiyoshi Tanida for their helpful advice and encouragements during my stay at Kyoto university. I would like to thank Dr. Munehisa Ohtani for helpful discussions from theoretical aspects.

I sincerely thank all the members of NH and PN groups in Kyoto university. I am also thankful to all the members of Radiation Laboratory in RIKEN and the staff members of RSCC and RIKEN-CCJ.

The experiment was fully supported by the staffs of KEK, including the PS beam channel group, the PS floor staff, the online group, the electronics division and the accelerator division. I wish to express my gratitude to Prof. Kazuhiro Tanaka and Prof. Masaharu Ieiri for the construction of the EP1-B beam line and the spectrometer magnet. In every beam cycle, a clean beam was delivered to our experimental area owing to the effort of the beam-channel staffs, Yutaka Yamanoi, Prof. Hiroyuki Noumi, Yoshihiro Suzuki, Yohji Katoh, Michifumi Minakawa, Erina Kusano and the group leader Prof. Minoru Takasaki.

This study was partly funded by the Japan Society for the Promotion of Science, RIKEN Special Postdoctoral Researchers Program, and a Grant-in-Aid for Scientific Research from the Japan Ministry of Education, Culture, Sports, Science and Technology (MEXT).

I would like to express my gratitude to my parents, Sadayuki and Hatsuko Muto for their understanding and support. Finally, I wish to express again my appreciation to my wife, Dr. Megumi Naruki for her lasting encouragement and helpful assistance.

Bibliography

- [1] Y. Nambu and G. Jona-LAsinio, Phys. Rev. **122** (1961) 345.
- [2] S. Klimt, M. Lutz and W. Weise, Nucl. Phys. **A542** (1992) 521-558.
- [3] W. Weise, Nucl. Phys. **A553** (1993) 59-72.
- [4] K. Ozawa *et al.* (E325 Collaboration), Phys. Rev. Lett. **86**(2001) 5019.
- [5] M. Naruki *et al.* (E325 Collaboration), Phys. Rev. Lett. **96**(2006) 092301.
- [6] G. E. Brown and M. Rho, Phys. Rev. Lett. **66** (1991) 2720.
- [7] T. Hatsuda and S.H. Lee, Phys. Rev. **C46** (1992) R34.
- [8] T. Hatsuda, H. Shiomi and H. Kuwabara, Prog. Theor. Phys. **95** (1996) 1009-1028.
- [9] E. Oset and A. Ramos, Nucl. Phys. **A679** (2001) 616.
- [10] D. Cabrera and M. J. Vicente Vacas, Phys. Rev. **C67** (2003) 045203.
- [11] F. Klinge, T. Wass and W. Weise, Phys. Lett. **B431** (1998) 254.
- [12] G. Agakichiev *et al.*, Phys. Lett. **B422** (1998) 405-412.
B. Lenkeit *et al.*, Nucl. Phys. **A654** (1999) 627c-630c.
B. Lenkeit *et al.*, Nucl. Phys. **A661** (1999) 23c-32c.
- [13] G.J. Lolos *et al.* (TAGX Collaboration), Phys. Rev. Lett. **80** (1998) 241-244.
- [14] D. Trnka *et al.*, Phy. Rev. Lett. **94** (2005) 192303.
- [15] R. Arnaldi *et al.*, Phy. Rev. Lett. **96** (2006) 162302.
- [16] K. Suzuki *et al.*, Phy. Rev. Lett. **92** (2004) 072302.
- [17] T. Eberl *et al.*, Nucl. Phys. **A752** (2005) 433c.
- [18] K. Ozawa *et al.*, Eur. Phys. J **C43** (2005) 421.
- [19] T. Ishikawa *et al.*, Phys. Lett. **B608** (2005) 215.

- [20] R. Muto *et al.*, Phys. Rev. Lett., to be published.
- [21] M. Takasaki *et al.*, KEK Internal **1** (1995).
- [22] M. Sekimoto *et al.*, Nucl. Instrum. Meth. **A516** (2004) 390-405.
- [23] I. Adachi *et al.*, Nucl. Instr. and Meth. **A335** (1995) 390.
- [24] M. Ishino *et al.*, Nucl. Instr. and Meth. **A457** (2001) 581.
- [25] Y. Sugaya *et al.*, Nucl. Inst. and Meth. **A368** (1996) 635.
- [26] Vector Fields Limited (UK), <http://www.vectorfields.co.uk/>.
- [27] developed in CERN. <http://consult.cern.ch/writeup/garfield/>
- [28] F. Sakuma, PhD thesis, Kyoto Univ. (2007).
- [29] O. Sasaki, ATLAS Internal Note, MUON-NO- (1999).
<http://www-online.kek.jp/sosamu/ASD-PRR.pdf>.
- [30] H. Hinterberger and R. Winston, Rev. Sci. Instr. **37**, 1004 (1966)
- [31] S. Kawabata *et al.*, Nucl. Inst. Meth. **A270** (1988), 11.
- [32] VMEbus architecture, IEEE 1014/D1.0.
- [33] T. K. Ohsuka *et al.*, KEK report 85-10 (1985)
- [34] ESONE Comimittee, Joint Nuclear Research Centre Ispra Establishment, Italy (1972).
- [35] Unidaq Documentation Set, SDC-93-487, Superconducting Super Collider Laboratory, 1993.
- [36] HBOOK, <http://wwwasdoc.web.cern.ch/wwwasdoc/hbook/HBOOKMAIN.html>.
- [37] Physics Analysis Workstation (PAW),
<http://wwwasd.web.cern.ch/wwwasd/paw/>.
- [38] X.org foundation, <http://wiki.x.org/wiki/Home>.
- [39] CCJ. <http://ccjsun.riken.jp/ccj/>.
- [40] Andy Hanuchevsky, <http://www.slac.stanford.edu/abh/bbcp/>.
- [41] HPSS. <http://www.hpss-collaboration.org/hpss/index.jsp>.
- [42] M. Naruki, PhD thesis, Kyoto Univ. (2006).
- [43] developed in CERN. <http://consult.cern.ch/writeup/minuit/>

- [44] S. Agostinelli *et al.*, Nucl. Instrum. Meth. **A506** (2003), 250-303.
- [45] A. Spiridonov, hep-ex/0510076.
- [46] J. Fleicher and F. Jegerlehner, Z. Phys. **C26**(1985) 629.
- [47] F. A. Berends and R. Kleiss, Nucl. Phys. **B177** (1981) 237-262.
- [48] Y. Nara *et al.*, Phys. Rev. **C61** (1999) 024901.
- [49] T. Tabaru *et al.*, Phys. Rev. **C74** (2006) 025201.
- [50] R. J. Glauber and G. Matthiae, Nucl. Phys. **B21** (1970) 135-157.
- [51] F. Klinge, N. Kaiser and W. Weise, Nucl. Phys. **A624** (1997) 527-563.